NUMERICAL INVESTIGATION ON THERMOMECHANICAL CHARACTERISTICS OF EARTH'S CRUST WITH MAGMA CHAMBERS

A THESIS SUBMITTED TO
THE GRADUATE SCHOOL OF NATURAL AND APPLIED SCIENCES
OF
MIDDLE EAST TECHNICAL UNIVERSITY

BY

SELİN ERDOĞAN

IN PARTIAL FULFILLMENT OF THE REQUIREMENTS
FOR
THE DEGREE OF MASTER OF SCIENCE
IN
MECHANICAL ENGINEERING

NOVEMBER 2024

Approval of the thesis:

NUMERICAL INVESTIGATION ON THERMOMECHANICAL CHARACTERISTICS OF EARTH'S CRUST WITH MAGMA CHAMBERS

submitted by **SELİN ERDOĞAN** in partial fulfillment of the requirements for the degree of **Master of Science** in **Mechanical Engineering, Middle East Technical University** by,

Prof. Dr. Naci Emre Altun
Dean, **Graduate School of Natural and Applied Sciences**

Prof. Dr. Serkan Dağ
Head of the Department, **Mechanical Engineering**

Assoc. Prof. Dr. Özgür Bayer
Supervisor, **Mechanical Engineering, METU**

Prof. Dr. Özgür Karaoğlu
Co-Supervisor, **Geological Engineering,**
Eskişehir Osmangazi University

Examining Committee Members:

Prof. Dr. Serkan Dağ
Mechanical Engineering, METU

Assoc. Prof. Dr. Özgür Bayer
Mechanical Engineering, METU

Prof. Dr. Almıla Güvenç Yazıcıoğlu
Mechanical Engineering, METU

Prof. Dr. Kaan Sayıt
Geological Engineering, METU

Assoc. Prof. Dr. Özgür Ekici
Mechanical Engineering, Hacettepe University

Date: 27.11.2024

I hereby declare that all information in this document has been obtained and presented in accordance with academic rules and ethical conduct. I also declare that, as required by these rules and conduct, I have fully cited and referenced all material and results that are not original to this work.

Name Last name : Selin Erdoğan

Signature :

ABSTRACT

NUMERICAL INVESTIGATION ON THERMOMECHANICAL CHARACTERISTICS OF EARTH'S CRUST WITH MAGMA CHAMBERS

Erdoğan, Selin
Master of Science, Mechanical Engineering
Supervisor: Assoc. Prof. Dr. Özgür Bayer
Co-Supervisor: Prof. Dr. Özgür Karaoğlu

November 2024, 117 pages

In this study, relationship between cooling and stress distribution around the magma chambers formed by silicate melts settled throughout the Earth's crust is researched. Subsurface magma chambers through crustal domain are modeled using COMSOL Multiphysics with 2D and 3D modeling approaches. The magma chambers, 30x5x5, 20x3x3, and 5x1x1 km in size, are examined in 12 distinct cases to explore different thermomechanical behavior applying distinct settlement depths and magma internal temperatures through depth of 1-30 km. Three initial internal magma temperature values are defined as 700°C, 800°C and 900°C. Earth's surface temperature is assumed constant at 15°C, with a thermal gradient of 25°C/km towards depth. Temperature dependent mechanical properties are assigned to magma and surrounding host rock. Results from both models are analyzed to better understand how changes in size, temperature, and location of magma chambers influence the thermo-mechanical behavior of upper crustal setting subjected to active deformation, such as intracontinental rifts and slab subduction zones. 2D and 3D model outputs are compared to determine the most suitable modeling methodology for similar geological scenarios in terms of modeling costs and data consistency. It is highlighted that the stress distribution in the 3D model is more homogenous and up to 20% lower compared to the 2D model in average; primarily due to the wider stress dispersion and more efficient heat transfer. The results suggest that the 3D models, outputting shorter solidification periods and lower stress concentrations, represent the stress patterns more reliably.

Keywords: Magma Chambers, Thermomechanical Effect, Stress Fields, Magma Solidification, Crust Deformation

ÖZ

MAGMA ODALARINA SAHİP YERKABUĞUNUN TERMOMEKANİK DAVRANIŞININ SAYISAL İNCELENMESİ

Erdoğan, Selin
Yüksek Lisans, Makina Mühendisliği
Tez Yöneticisi: Doç. Dr. Özgür Bayer
Ortak Tez Yöneticisi: Prof. Dr. Özgür Karaoğlu

Kasım 2024, 117 sayfa

Bu çalışmada, kapalı bir sistemde, silikat eriyiklerinin oluşturduğu magma odalarının yer kabuğu boyunca yerleşiminin yarattığı soğuma ve stres dağılımı ilişkileri incelenmiştir. Yer kabuğu boyunca yerleşmiş magma odaları COMSOL Multiphysics ile 2D ve 3D modelleme yaklaşımları ile modellenmiştir. Magma odaları 30x5x5, 20x3x3, 5x1x1 km boyutlarında olup, 1 ila 30 km derinliğinde bir kontrol hacminde her birinin yerleşimi arasında derinlik ve ilk iç sıcaklık farkı olan 12 durum için incelenecektir. Magma odalarının başlangıç sıcaklıkları 700°C, 800°C, 900°C olmak üzere üç farklı sıcaklık değerleri ile tanımlanmıştır. Yer yüzeyi sıcaklığı sabit 15°C alınıp, derinlikle birlikte her kilometrede 25°C artış olduğu kabul edilmiştir. Magma odaları etrafındaki ana kaya ve magma için sıcaklığa bağlı olarak farklı mekanik özellikler tanımlanmıştır. Modellerden alınan çıktılar analiz edilerek, manto ya da kabuk ergimesi sonucu oluşan magma odalarının boy, sıcaklık ve lokasyon değişimlerinin, yer kabuğunda aktif deformasyona maruz kalan bölgelerin (kıta yarığı, levha yitim zonları gibi) termo-mekanik davranışlarını nasıl kontrol ettiğinin anlaşılması hedeflenmiştir. 2D ve 3D model çıktıları, benzer jeolojik senaryolar için en uygun modelleme metodolojisini belirlemek amacıyla modelleme maliyetleri ve veri tutarlılıkları açısından karşılaştırılmıştır. Bunun sonucunda, 3D modeldeki stres dağılımının, 2D modele kıyasla daha homojen ve ortalamada %20’ye kadar daha düşük olduğunu, bunun başlıca sebeplerinin ise daha geniş stres yayılımı ve daha verimli ısı transferi olduğunu vurgulamaktadır. Sonuçlar, bu bağlamda, daha kısa katılaşma süresi ve daha düşük stres konsantrasyonlarına sahip 3D modellerin stres dağılımlarını daha güvenilir bir şekilde temsil ettiğini göstermektedir.

Anahtar Kelimeler: Magma Odaları, Termomekanik, Stres, Magma Katılaşması, Kabuksal Deformasyon

To my family.

ACKNOWLEDGMENTS

I wish to express my deepest gratitude to my supervisor Assoc. Prof. Dr. Özgür BAYER for his guidance, efforts, patience and fatherly understanding throughout my studies. Without his belief and persistence of seeing me graduated, I would not be able to output this work. His encouragement is so precious for me.

I'm extremely grateful to my co-supervisor Prof. Dr. Özgür KARAOĞLU for his guidance, advice and insight throughout the research. He kept relaying information on his profession, geology, which I did not have a clue and made me turn all those into a thesis study.

I would also like to thank to Deniz Alp YILMAZ who generously provided knowledge and expertise through my study.

I would also like to show my greatest respect and gratitude to Tamer ŞENYUVA for his mentorship from my childhood, throughout my career. He will be my role model all through my life with his broad vision.

I would like to extend my sincere thanks to Emrullah BİLGİN for his helps on getting over the bottlenecks of my studies. His ability of simplifying and solving even the most complex problems did not only give insight to me but also encouraged me.

I would like to express my gratitude to Osman Emre AYDIN, who, despite not being in this field, helped me navigate through some of the toughest challenges by offering invaluable technical support and a fresh perspective.

Lastly, words cannot express my gratitude to my family, especially to my dear mother. Their precious patience and endless support lifted me every time I need a support. I would also like to mention my pets, Bakla and Kayısı for all the emotional support.

TABLE OF CONTENTS

LIST OF TABLES

TABLES

LIST OF FIGURES

FIGURES

LIST OF ABBREVIATIONS

ABBREVIATIONS	
2D	Two dimensional
3D	Three dimensional
DAQ	Data acquisition
FEM	Finite element method
Gs	Giga seconds
ISV	In situ vitrification
LMC	Large magma chamber
MMC	Medium magma chamber
PCM	Phase change material
SA:V	Surface area to volume ratio
SEM	Scanning electron microscopy
SMC	Small magma chamber
TGM	Target geological model

LIST OF SYMBOLS

SYMBOLS

ρ	Density, kg/m^3
μ	Dynamic viscosity, kg/ms
$c_{p,\mathrm{eq}}$	Equivalent specific heat capacity, J/kg°C
Pe	Excess pressure in the magma chamber, Pa
Q	External heat, J
q	Heat flux by conduction, W/m^2
σ_2	Intermediate compressive principal stress, MPa
L	Latent heat, J/kg
P_l	Lithostatic pressure, MPa
X	Mass Fraction, -
σ_1	Maximum compressive principal stress, MPa
σ_3	Minimum compressive (maximum tensile) principal stress, MPa
σ	Normal stress, MPa
T_{cr}	Phase change temperature
θ	Phase of the material, -
ν	Poisson's ratio, -
τ	Shear stress, MPa
c_p	Specific heat capacity, J/kg°C
ε	Strain, -

T	Temperature, °C
k	Thermal conductivity, W/m°C
α	Thermal expansion coefficient, $°C^{-1}$
Q_{ted}	Thermoelastic dampening for thermoelastic effects in solids, J
σ_u	Ultimate strength, MPa
v	Velocity vector of translational motion, m/s
σ_v	Von mises stress, MPa
σ_y	Yield strength, MPa
E	Young's modulus, GPa

CHAPTER 1

INTRODUCTION

1.1 Magmatic Systems

The Earth's internal structure consists of three main layers, namely the core, the mantle, and the crust. Each of these layers has distinct compositions and properties that interact to drive the geological processes. The focus of this thesis study is the crust, which is the thin, outermost layer of the Earth. It plays a fundamental role in geodynamic processes, such as plate tectonics, faulting, and the formation of geological structures. Its composition, thickness, and mechanical properties are key factors in understanding the behavior of Earth's surface and its interactions with the underlying mantle.

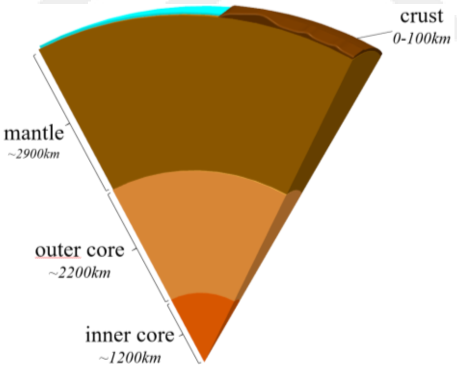

Figure 1.1. Layers of the Earth

The crust is subdivided into two distinct types; oceanic crust and continental crust. The oceanic crust, typically formed from mafic rocks like basalt, is dense, with an average thickness of about 7 kilometers. In contrast, the continental crust is composed predominantly of felsic rocks like granite, varying in thickness from 30 km to 70 km. Both types of crusts involve individual sublayers having distinct rock structures. The stratification results from the lithological differences caused by variations in mineral composition, rock accumulation over geological timescales, and magmatic system processes. Over millions of years, processes like sedimentation, tectonic movements, erosion, and biological accumulation have created distinct layers of different rock types and compositions [1].

Magmatic systems, which include the generation, movement, and differentiation of magma beneath the Earth's surface, are responsible for the formation of underground sub-layers, igneous rocks, and volcanic activities [2]. Magmatic processes are initiated by generation of magma. The increase in temperature, decrease in pressure and addition of volatiles contribute to the partial melting of rocks in the Earth's mantle, leading to the formation of molten rock, known as magma. This process occurs primarily at tectonic plate boundaries, hotspots, and subduction zones, where conditions such as rising temperatures or decompression cause minerals within the rock to melt and form a liquid phase. Molten rock is composed of three main components: a liquid melt (mostly silicate), suspended crystalline solids, and gas bubbles. When this molten material erupts and solidifies on the Earth's surface, it forms volcanic rocks, which can be either crystalline or glassy. Conversely, when magma cools and solidifies within the Earth's interior, the resulting igneous rocks are classified as intrusive or plutonic rocks. These formations differ primarily in their cooling environments and resultant textures [3]. Partial melting of rocks may occur, forming domains of magma [4]. After its formation (which mainly occurs within the mantle), magma migrates through the mantle, then to crust, moving from regions of higher pressure to lower pressure along paths of least resistance, driven by thermodynamic gradients and fluid dynamics principles. This propagation can occur both horizontally and vertically through the pathways such as fractures, faults, or magma chambers [5].

As magma moves, it cools and may differentiate due to the crystallization of silicic mush zones and formation of minerals at different temperatures, leading to distinct rock compositions [6,7]. Over geological timescales, these formations shape the Earth’s crustal domains. Magma solidification may not completely occur below the Earth’s surface; it sometimes reaches the surface via volcanic vents or fissures, causing eruptions. In most cases, magma accumulates in igneous bodies known as magma chambers, where it cools over time [8]. The surrounding rock structure, called as the host rock, plays significant role in this process.

Magma chambers, which are underground reservoirs filled with magma, play a considerable role in volcanic systems and crust deformations, which in turn, the formation of underground rock structure. These chambers are categorized based on depth, size, shape and composition. Large, deep-seated magma chambers, known as "reservoirs", are located at depths of 20 to 80 km, while other magma chambers can be settled at depths of 1-9 km below the Earth's surface [9,10]. The variation in size and form of magma chambers is influenced by factors such as magma volume, geological structures, and tectonic setting. Their shapes can include tabular, lens-shaped, irregular, or complex geometries shaped by surrounding rock structures and magma emplacement processes.

The difference in composition are influenced by magma chamber's depth, size and position. Magma chambers located in the deep lithosphere are typically filled with alkali-basaltic magma, whereas shallow ones can mostly be acidic (e.g. rhyolite) or intermediate [11]. The characteristic of magma, whether acidic, basaltic, or intermediate, is determined by its chemical composition. Both magma inside a chamber and the surrounding host rock can vary in composition. The compositional differences in magma chambers at various depths can be exemplified by the underground volcanism observed in the Yellowstone region illustrated in Figure 1.2.

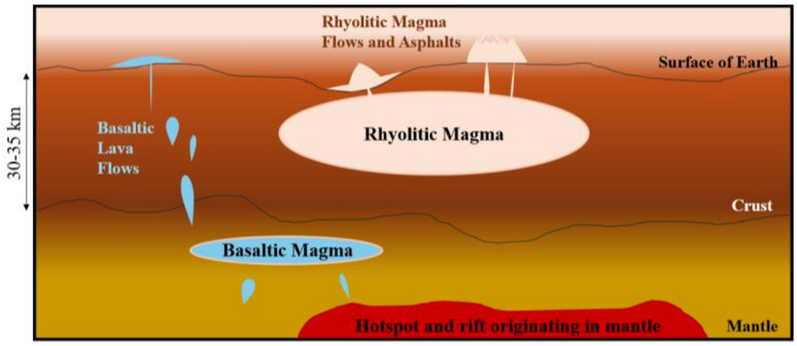

Figure 1.2. Magma chambers in Yellowstone region [adapted from 12]

Variations in magma chamber compositions lead to differing chamber temperatures which initiate heat transfer, subsequent magma cooling. This heat transfer between host rock and magma drives the solidification process, leading to the formation of rock. Crystallization, in which melts solidify to form solid structures, is the key to this process.

As magma cools and solidifies, thermal stresses, may induce fractures in the host rock making the thermo-mechanical properties of both magma and host rock critical in predicting these fractures. Magma's mineral composition has significant effect on its properties as detailed in Table 1.1.

Table 1.1. Properties of common magma compositions at 1 bar [13]

Composition	**Liquidus Temperature [°C]**	**Density [kg/m^3]**	**Specific Heat Capacity [J/kg°C]**	**Dynamic Viscosity [kg/ms]**
Granite (dry)	900	2349	1375	1.2×10^{10}
Granite (2% H_2O)	900	2262	1604	5×10^5
Granodiorite	1100	2344	1388	1.3×10^6
Gabbro	1200	2591	1484	30.0
Eclogite	1200	2591	1484	-
Komatiite	1500	2748	1658	0.15
Peridotite	1600	2689	1793	0.25

The composition of magmatic rocks varies significantly and is typically categorized by the presence of major, minor, and trace elements. Major elements, with oxide abundances exceeding 1 wt%, typically include SiO_2, Al_2O_3, FeO, Fe_2O_3, CaO, MgO, and Na_2O. Minor elements, present in concentrations between 0.1 and 1 wt%, mainly include K_2O, TiO_2, MnO, and P_2O_5. Trace elements, comprising less than 0.1 wt%, are also present. Volcanic rocks, which form from the rapid cooling of lava at the Earth's surface, are often classified based on silica (SiO_2) and total alkali content

(Na_2O + K_2O), while plutonic rocks, which crystallize slowly from magma beneath the Earth's surface, are better defined by their mineralogical composition, such as quartz, plagioclase, and alkali feldspar [14, 15].

Magmatic rocks are predominantly of two compositional types: basalts and granites. Basalts are mafic rocks rich in Fe and Mg oxides, typically found in the oceanic crust. Their solidus and liquidus temperatures are approximately 1000°C and 1200°C respectively. Granites, which are more abundant in continental crust, represent felsic rocks rich in silica. Their solidus temperature is around 960°C, with hydrous conditions lowering this to 680°C, and their liquidus temperature is approximately 1050°C [16].

The evolutionary history and composition of magma significantly influence its physical properties. For instance, as presented in Figure 1.3, melt density varies according to composition and temperature in anhydrous and mafic magmas across the compositional spectrum from rhyolite to komatiite.

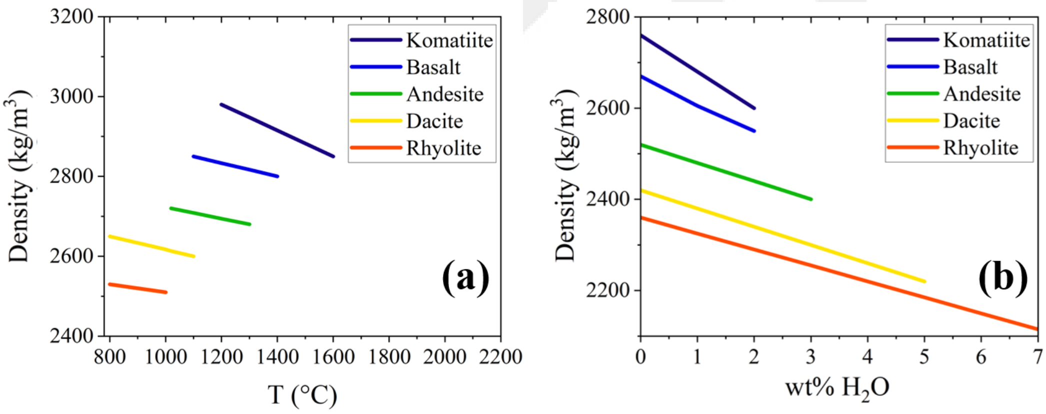

Figure 1.3. Variation of magma density with (a) temperature and (b) wt% H_2O [17]

The corresponding temperatures for each melt align with typical eruption temperatures. These densities are calculated at a standard pressure of 1 bar, reflecting the effects of compositional and thermal variations. It ranges from 2300 to 2900 kg/m³ for silicic to ultramafic compositions, inversely proportional to magmatic temperatures with the contributional effects of alkali metals and water. Dissolved water content leads to drastic decline in magma density. As alkali metals, volatiles and water are more compressible, their presence significantly affects the pressure dependence of magma density. Compressibility, which plays a vital role in the explosivity of volatile-rich magmas is also affected by density [17]. The differentiation of magma by fractional crystallization is also density-dependent, influencing its segregation, ascent, and eruption [18].

The buoyancy of magma, which also influences its ability to ascend and erupt, is determined by the density difference between magma and country rock, governed by gravitational forces and the depth of the magma. Positive buoyancy occurs when magma is less dense than the country rock, promoting ascent; whereas negative buoyancy occurs when it is denser, hindering movement. The point where buoyancy shifts from positive to negative is the neutral buoyancy level, where magma ascent ceases [19].

The cooling rate of magma is also dependent on its composition, influences its properties and affects the crustal structure of the host rock. Rapid cooling leads to fine-grained textures due to the limited time for crystal growth, albeit slower cooling rate results in coarse-grained textures [20].

Although magma solidifies to form igneous rock, its content and properties do not remain entirely conserved, as some melts crystallize at different rates, creating a unique structure [21]. The crystalline texture of the host rock significantly affects its mechanical response to stress, influencing properties such as density, yield strength and Young's modulus values. These properties are essential to foresee fractures, such as dykes, sills, or even volcanic eruptions. The potential for fractures, and therefore the thermomechanical properties of the host rock, are of particular importance in geological studies.

Two primary types of mechanical fractures occur in host rock are shear fractures, caused by shear stresses and extension fractures, caused by tensile stresses. Shear fractures manifest as strike slip faults, while extension fractures include tension and hydro fractures. Tensile fractures arise from tensile stress, resulting in structures like dykes [22]. Faults are zones where rocks have undergone fracturing and displacement along a planar surface and both tensile and shear stresses can play a role in their formation. The dominant stress type depends on the fault type and the direction of tectonic forces in the region. In Figure 1.4, fault and deformation types are illustrated along with the stress types that lead to their formation.

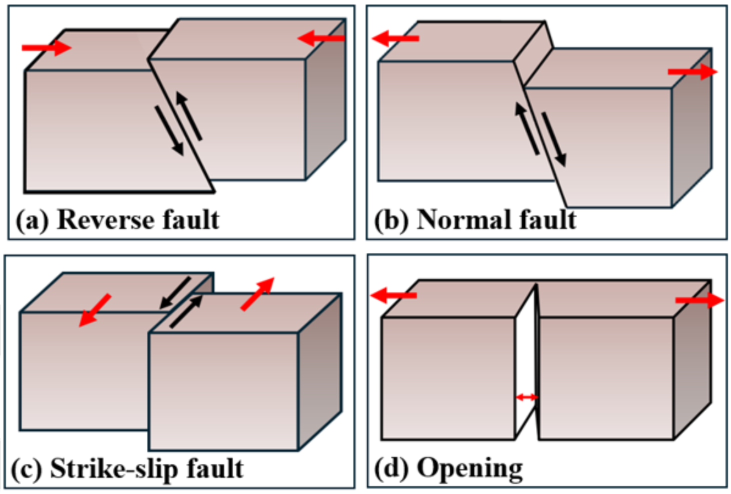

Figure 1.4. Types of faults dominated by (a) shear stresses, (b,d) tensile stresses and (c) compressional stresses

In a geological study area, the presence of grabens or horsts typically indicates favoring tensile fractures, prompting a focus on analyzing tensile or compressive stresses. This expectation arises from the tendency of such features to form under extensional forces. However, in cases where the geological setting indicates significant horizontal displacement between two distinct zones moving in opposite directions, as depicted in Figure 1.4-c, the likelihood of shear fractures increases. In these situations, the analysis shifts towards examining shear stresses, which play a crucial role in driving deformation and failure mechanisms under lateral shearing conditions.

Internal pressure and thermal stresses of magma chambers exert pressure on the surrounding host rock, leading to stress concentrations. Therefore, the existence of magma chambers, through their thermomechanical effects, contributes to the generation of shear and tensile stresses or amplifies existing ones. Other than their contribution on the complex loading on host rock, magma chambers also cause fractures through their direct movement and propagation within the rock. For instance, the roof of a magma chamber might fail due to tension and a dyke may form. In this case, magma follows the paths dictated by the maximum principal compressive stress, σ_1. Else, if the combined lithostatic and magma excess pressures surpass the host rock's tensile strength and minimum principal compressive stress, σ_3, the magma chamber ruptures, creating hydrofractures [23]. Lithostatic pressure (p_l), depending on depth, is the pressure exerted by the overlying rocks and sediments where magma excess pressure (p_e) corresponds to the fluid pressure inside the magma chamber. It is important to emphasize that generally, the overlying rock does not consist of a single type of rock and all different layers' pressure effect should be considered individually and then summed for the resultant p_l value [24]. Consequently, surface conditions have a more significant impact on shallow rock structures. If a magma chamber's distance to Earth's surface is lower than the chamber's diameter, free surface affects the local stress concentrations around the magma chamber [25]. As the lithostatic pressure is low in shallow crust, effects caused by magma chambers dominate.

Stresses cause fracture when their magnitude exceeds the strength of host rock [26]. Similarly, eruptions take place when the magma pressure in a reservoir or chamber exceeds the host rock's strength [13]. Therefore, to make reasonable assumptions on host rock fracture, deeper understanding of host rock properties is needed.

At low stress levels, rocks are linear elastic materials which behave with respect to Hooke's Law [27]. In simpler terms, exposed stress versus host rock's elastic (temporary) deformation has a linear relation whose slope outputs the E (Young's modulus) value of the rock. Rocks having large Young's modulus are called stiff and the others are compliant. Common solid rock property values are between 0.10 and 0.35 for Poisson's ratio and 1 GPa and 70 GPa for Young's modulus [28, 29]. Rock strength increases with increasing crust depth in general but pores, vesicles, present fractures and contacts also have a significant effect on those properties. Actual values can be found not only by in situ examinations but also with theoretical models using upscaling.

Apart from the temporary deformation characteristic, which is determined by Young’s modulus, plastic deformation behavior also decides on rock property. Host rocks having considerable plastic deformation before fracture are called ductile where the ones who immediately breaks before little permanent deformation are called brittle. Generally, as the crust depth increases and overburden pressure increases, host rock becomes more ductile [30].

Rock’s stress-strain curve is highly informative to comment on the effects of stresses on a rock structure. In Figure 1.5, behavior of a rock when exposed to compressive stress until a macroscopic failure occur is seen. First portion is nonlinear where the following elastic portion whose slope is the E value is linear. The reason of the first portion being concave upwards is that this process includes the closing of microcracks and pores in the structure. The σ_y value in a σ-ε curve is the yield strength of the rock where it starts to plastically deform. After exceeding σ_y value, plastic deformation starts with the growth of microcracks in the stress direction. Lastly, the macroscopic fracture starts after σ_u, ultimate strength. The last end of the graph is residual strength which the rock has after fracture. For common rocks, a sudden fracture occurs after region 3, therefore the 4th portion of Figure 1.5 is significantly shorter than illustrated.

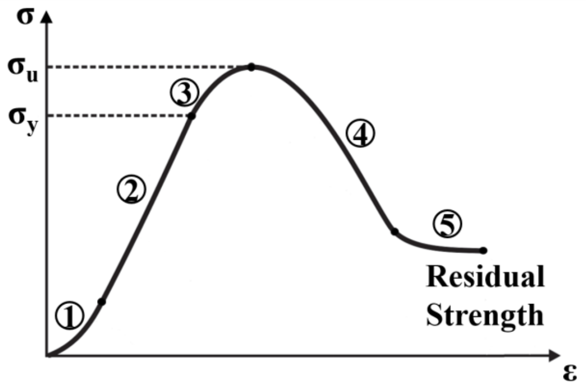

Figure 1.5. Typical stress strain curve of a rock specimen

Elastic deformation of rocks is not responsible on deformed rock's crack but leads to local tensile, compressional or shear stresses around crust layers or grain interfaces, causing fracture on another rock structure having less strength [31]. Even though elastic deformation and the associated stresses may not directly cause fracturing in the rock, they should be examined in detail as they transfer load to adjacent domains. Therefore, stress vectors having three orthogonal components on a domain is illustrated in Figure 1.6. Normal stress (σ) acts perpendicular to the plane where shear stresses (τ) are parallel. The first index of stress is the axis perpendicular to the shear acting plane and second index is the direction of stress.

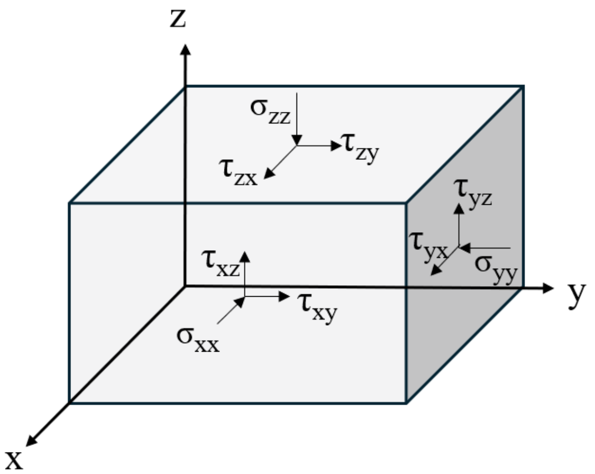

Figure 1.6. Components of stress tensor at a control volume

The maximum and minimum normal stresses occur within a control volume exposed to complex loading conditions are identified as principal stresses: σ_1, σ_2, σ_3. Composition of principal stresses as in Eqn (1.1) is the von Mises stress, defined as the effective or equivalent stress, allowing a comprehensive assessment of deformation and yield conditions. Tresca and von Mises criteria are indicated as the most appropriate criteria to use when considering ductile or plastic rock behavior. Von Mises states as von Mises stress exceeding the yield strength or alternatively, octahedral shear stress exceeding 0.47 times the yield strength [32]. It is appropriate to work on von Mises stress contours and trajectories to estimate shear fracture behavior of rocks and on σ_3 for the tensile fractures.

$$\sigma_v = \sqrt{\frac{(\sigma 1 - \sigma 2)^2 + (\sigma 2 - \sigma 3)^2 + (\sigma 3 - \sigma 1)^2}{2}} \tag{1.1}$$

In summary, the primary focus encompasses the processes of solidification and the resulting rock fracture in the host rock due to their interrelated impacts. All concepts and behaviors of the magmatic systems mentioned above are studied both individually and in combination in the literature to enhance the understanding of tectonic occurrences.

1.2 Literature Review

So far, the relation between magma chambers and tectonic environments has been studied by numerous researchers. Crystallization, solidification and rock fracture have been extensively studied for forecasting rock age and crust deformations. Stress distributions caused by magma chambers' thermomechanical effects, although relatively recent, have also been investigated. The important clusters of studies created to understand the different aspects discussed in Section 1.1 are presented below.

Formation and dynamics of magma chambers are dominated by magma transport and solidification controlled by fluid dynamics and thermodynamics respectively. Spark extensively studied these concepts to make forecasts on magma motion and eruptions. These studies identify four mechanisms for magma chamber formation; magma intrusion, defrosting, reactive flow accumulation, and layer coalescence by discussing how these mechanisms contribute to magma chamber development and the diversity of igneous phenomena. [5, 33]. Spark's studies on magma formation and dynamics play a vital role in studies considered magma motion and behavior. Magma flow is modelled to examine the potential of formation of chambers, dykes, sills and the occurrence of eruptions in the literature [34-37].

Crystallization concept have been deeply studied, generally by mating with mineral composition as they are highly related. In the late 80s, Cashman studied the crystallization dynamics of rocks which are all major sources of this field. The dynamics of crystal growth and the mechanisms of crystal formation in magmas are explored. These researches focus on how crystallization processes influence magma viscosity and the resulting geological features, providing insights into the behavior of magma during cooling and solidification. [38-40]. Rather than the crystallization volume itself, chemical processes at the interfaces of crystal melts were also taken into consideration. Albarede et al. and Lofgren et al. found that if the growth rate of crystallization is higher than the components diffusing away from the interface, a chemically affected zone will form around the crystal leading to skeletal like crystal structures having chemical differences from their parent melt [41,42]. In support of this, Grove et al. held an experiment and observed that a simple growth rate difference might cause many different crystal compositions all emerged from the same parent melt because of the cooling rate differences caused by different mineral properties [43]. Kotash noted that not only the mineral composition of magma but also the presence of volatiles has an impact on host rock properties as they affect the output host rock material by escaping and leaving solidified material behind with vesicles (holes) trapped inside [44]. Small scale experimental studies and numerical models to observe crystallization dynamics are also made [45-47].

The process of magma chamber solidification has been studied extensively by many researchers. Delaney et al. worked on a 1D model for the solidification of magma in a dyke in early 80s [48]. This study has an importance for having analytical relations and solution methodologies without needing any software. Similarly, analytical thermal models were studied by Annen et al. for a 1D geometry. Spatial temperature value at any time and radius is obtained by combining analytical formulations to obtain the solidification time and thermal halos [49]. 1D analytical models are important as they discuss the physics of events and form the basis of software applications on geological studies.

From 1995 and on, with geological modeling software came into use, numerical analyses started to emerge in literature. Silva et al. modeled the conductive cooling of a magma body in host rock to obtain temperature profiles. Temperature data of magma bodies were analyzed, and it is found that near magma chamber body, continuous gradient temperature profiles all around the chamber which is called “thermal halos” affect deformation behavior of the rocks [50]. Bea, studied granite magma solidification for magma chambers cooling at distinctive crust depths with the properties output from MELTS by inputting the mineral composition [51]. Research on the cooling and solidification of magma by modeling are held to comment on the age of a rock, magma chamber [52-64].

Other than the analytical studies or models, solidification can be observed via captures of SEM methods for a known aged chamber or analyzed through small scale experiments. As an instance, Dunbar et al. held an ISV experiment at Oak Ridge National Laboratory on solidification of an artificial melt to deeply investigate solidifying process. Dolomitic limestone gravel was poured inside a saprolite domain and temperature data is taken to observe crystallization profile by time. This temperature profile gives an insight into the true pattern for magma cooling and solidification [65]. Another experimental procedure coupled with modeling is held by Rodríguez et al. This study was held to see the accuracy of experiment numerical approach and scaling for magma solidification cases by observing the solidification of 10 mm melt capsules and relating them with large scale magma chambers. According to this study, the experimental-numerical approach largely depends on the volume and aspect ratio of the magma chamber [66].

For modelling, many studies in literature neglects the property differences in crust layers but in reality, there is crust heterogeneity. To obtain the lithospheric domain and its sublayers, Tarhan studied the crust layers of stratigraphic columnar section of Eastern Anatolia Accretionary Complex consisting of the layers composed of sandstone, metamorphic rocks, massive gabbro and limestone. A significant fractural anisotropy source is the Young’s modulus variability between layers. For instance, continental crust tends to have a higher Young's modulus compared to oceanic crust due to differences in composition and thickness [67]. Gudmundsson held a study by considering effects of Young’s modulus variations of host rock and outputted those changes in mechanical properties over space and time influence fault displacement and scaling behavior [68]. It highlighted the fact that crust layers having different properties should be considered in modelling.

Gudmundsson has highly valuable works on the mechanical effects of magma chambers. Hydrofracture occurrence examination urged him to study stress distributions on host rock, around magma chambers [69]. He developed studies on stress distributions and output other valuable analytical relations for foreseeing any fracture causing structure formations like dykes, sills or eruptions [70]. Further, Gudmundsson studied the local stress concentrations caused by magma chambers and output analytical cavity models by considering different configurations and shapes for magma chambers. He has found that if the distance between a magma chamber and Earth's surface is lower than 1.73 times the radius of the magma chamber, it exerts the maximum stress to Earth's surface. Otherwise, maximum stress occurs at points on magma chamber host rock interface. Magnitudes and locations of maximum tensile stress and maximum compressive stress are both outputted in Gudmundsson's study with analytical relations [71, 72]. Those studies gave insights into all research where mechanical effects of magma chambers are considered.

A recent set of studies on mechanical effects of magma chambers on host rock structure are held by Browning and Karaoğlu. Their model of the anisotropic domain of Karlıova region's crust with magma chambers having complex loading conditions, magma internal pressure and external loads, outputted the stress distributions caused by magma chambers [26]. Similarly, Karaoğlu et al. investigated the Triassic mafic igneous system of Antalya by building a 3D model having external loadings and prescribed velocities simulating tectonic motions to output stress distributions [73]. Browning et al. studied the dykes formed in Santorini with magma chamber ruptures by using real tectonic data [74].

Magma chambers' thermomechanical effects begin to make an impact in the literature after pure mechanical studies. Karaoğlu et. al studied the thermomechanical effects for Karlıova Triple Junction. These studies evaluate that volcanic rocks and faults are significantly influenced by thermal fluid movement and heat transport, with magma beneath the Varto and Özenç volcanoes serving as the primary heat source [75,76]. In addition, Browning et al. conducted a study on the thermomechanical effects of magma chambers with a 2D model having a homogeneous host rock domain without any temperature gradient. According to this study, thermal expansion is responsible from the increase of shear and decrease of tension around the chamber when compared to a case having only purely mechanical effects [77].

1.3 Motivation, Objective and Organization of Thesis

Magma chambers significantly influence the thermo-mechanical constraints of surrounding host rock, which is crucial in earth sciences for better understanding dyke nucleation, crustal deformation, and rock fracture. These insights may provide forecasts on tectonic interactions such as earthquakes, volcanic eruptions, and ground deformations. Studies on magma chambers have been discussed in the previous section, covering both fundamental behaviors and specialized topics. While many numerical models exist for specific geometries, thermal factors affecting mechanical behavior are less explored. Thermomechanical studies on the effects of magma chambers are rare and relatively new, highlighting the need for advanced numerical thermomechanical models. Given the challenges and costs of field measurements in earth sciences, numerical modelling becomes crucial in these contexts. Therefore, developing thermomechanical based numerical models and recommending optimizing solutions—such as investigating the differences between 2D and 3D models—would provide significant contributions to the field.

In the literature, solidification of magma chambers is typically modelled using 2D frameworks with constant, temperature-independent properties. Similarly, stress accumulations around magma chambers are analyzed separately using solid mechanics models that do not account for temperature variations. However, stress distributions do not simply depend on mechanical properties and magmatic pressure only. Rocks might fracture because of the accumulation of thermal stresses caused by thermal expansion and contraction during magma solidification. In addition, as the change in temperature affects the properties of magma and the surrounding host rock, temperature dependent properties should be considered in numerical modelling of cooling and solidification of magma chambers. This study aims to investigate crustal behavior when mechanical stresses are coupled with thermal stresses with different modeling approaches and make a comparison on them. The novelty lies in developing a model incorporating those temperature-dependent properties and coupling solid mechanics with heat transfer physics through 2D and 3D transient modelling. 2D and 3D models on a specific geological case in COMSOL Multiphysics® 6.1 are developed to analyze the thermomechanical interactions occurring on Earth's crust [78]. The results of these coupled modelling approaches are then compared with each other, highlighting the differences between 2D and 3D methodologies. With this comparison, insights are gained into more accurate predictions of the solidification process and stress fields in nature.

The findings of this study reveal the impact of positional and thermal changes in magma chambers on the thermo-mechanical behavior of the upper crustal setting, as obtained through both 2D and 3D models. The methodology used in these analyses is detailed in the following section.

CHAPTER 2

METHODOLOGY

In this study, a common subsurface formation in geology is examined under different scenarios to investigate solidification processes of magma and the stresses exerted on surrounding rocks during this process. This subsurface formation is a specific geological case consisting of a crust domain having magma chambers and host rock, is identified as Target Geological Model (TGM). TGM is analyzed by coupling thermal and mechanical effects with 2D and 3D modeling approaches in COMSOL Multiphysics, by inputting temperature dependent properties. Due to the long timescales and large domains involved in geological models, experimental data lacks and validation with experimental data is not applicable. Therefore, preliminary analyses are conducted first, to gain insights into the general framework and accuracy of the model setup.

In the preliminary studies, models are constructed with scenarios based on literature studies, in-situ instantaneous measurements of chamber ages or similar physical analogies found in the literature. These preliminary models are established to provide insights into the inputs and model setup, and the obtained results are compared with literature findings in Section 3. Once the accuracy of the model setup and the employed physics are confirmed, TGM is built by using the same physics and modeling approach.

In TGM, the two physical phenomena used are heat transfer and solid mechanics coupled with thermal expansion. These pyhsics are well-established and widely used in COMSOL. Therefore, the software gives accurate results, enabling it to mitigate the lack of validated data for the models. In the literature, studies emphasizing COMSOL’s reliability are present. For instance, Dagher et al conducted the simulation of thermal and hydrogeological effects of a shallow lake in a permafrost environment and confirmed that time-dependent heat transfer with phase change effects can be accurately modeled by COMSOL by validating data from previous studies [79]. Similarly, Freeman et al. built a hydro mechanical model by coupling heat transfer and structural modules in COMSOL Multiphysics and pointed out the accuracy of the results obtained from COMSOL for a well-constructed model by validating the outputs [80].

Even through all those preliminary studies and COMSOL's ability to deal with these simple physics, due to the absence of experimental data to validate the temperature and stress values spanning millions of years obtained from all these models, definitive conclusions cannot be drawn, but they provide useful insights.

2.1 Theory

The scenario in TGM is characterized by a crust structure containing three ellipsoidal magma chambers of sizes 30x5x5 km, 20x3x3 km, and 5x1x1 km surrounded by host rock as presented in Figure 2.1. Over time, these chambers undergo a process of solidification, leading to significant thermal and mechanical interactions with the surrounding host rock. The resulting stresses within the host rock are influenced by a combination of thermal expansion and contraction phenomena, necessitating a coupled approach that integrates heat transfer and solid mechanics.

Figure 2.1. Visualization of the TGM - three magma chambers in host rock domain

This analysis encompasses the physics of heat transfer and phase change coupled with solid mechanics via thermal expansion. The magma chambers are modeled as phase change material while the host rock is assumed to undergo no phase changes. Magma solidification takes place with heat transfer through magma chamber to host rock. Related governing equations are given in this section.

Assuming negligible radiation, the energy equation for magma is:

$$\rho c_p \left(\frac{\partial T}{\partial t} + \boldsymbol{v}.\nabla T\right) + \nabla.\mathbf{q} = Q \qquad (2.1)$$

where ρ is density, c_p is specific heat, $\frac{\partial T}{\partial t}$ is the rate of change of temperature with time, $\boldsymbol{v}.\nabla T$ is the convection term, $\nabla.\mathbf{q}$ is the heat conduction term, Q represents additional heat sources, in this case from other magma chambers and reservoirs. However, as the control volume for energy equation is magma only, heat transfer from other chambers cannot be considered in it but included in the conduction between host rock and magma, therefore it is zero. Velocity vector of translational motion is represented with $\boldsymbol{v}$ where lack of velocity of fluid magma flow enables to set the term including it to become zero. In reality, there is a fluid motion of magma within magma chambers driven by buoyancy but in similar studies, this motion has either been neglected or addressed as a separate topic of investigation. Therefore, the convection term is omitted. Heat flux by conduction is expressed with Eqn. (2.2).

$$\mathbf{q} = -k.\nabla T \qquad (2.2)$$

In order to model the phase change phenomenon in the magma domain, apparent heat capacity formulation is used. In this method, heat capacity of the material is taken as an equivalent $c_{p,\mathrm{eq}}$ outputted according to the phase and mass fraction.

$$c_{p,eq} = \theta_1 c_{p,1} + \theta_2 c_{p,2} + L\frac{\partial X}{\partial T} \qquad (2.3)$$

θ denotes the percentage of the material and subscripts 1 and 2 indicate the phase, liquid and solid respectively. L is the latent heat of magma and X is the mass fraction expressing the ratio of solidified magma to its initial form. As the specific heat is temperature dependent and same relation is used for both magma and host rock, $c_{p,1}$ and $c_{p,2}$ values are both equal to c_p(T) and Eqn. (2.3) becomes Eqn. (2.4).

$$c_{p,eq} = c_p + \mathrm{L}\frac{\partial \mathrm{X}}{\partial \mathrm{T}} \tag{2.4}$$

Eqn. (2.5) is obtained by substituting Eqn. (2.2) and Eqn. (2.4) to Eqn. (2.1),

$$\rho c_p \frac{\partial \mathrm{T}}{\partial \mathrm{t}} = \nabla.(k.\nabla \mathrm{T}) - \rho \mathrm{L}\frac{\partial \mathrm{X}}{\partial \mathrm{t}} \tag{2.5}$$

When heat transfer is coupled with solid mechanics, the additional term of thermoelastic dampening, Q_{ted} should be added to Eqn. (2.5). It is included in energy equation only when solid mechanics is coupled with heat transfer because it represents dissipation of heat caused by an external mechanical stimulant. Then, Eqn. (2.5) becomes Eqn. (2.6).

$$\rho c_p \frac{\partial \mathrm{T}}{\partial \mathrm{t}} = \nabla.(k.\nabla \mathrm{T}) - \rho \mathrm{L}\frac{\partial \mathrm{X}}{\partial \mathrm{t}} + Q_{ted} \tag{2.6}$$

$$Q_{ted} = -\alpha \mathrm{T}: \frac{\partial \mathrm{S}}{\partial \mathrm{t}} \tag{2.7}$$

In Eqn. (2.7), α is the thermal expansion coefficient, and S is the second Piola-Kirchhoff stress tensor which is the term relating the internal forces in a deformed material to its undeformed configuration.

$$\mathrm{S} = \mathrm{S_{ad}} + \boldsymbol{C}: \varepsilon_{\mathrm{el}} \tag{2.8}$$

C is the constitutive tensor which is a function of Young's modulus and Poisson's ratio as it establishes the linear relationship between strain and stress. $\varepsilon_{\mathrm{el}}$ is the elastic strain representing the elastic deformation of the material. $\mathrm{S_{ad}}$ is the adiabatic stress component called Second Piola-Kirchhoff stress tensor which is the internal stress under adiabatic conditions. It can be obtained by Eqn. (2.9).

$$\mathrm{S_{ad}} = \mathrm{S_0} + \mathrm{S_{ext}} + \mathrm{S_q} \tag{2.9}$$

S_0 is the initial stress component at undeformed state. S_{ext} is the external stress component refering the stress due to boundary loads, which is due to the magma internal pressure in present case. S_q is the thermal stress which is the stress caused by thermal effects.

$$\varepsilon_{el} = \varepsilon - \varepsilon_{inel} \tag{2.10}$$

Elastic strain is calculated with the subtraction of inelastic strain (ε_{inel}) which is the irreversible deformation from overall deformation, ε. As the materials are assumed as linear elastic, inelastic strain is neglected. Thermal strain, which shows the amount of thermal expansion is obtained by Eqn. (2.11).

$$\varepsilon_{th} = \alpha(T)(T - T_\infty) \tag{2.11}$$

The equation of motion to obtain stress magnitudes for a linear elastic material solved in FEM model is Eqn. (2.12).

$$\rho \frac{\partial^2 \boldsymbol{u}}{\partial t^2} = \nabla.\boldsymbol{\sigma} + \boldsymbol{F_v} \tag{2.12}$$

In Eqn. (2.12), $\boldsymbol{u}$ is the displacement field, $\boldsymbol{\sigma}$ is the stress tensor and $\boldsymbol{F_v}$ is the volume force vector. As there is zero prescribed velocity in the model and no volume force is present, Eqn. (2.12) becomes Eqn. (2.13).

$$\nabla.\boldsymbol{\sigma} = 0 \tag{2.13}$$

2.2 Preliminary Numerical Analyses

In preliminary analyses, finite element models for three distinct cases taken from literature are built and the results are compared with outputs from their related studies as a preparatory work for the TGM modeling. These are analytical modelling studies of magma solidification in Yosemite National Park in Tuolumne Intrusive Suite-USA, Elbrus Greater Caucasus-Russia and a casting process having similar phenomenon with magma solidification.

Unlike the referenced papers, temperature dependent features are used rather than constant magma and rock properties, which enables exploring a more realistic modelling strategy and gain new insights into the problem domain. By integrating these temperature dependent characteristics, it is aimed to enhance the model's precision and provide a more nuanced insight of the underlying phenomenon. These cases and comparisons of the results are given in the following sections.

2.2.1 Yosemite National Park, USA

Solidification process of a magma chamber in Yosemite National Park, Tuolumne, USA is modelled with the program HEAT by Glazner et al. [81]. To use as a preliminary methodology check, this analysis is rebuilt by using COMSOL Multiphysics with temperature dependent magma and host rock properties taken from the literature for similar silicic magma types found in the regions of preliminary and TGM studies.

The computational domain in the first preliminary analysis is a simplified rectangular magma geometry surrounded by host rock having a width and depth of 60 km and 35 km respectively. Magma has a thickness of 5 km, width of 20 km where its top is positioned at a depth of 15 km. Four points are included in the geometry to collect temperature data as seen in Figure 2.2.

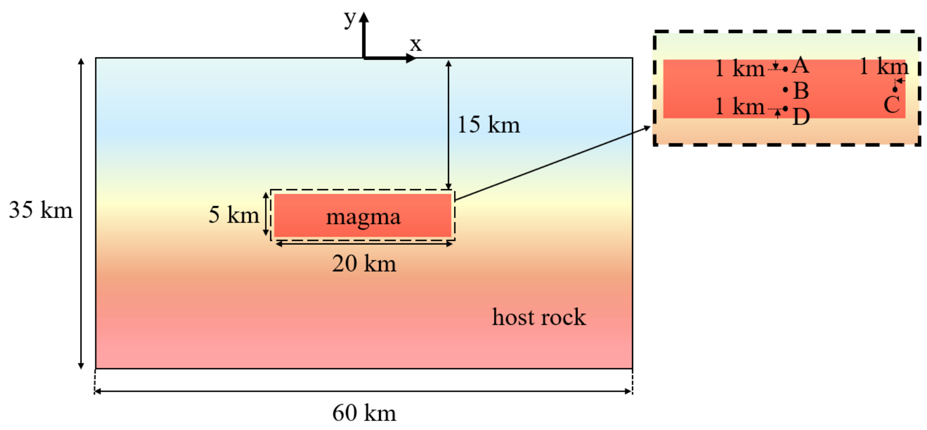

Figure 2.2. Computational domain and data points

Magma has an initial temperature of 900 °C. Host rock is characterized by a geothermal gradient of 20°C increasing per km depth initially where Earth's surface is 20°C as in Eqn. (2.14). Earth's surface, side walls and bottom boundary are also assigned to the same temperature gradient as a boundary condition with Eqn (2.14). Outer boundaries are assigned to constant values by assuming a domain large enough to fit in the general temperature pattern.

$$\mathrm{T}(y) = 20 - 20y \tag{2.14}$$

Magma in the referenced study is silicic in composition. Therefore, magma and host rock materials are taken as granite whose liquid form is one of the most well-known silicate melts such that many of the historical buildings, monuments and sculptures were built from its rock form [82]. Also, it maintains its mineral composition even when exposed to high heat flux and temperatures [83]. Therefore, it is the most accessible and stable magma material by means of literature data and property. In fact, granite also have subgroups as Remiremont granite, charcoal granite, Senones granite etc. but they both have similar behaviors and can be considered as a group. Wang and Konietzky has compilated nine types of granite data and fitted the average values [84]. To provide consistency of the properties of the material, many properties are taken from this study.

Magma and host rock's thermal expansion coefficient behaves according to a piecewise continuous function relation given in Eqn. (2.15) [84].

$$\alpha(\mathrm{T}) = \begin{cases} 8\mathrm{x}10^{-6}\mathrm{x}(0.8383 - 0.00142\mathrm{T})^{(-1/1.7085)}, & 0 \leq \mathrm{T}[°\mathrm{C}] \leq 573 \\ 8\mathrm{x}10^{-6}\mathrm{x}(-5.4160 + 0.0095\mathrm{T})^{(-1/1.5719)}, & 573 \leq \mathrm{T}[°\mathrm{C}] \leq 625 \\ 5\mathrm{x}10^{-3}, & 625 \leq \mathrm{T}[°\mathrm{C}] \leq 800 \end{cases} \tag{2.15}$$

Magma and host rock's specific heat (c_p) values obtained via MELTS software is given with Eqn. (2.16) and shows a tendency to increase up to 680°C which is a value close to the crystallization point [85]. Then, a turn occurs around the crystallization temperature followed by a fall. This is explained by the transition of linear to volumetric expansion at that point [84]. After liquefying, it continuously increases.

$$c_p(\mathrm{T}) = \begin{cases} 820\mathrm{x}(0.9576.59\mathrm{x}10^{-4}\mathrm{T}), & 0 \leq \mathrm{T}[°\mathrm{C}] \leq 573 \\ 820\mathrm{x}(1.173 + 1.238\mathrm{x}10^{-4}\mathrm{T}), & 573 \leq \mathrm{T}[°\mathrm{C}] \leq 1000 \end{cases} \quad (2.16)$$

Magma's thermal conductivity is again temperature dependent, tending to behave as an exponential polynomial between temperatures 0°C and 1200°C as given in Eqn. (2.17) [84]:

$$k(\mathrm{T}) = 2.6\mathrm{x}\left(5.8126 + 6.8485\mathrm{x}0.9995^{\mathrm{T}} + 0.002172\mathrm{T}\right) \quad (2.17)$$

Density of magma is taken as a constant value of 2645 kg/m^3 in parallel with the previous literature studies as it generally does not affect the results significantly but results to a complex model when identified as a temperature dependent variable [86]. Same is applied for Poisson's ratio, the value of 0.25 is assigned as it has the same value, without significant temperature dependence [87]. The latent heat crystallization which is the amount of heat for the solidification of magma per unit mass for silicate melts of granite is 4x10^5 J/kg [88]. Crystallization occurs at temperatures between 680°C and 573°C [84].

Host rock is also characterized by constant density and Poisson's ratio for this preliminary study. The density of the host rock is assigned a value of 2700 kg/m^3, the average density of granodiorite, which is the host rock used in the reference study [66]. The temperature dependence of the Poisson's ratio for host rock is also very low and has been neglected, with the Poisson's ratio set at 0.25. Even for highly dissimilar rocks, this value floats around 0.25 [89].

This analysis encompasses the physics of heat transfer between host rock and magma chamber and phase change of magma. Eqn. (2.5) stands for this analysis as governing equation which is solved with the finite element model. In order to verify the reliability of mesh discretization and make a time step optimization, mesh and time step independence studies are conducted. Three distinct mesh from coarse to refined are generated. Runs are held for a combination of 570, 3898, 4587 mesh elements and 322, 7889 timesteps for a time domain of 31556 Gs which corresponds to 10^6 years. Data consistency is checked with temperature values at Table 2.1 with points mentioned in Figure 2.2 for their values at last time step, 10^6 years.

Table 2.1. Mesh independence study for 322 time steps

Point	Elements	T (℃) (@10^6 years)	Change in T
A	570	614.88	-
	3898	618.67	0.62%
	4587	619.27	0.10%
B	570	660.06	-
	3898	664.22	0.63%
	4587	664.48	0.04%
C	570	545.19	-
	3898	548.63	0.63%
	4587	549.14	0.09%
D	570	678.11	-
	3898	681.41	0.49%
	4587	682.23	0.12%

It is obtained that the results are not influenced significantly after a refined mesh having 4587 elements. Therefore, results are obtained with the refined mesh shown in Figure 2.3.

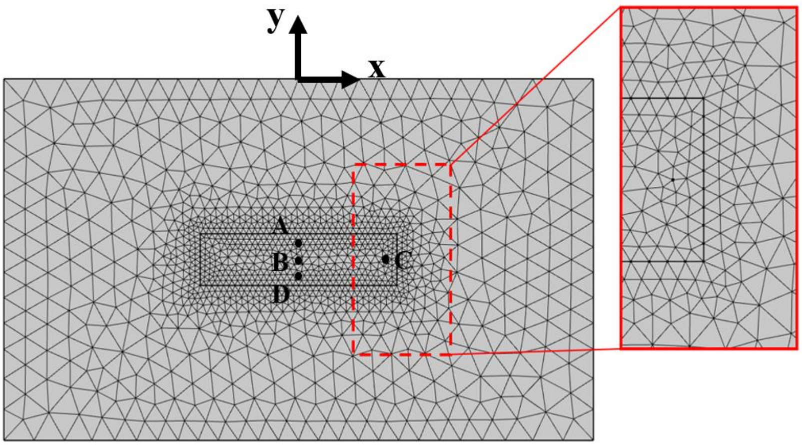

Figure 2.3. Refined mesh with data points

To decide whether the time step used is sufficient or not, transient solver is also computed the results with a step time of 127 years, corresponding to 7889 time steps.

In Table 2.2, it is seen that using 322 time steps is precise enough as its influence on the result is lower than 0.05%.

Table 2.2. Time step independence study for 4587 elements

Point	Number of Time Steps	T (°C) (@10^6 years)	Change in T
A	322	619.27	-
	7889	618.97	-0.05%
B	322	664.48	-
	7889	664.15	-0.05%
C	322	549.14	-
	7889	548.93	-0.04%
D	322	682.23	-
	7889	681.95	-0.04%

2.2.2 Elbrus Greater Caucasus, Russia

Temperature profile of a $6x10^5$ years old dyke shaped silicic magma originated in Elbrus Greater Caucasus, Russia is obtained by Bindeman et al. and in-situ images were captured by SEM Method in University of Alberta [90]. Similar to the study held in Section 2.2.1., a 2D heat transfer model with phase change is built via COMSOL Multiphysics with temperature dependent properties.

A computational domain with 25 km depth and 20 km width has a dyke like amorphous magma accumulation in it. Magma is located in a depth of 3 km to 24 km with maximum and minimum widths of 5 km and 3 km respectively. Magma lacks a distinct shape as it is directly taken from the capture of a real crust area. Point E and point F is located to measure the at coordinates (0,-6) and (3,-13).

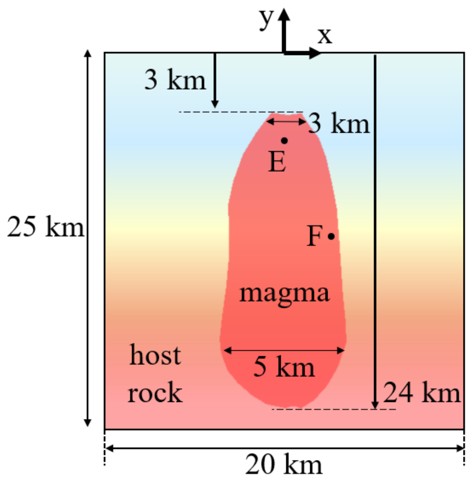

Figure 2.4. Computational domain and data points

At the upper surface of the studied rock domain, temperature value of 100°C is assigned as a constant boundary temperature and an increasing temperature gradient of 20°C per km depth for the host rock domain is present initially. Magma accumulation whose geometry is given in Figure 2.4 has an initial internal temperature of 950°C. Side and bottom domain boundaries are defined with the boundary condition given in Eqn. (2.18).

$$\mathrm{T}(y) = 100 - 20y \tag{2.18}$$

All properties of magma and host rock mentioned in Section 2.2.1 are also used in this model. In the same manner, as the scenario is the same but the geometry and boundary conditions differ from the previous preliminary study, Eqn. (2.5) also stands for this analysis as governing equation.

Mesh and time independence studies are held for three distinct mesh and two distinct time steps in Table 2.3 and Table 2.4. A combination of 810, 1837, 5382 elements and 3787, 541 timesteps for a time domain of $6\text{x}10^5$ years is evaluated. Precision is checked with temperature value at the end of the time domain, $6\text{x}10^5$ years, from the points E and F shown in Figure 2.4.

Table 2.3. Mesh independence study for 3787 time steps

Point	Elements	T (°C) (@6x10^5 years)	Change in T
E	810	571.54	-
	1837	569.07	-0.43%
	5382	567.53	-0.27%
F	810	657.97	-
	1837	660.07	0.32%
	5382	660.50	0.07%

Change in the results drops significantly after a mesh having 1837 elements when the time step is 158 years. However, refining the mesh at conduction boundaries still affects the temperature value at an order of magnitude of 1.5°C. To get rid of any inconsistency, results are obtained with the refined mesh shown in Figure 2.5.

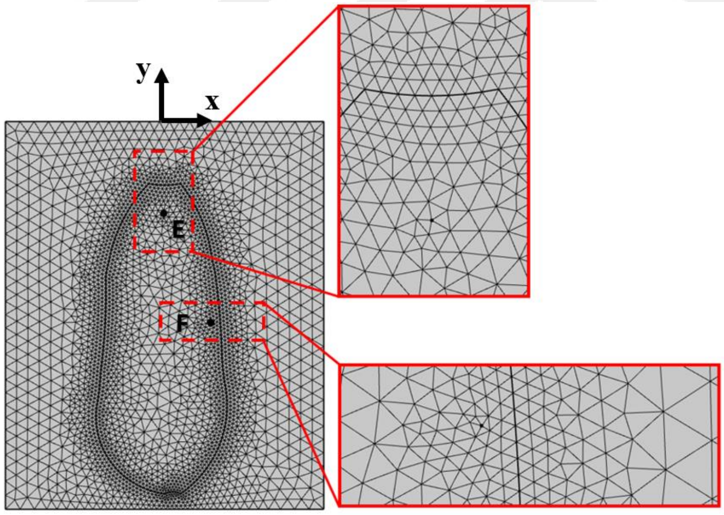

Figure 2.5. Refined mesh with data points

To see whether a smaller number of time steps gives sufficient precision or not, results with a number of time steps of 3787 are obtained. Given the significantly low change in the results and considering computational costs and efforts in Table 2.4, it is seen that using a time step of 1100 years corresponding to the number of time step of 541 is precise enough as its influence on the result is lower than 0.04%.

Table 2.4. Time step independence study for 5382 elements

Point	Number of Time Steps	T (°C) (@6x10^5 years)	Change in T
E	541	569.32	-
	3787	569.07	0.04%
F	541	660.29	-
	3787	660.07	0.03%

2.2.3 3D Casting Analysis

Casting can be evaluated similar to magma chamber solidification as this process is the solidification of molten metal potted in a cavity inside pressed sand which is just like the magma solidifying in a host rock. Both processes have heat transfer, phase change, thermal contraction and solid mechanics physics in it. The primary distinction is that the geometries and time domains dealt with in geological scenarios are in the order of kilometers and years where those in casting are in millimeters and seconds. Considering these two distinct occurrences from different fields of specialization, an analogy is built with these two similar phenomena. A 3D model coupling heat transfer and solid mechanics with temperature dependent properties is developed from an experimental casting scenario studied by Jin et al. [91]. This scenario consists of a melt being poured into a casting die and cooling curve being monitoring for 30 seconds with a DAQ system taking data from 4 thermocouples located 0, 2, 4, 5 mm away from z axis. Figure 2.6 illustrates the process.

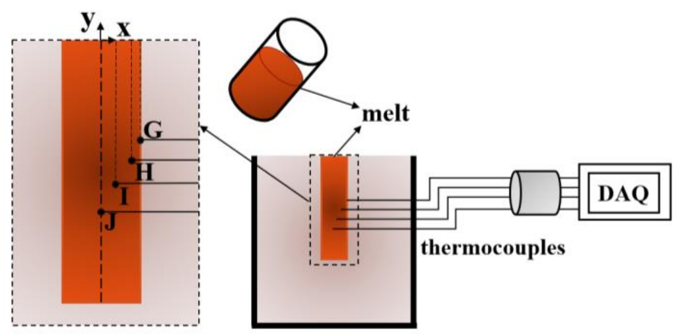

Figure 2.6. Schematic of casting experiment with data points

Computational domain consists of a casting melt poured into a cavity sized 60 mm x 60 mm x 10 mm as illustrated in Figure 2.7. The area surrounding the mold with casting sand is 120 mm x 60 mm x 120 mm in size.

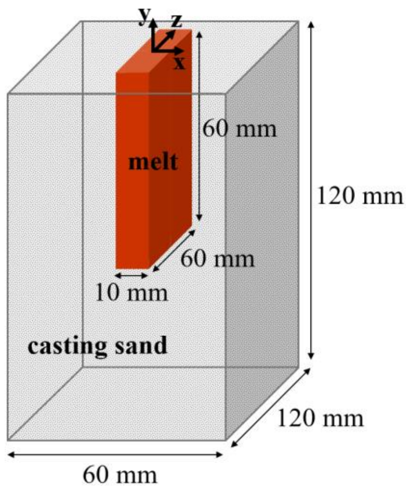

Figure 2.7. Computational domain

The melt is at 1150℃ initially where the surrounding sand is 27℃ without any temperature gradient. Upper surface of the casting sand is taken constant as 27℃ throughout the process and all other temperature values are defined to be initial values. Thermal insulation is assigned to the bottom and side boundaries. Upper surface is free surface and a boundary load of 5 MPa is exerted from all other side boundaries of casting sand, simulating the pretension of casting sand and pressure exerted on the casting mold. This value and melt properties are taken from Tasaki et al.'s study where the pressure on the mold is measured for a domain having a similar order of magnitude of dimensions [92]. Displacement and velocity field for the whole domain is zero initially.

The material of casting sand is not specified in the experimental study, but it is taken as green sand which is a type of specially treated high-pressure molding sand to use in casting processes and defined with temperature dependent properties in COMSOL's material library. On the other hand, casting melt is formed by 5 element alloy (zirconium, titanium, nickel, copper, beryllium). Its properties are tabulated in Table 2.5.

Table 2.5. Properties of casting melt [84, 85]

Casting Melt Property	**Value**
ρ [kg/m^3]	7000
ν	0.2
L [J/kg]	3.2 x10^3
c_p [J/kg°C]	771
T_{cr} [°C]	987
k [W/m°C]	29.93
α [1/°C]	4x10^{-5}
E [GPa]	69

In all previous preliminary models, heat transfer via conduction and phase change occurs. Energy equations for those thermal processes are given in previous sections with Eqn. (2.1)-(2.5). Heat transfer module is built again by introducing casting melt as the phase change material but also coupled with solid mechanics with the addition of thermal expansion different than the previous models. Transient system of equations coupling conductive heat transfer, Eqn. (2.6) and elasticity equations, Eqn. (2.13) are solved.

In this instance, a model simulating this experiment is developed to ensure our methodology and COMSOL's ability to incorporate solid mechanics physics to heat transfer. The outputs of this model are compared with real experimental data measurements. Although the two dynamics involved—one from mechanical engineering and the other from geology—are different, the presence of similar physics in both studies highlights the value of validating the 3D coupled model against experimental data.

Studies are held with three different mesh for a time domain of 30 seconds from the points given in Figure 2.8 for mesh independence study. Temperature is taken at an earlier time of 0.4 seconds. Table 2.6 indicates that 39352 elements are sufficient. Refinement does not cause a significant change in the results but only increases computation time and cost. The mesh is presented in Figure 2.8.

Table 2.6. Mesh independence study results for 30 time steps

Point	Elements	T (°C) (@0.4 s)	Change in T
G	2630	1036.55	-
	39352	1039.08	0.24%
	130271	1039.31	0.02%
H	2630	1024.32	-
	39352	1027.24	0.29%
	130271	1027.56	0.03%
I	2630	1009.14	-
	39352	1012.72	0.35%
	130271	1013.00	0.03%
J	2630	973.87	-
	39352	977.63	0.39%
	130271	978.09	0.05%

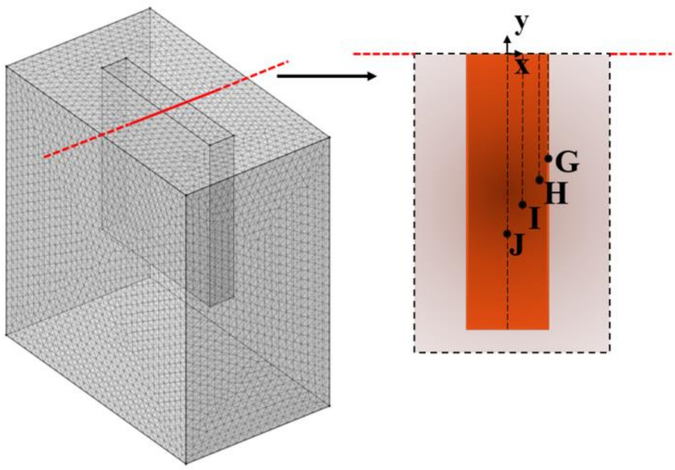

Figure 2.8. Mesh with 39352 elements and data points

The model is run with the selected mesh configuration using three different time steps. Time step independence study which is given in Table 2.7, is evaluated based on the temperature values obtained from two of the data points, G and H.

Table 2.7. Time step independence study results for 39352 elements

Point	Number of Time Steps	T (℃) (@0.4 s)	Change in T
G	10	1039.05	-
	30	1039.08	0.00%
	300	1039.08	0.00%
H	10	1027.04	-
	30	1027.24	0.02%
	300	1027.32	0.01%

As the cooling process takes place too rapidly in this scenario, total time domain is short. Although it increases the significance of time steps, because of the domain's and concept's simplicities, time steps at the order of magnitude of seconds give precise values. In order to avoid inconsistencies caused by inadequate number of computational steps, a time step of 1 second, corresponding to a number of time steps of 30 is selected.

This model gives insights on building a 3D, coupled model of heat transfer and solid mechanics. Based on the outputs and insights obtained from this model, TGM, a 3D, coupled model for the geological process of magma solidification is developed.

2.3 Target Geological Model

In the previous sections, 2D heat transfer models and a 3D coupled model are developed to be compared to data referenced in the literature and overlapping results will be demonstrated in Section 3. With this verified model framework, several cases are generated to represent potential geological scenarios, and a study is performed by varying the geometries and initial conditions. All scenarios are studied as cases both by building a 3D model and a 2D model simulating the midplane section of the 3D model. By incorporating a range of parameter values, these models are aimed to provide an analysis of the underground conditions, enhancing the accuracy and relevance of the simulation results. Outputs for temperature profile and stress distributions are generated for both analyses, the output results are compared.

In literature, many geological cases are simplified and studied with 2D models. However, 2D modeling may not achieve the same level of accuracy as a 3D approach, particularly in complex scenarios where the third dimension plays a crucial role on the distribution of thermal properties and heat transfer. The transition from 2D to 3D modeling is often necessary because 3D models better capture the complexities of spatial variations and boundary conditions, which are crucial in predicting temperature fields and heat flux in real-world applications. Or, contrarily, 3D approach may not always justify the additional computational effort, as the improvements in accuracy might not be significant enough to extend the simulation time. When the distinction between the 2D and 3D model results is minimal, 2D approach might be a more practical choice for scenarios where the added complexity and time required for 3D simulations do not provide a significant benefit. To see if there is a massive contrast between the results of a 3D model and 2D model of the same problem, two models are developed with temperature dependent properties, along with the inclusion of additional physics of solid mechanics, therefore more accurately simulating the real-life underground conditions. Scenario of the geological case to be studied is explained in the following section.

2.3.1 Computational Domain

The scenario to be analyzed is a host rock domain having three magma chambers in it. The settlement depths of chambers are examined in 12 distinct cases for different depth and initial magma temperatures. Configuration of magma chambers are changed to examine different cases but the host rock remains unchanged.

2.3.1.1 Three-Dimensional Domain

Three dimensional analysis domain consists of a block of host rock with dimensions of 80 km width, 30 km length, 30 km depth and three magma chambers in it. Magma chamber geometries are 30x5x5 km, 20x3x3 km, 5x1x1 km ellipsoidal formations filled with magma. They are taken as ellipsoidal because it is a typical geometry both used widely in the literature and also monitored in field observations, enabling it to simulate real conditions [93,94]. However, it should be noted that consideration of a different geometry as a dyke like vertical ellipsoidal surely leads to a significantly different stress concentrations [52]. İllustration of the domain is given in Figure 2.9.

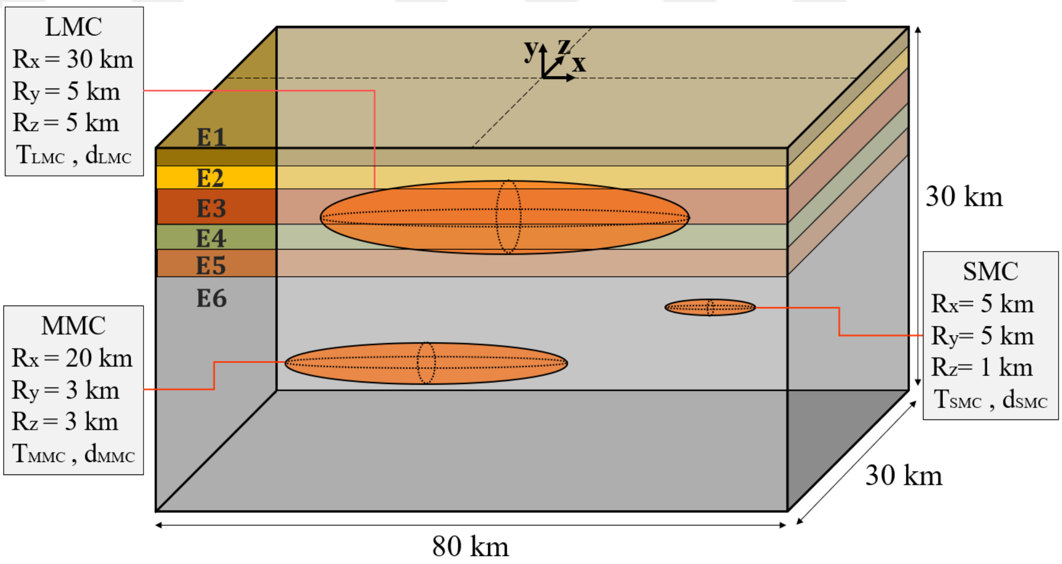

Figure 2.9. 3D computational crust domain

Large magma chamber (LMC) is the biggest chamber having 30x5x5 km dimensions, middle magma chamber (MMC) is the one with 20x3x3 km and small magma chamber (SMC) is the smallest one with 5x1x1 km size. Runs are held for different magma chamber settlement depths of 3 km, 8 km and 12 km because it both affects the cooling process and mechanical stress locations as mentioned in Gudmundsson's previous studies [72]. Depth of chambers are denoted with d; LMC, MMC and SMC have depths of d_{LMC}, d_{MMC} and d_{SMC} respectively.

Host rock domain has 6 different layers having different Young's modulus values in order to simulate the real case in nature. In the real natural case, temperature increases with depth [95] and each subsurface layer has different stifness values according to their composition [26,96]. Both for simulating real case and see the effect of Young's modulus in a pattern, E of layers are given as a synthesis of literature data. This pattern is formed by considering the Mount Rogers area, Virginia, USA because many detailed properties have been studied for this volcanic area having silicic magma, enabling to synthesize the info cited from Radford University's geology page and studies of Molina and Brown [97-99]. All the layers in the region are determined by matching the properties of rocks found in the literature. For the 3D model, host rock geometry is defined as 6 layers having the properties given in Table 2.8. Each layer is defined as E# because the property varying significantly is the Young's modulus.

Table 2.8. Host rock layers and properties

Rock Type	**Explanation**	**Layer**	**E [GPa]**	**Depth [km]**	**ρ [kg/m^3]**
Unicoi Formation	Sandstone and shale [88, 97, 98, 100]	E1	18	0.5	2349
Konnarock Formation	Conglometare, diamicite and sandstone [97, 99, 101]	E2	30	1.1	2349
Upper Part of Mount Rogers Formation	Tuff and rhyolite [97, 101]	E3	35	1.8	2600
Lower Part of Mount Rogers Formation	Rhyolite [97, 101]	E4	50	1.2	2800
Cranberry Gneiss	Marble, granitic gneiss [97]	E5	40	1.4	2800
Lower crustal rocks	Gabbro, diorite, granulite	E6	80	24	3200

For all other host rock and magma properties, values in Section 2.2.1 are used. Young's modulus of host rock and magma are not necessary for the previous studies because the physics used in them is only heat transfer. For the coupled model, temperature dependent E value for magma is used.

Magma Young's modulus tends to decrease as temperature increases and identified as an interval function for granite as given in Eqn. (2.19) [102]. At the point it rapidly decreases, it is understood that microcracking changing the inner structure, causing new spaces reducing the thermal expansion.

$$E(T) = \begin{cases} 37.35x\,1.2665/\left(1 + e^{-1.430+0.0034T}\right), & 0 \leq T[°C] \leq 600 \\ 37.35\,/(-109.953 + 17.542\ln(T)), & 600 < T[°C] \leq 1250 \end{cases} \quad (2.19)$$

2.3.1.2 Two-Dimensional Domain

2D domain is the x-y cross section of the 3D domain passing from the centers of the chambers. It is again formed by host rock with dimensions of 80 km width, 30 km length, having 6 different layers and three magma chambers. Magma chambers are the same as in 3D analysis; only having 2D ellipse geometries of 30x5 km, 20x3 km, 5x1 km. All properties are the same as used in the 3D analysis. 2D domain is given in Figure 2.10.

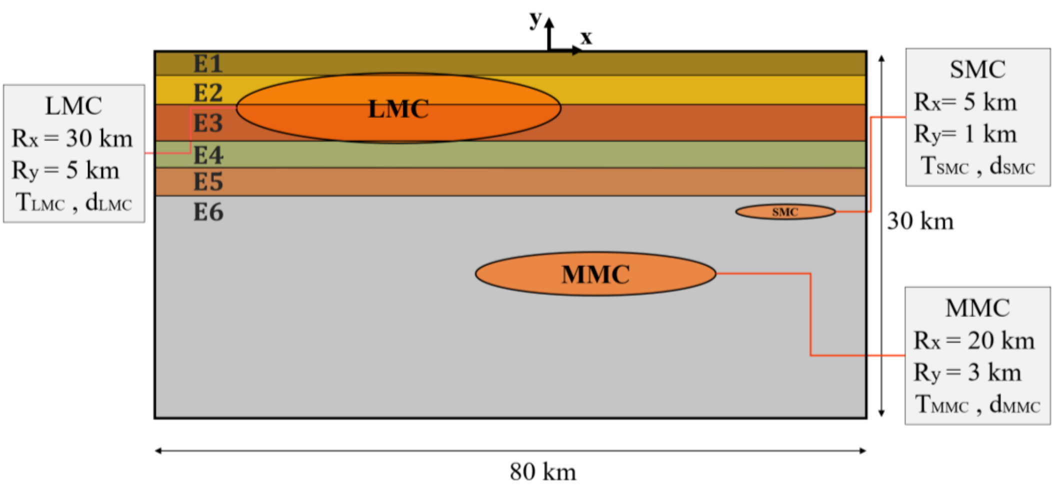

Figure 2.10. 2D computational crust domain

For both model setups, heat transfer physics is coupled with solid mechanics via thermal expansion. Related governing equations are Eqn. (2.6) and Eqn. (2.13) which are derived and indicated in Section 2.1.

2.3.2 Initial and Boundary Conditions

For heat transfer module, temperature of the domain's upper surface corresponding to Earth's surface is set to the constant value of 15°C. As in Eqn. (2.20), an increasing temperature gradient of 25°C per km depth is assigned to side and bottom walls as a boundary condition and to all the host rock layers as an initial condition.

$$T(y) = 15 - 25y \tag{2.20}$$

Magma chamber internal temperatures are one of the controlled variables and refer directly to the initial temperature of magma. Internal temperature of magma chamber is defined as an initial condition on heat transfer module as 700°C, 800°C and 900°C according to the case application. Initial internal temperature values of magma chambers are denoted by T_{LMC}, T_{MMC}, T_{SMC} for LMC, MMC and SMC respectively.

In solid mechanics module, bottom and lateral boundaries of the domain are fixed with a prescribed velocity of zero. Magma excess pressure (P_e) which is the load applied on chamber boundaries by magma is given as an initial pressure of 5 MPa as in Figure 2.11 because this value corresponds to the in situ inner chamber pressure and a sufficient value to illustrate the effects without dominating the results [89].

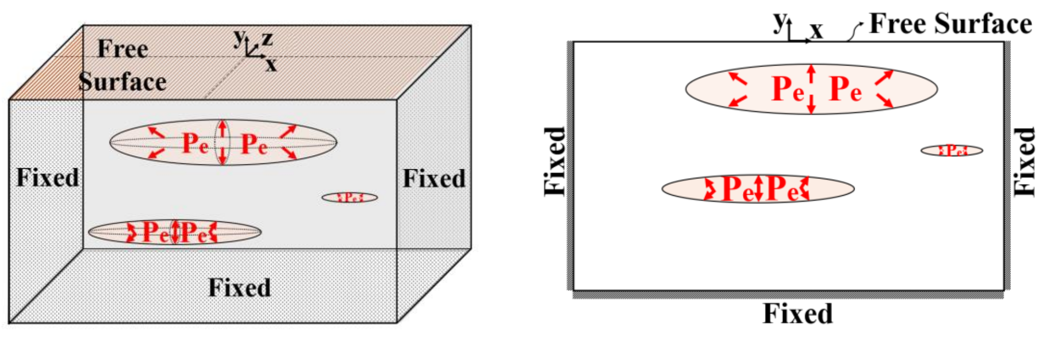

Figure 2.11. Boundary conditions of the 3D and 2D domains

Although topography may affect near stress fields closer to surface, as the aim is to make a comparison on the 2D and 3D model outputs of thermally induced mechanical effects around chambers elevated differently and at different temperatures in a large domain, topography effects are considered negligible and left as a further study. Therefore, top of host rock, which is the Earth's surface is a principal stress plane taken as a flat and free surface [22].

Regional extensions and compressions lead by the tectonic plate displacements effect the stresses around magma chambers [26]. For instance, a tectonic layer displaces 20mm per year where the other might remain constant or this displacement can also be relative. The difference caused by the unequal motion cause stresses between layers. In this study, as the main aim is seeing the differences between 2D and 3D analyses' results, no relative motion is studied. Therefore, host rock domain is not subjected to any external loadings.

2.3.3 Numerical Study Matrix

The magma chambers' settlement depths are examined in 3 different values as 3 km, 8 km and 12 km below the Earth's surface. Similarly, initial internal temperatures of chambers are also specified as 700°C, 800°C and 900°C in turn. Chamber depths and temperatures vary according to cases in order to see the effect of these parameters on host rock. These cases are named with respect to these various settlement depth and initial internal temperature values. Coding for defining the case is given in Figure 2.12 and examples are given in Figure 2.13.

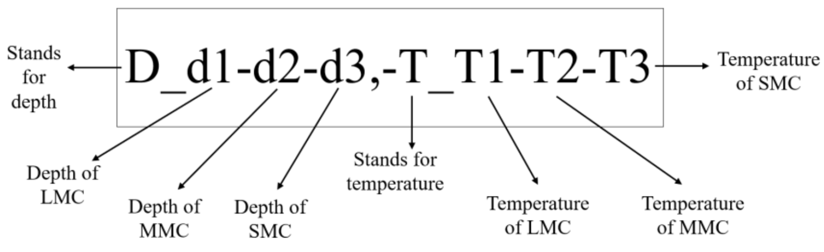

Figure 2.12. Coding of cases

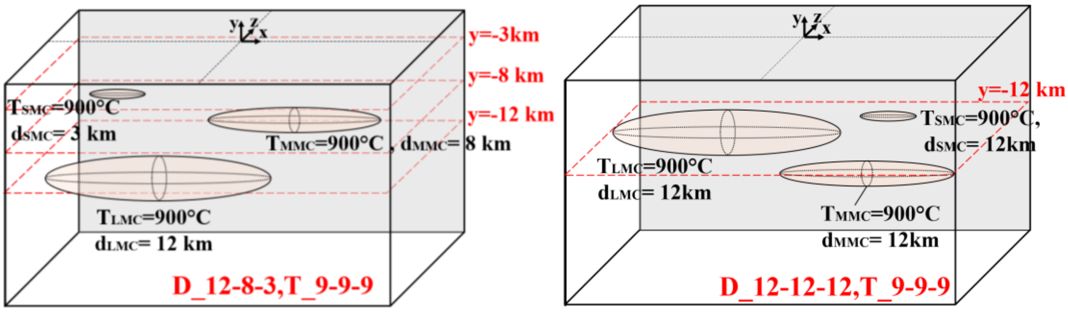

Figure 2.13. Various configurations with case codes

2.3.4 Mesh and Time Independence Study

The FEM models including 2D and 3D approaches, mesh discretization, numerical computations and computational optimizations are held with COMSOL Multiphysics® version 6.1 [78]. Heat transfer and solid mechanics modules are coupled with thermal expansion and phase change physics as multi physics study.

To check whether the mesh or time step gives precise data, temperature value at the center of LMC (Point X in 2D and Point Y in 3D) is tracked for both 2D and 3D models. Mesh independence study is held for the geometries of case D_3-3-3, T_9-9-9.

2.3.4.1.1 2D

Four different meshes for a time domain of 15×10^4 Gs, which corresponds approximately to 4.75×10^6 years is analyzed. Dynamic changes at the boundary of LMC occurs before its total solidification, which corresponds to 4.75×10^5 years. Therefore, for mesh independence study, temperature data is taken at an earlier time of 4×10^4 years. Table 2.9 indicates that mesh having 49953 elements is fine enough to get precise data. Selected mesh is given in Figure 2.14.

Table 2.9. Mesh independence study results for 800 time steps

Point	Elements	T (°C) (@4x10^4 years)	Change in T
X	4266	888.84	-
	22396	889.11	0.03%
	49953	889.27	0.02%
	298741	889.45	0.02%

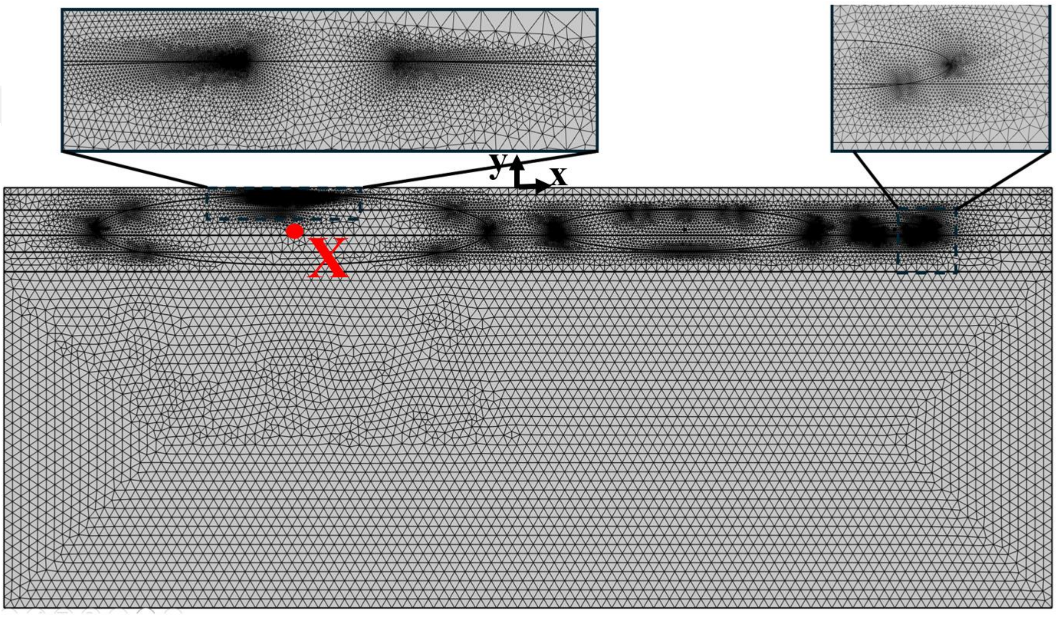

Figure 2.14. Refined mesh with data point

The mesh includes a maximum element size of 0.5 km at the outer host rock domain boundaries and a minimum size of 0.015 km at chamber boundaries, enabling more accurate calculations at the conduction interfaces. The mesh having higher number of elements has the size of 0.075 km at outer host rock domain boundaries and it is evident that mesh refinement in those areas does not specifically affect the output while increasing computation cost. For finding the optimum time step, computations are held for three different time steps of 10, 100 and 1000 years for a total time domain of 4.75x10^6 years.

Table 2.10. Time step independence study results for 44696 elements

Point	Number of Time Steps	T (°C) (@4x10^4 years)	Change in T
X	150	889.44	-
	1500	889.27	-0.02%
	15000	889.44	0.02%

Table 2.10 clearly indicates that using the time step of 100 years which corresponds to 1500 time steps is fully adequate. Computation time for the selected mesh and time step is a maximum of two hours with a 16GB DDR4 RAM.

2.3.4.1.2 3D

Mesh independence study is held for four different mesh configurations for the 3D model. Because the domain is huge and the coupled solution have complexities, computation time becomes extensively high as the number of elements increase. Therefore, greater number of mesh configurations are observed to save computational time. All 3D analyses are held with a time step of 100 years, corresponds to a number of 1500 time steps and temperature data is taken at 4x10^{4th} year from the center of LMC, point Y, as in the 2D analysis. Time independence study is not held for 3D model since it has already done for the same scenario at 2D analyses.

Table 2.11. Mesh independence study results for 800 time steps

Point	Elements	T (°C) (@4x10^4 years)	Change in T
Y	16,402	903.45	-
	37,691	888.5	1.65%
	132,904	883.78	0.53%
	575,511	882.07	0.19%

Table 2.11 shows that, when high computational time and the deviations in the results are considered, a mesh with 132904 elements is precise enough. As in the 2D study, finer meshes are implemented near the magma chamber, where the gradients are higher, while coarser elements are used away from the magma chamber. Size of the elements are 1 km at outer host rock domain boundaries and 0.15 km at chamber boundaries. Computation time for the selected mesh and time step is a maximum of 1.5 day with a 16GB DDR4 RAM.

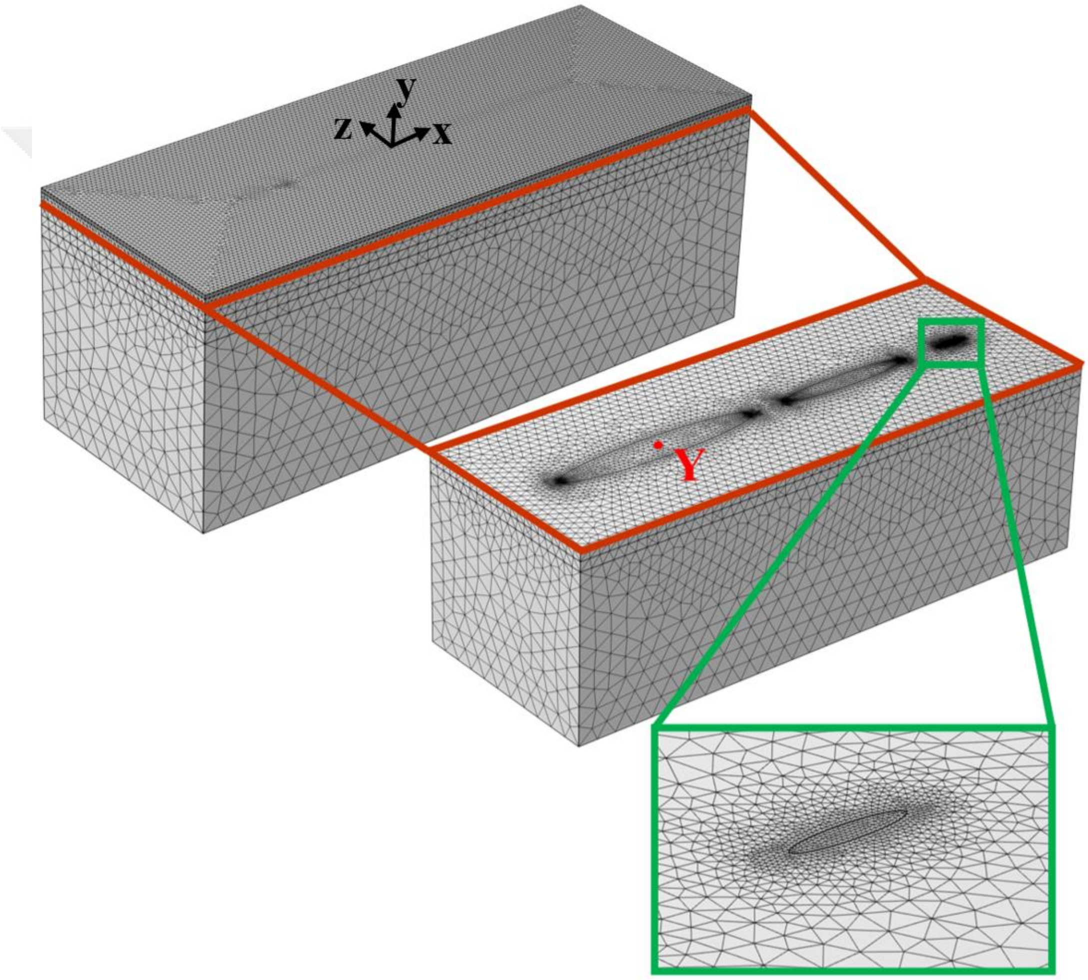

Figure 2.15. Refined mesh with data point

CHAPTER 3

RESULTS AND DISCUSSION

Finite element model outputs, magma solidification process, time and stress distributions are given in this section with FEM analyses results.

3.1 Preliminary Analyses Results

For magma to totally solidify and become rock structure, high amount of time with a rank of thousands of years is a likely result for both cases. The results obtained are consistent with the existing literature data, which reinforces the reliability of the newly developed models. However, it is important to note that all these studies are model-based, and as such, their accuracy cannot be fully guaranteed. The inherent limitations of model-based approaches mean that while our findings align with previous results, the ultimate validation of these models remains an ongoing challenge.

3.1.1 Yosemite National Park, USA

Results are obtained for 32,600 Gs which corresponds to about 10^6 years. Glazner et al.'s paper has the output for temperature of four data points through the total time domain [81]. Temperature profiles obtained from the 2D FEM model in this study are plotted in Figure 3.1 for points A, B, C, D which are shown in Figure 3.2. The general pattern fits and gives the same results with the referenced study with a maximum error of 6.25%. It can be explained with the temperature dependent properties exerted in the newly developed model.

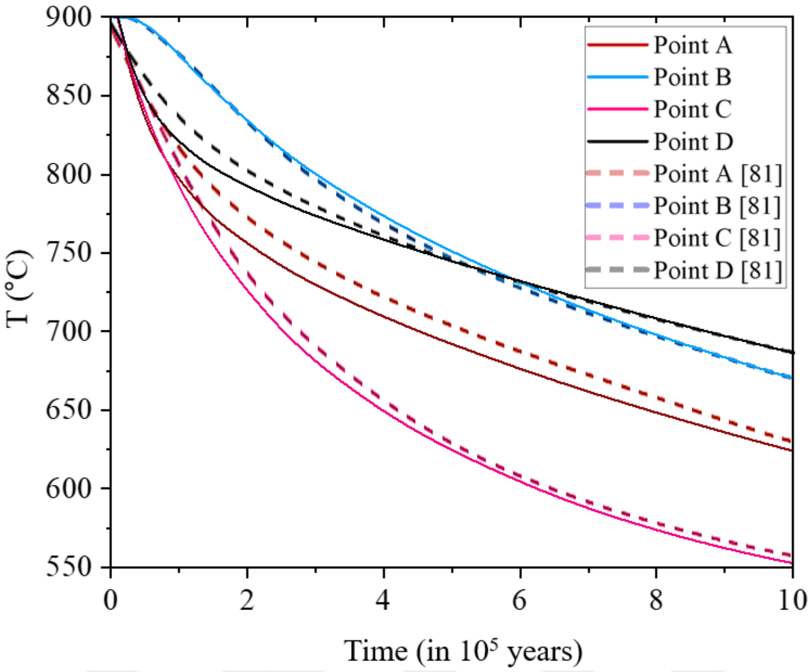

Figure 3.1. Temperature profiles

Temperature distribution at the end of 10^6 years is given in Figure 3.2 showing that magma mostly crystallized as the maximum temperature value is lower than the temperature which magma starts crystallizing (680°C), but higher than the total solidification temperature (573°C). Therefore, the solidification time for this scenario is greater than 10^6 years and steady state has not yet been reached.

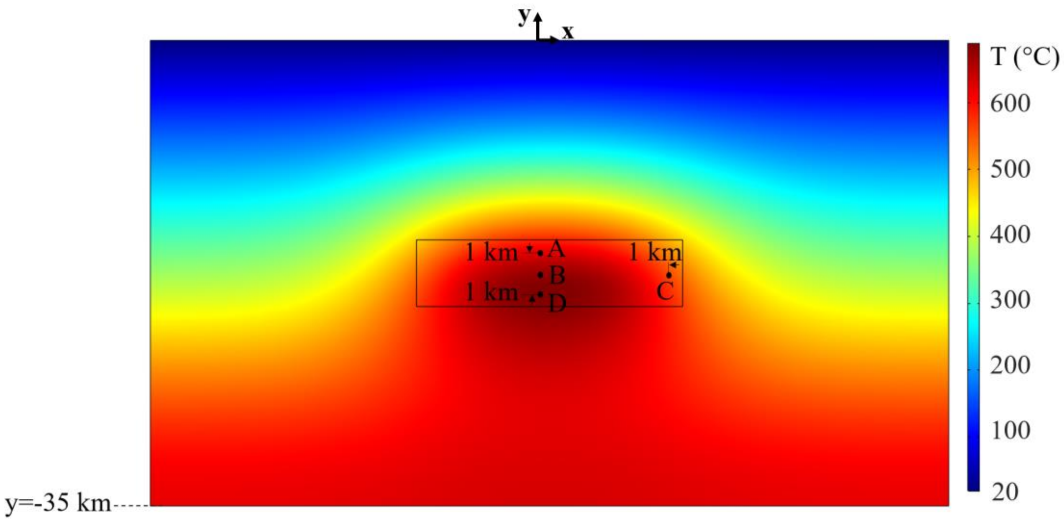

Figure 3.2. Temperature distribution at 10^6 year

3.1.2 Elbrus Greater Caucasus, Russia

In scope of this scenario, runs are held for a time domain of $6x10^5$ years. Temperature data is given in Figure 3.3 for points E and F shown in Figure 3.4.

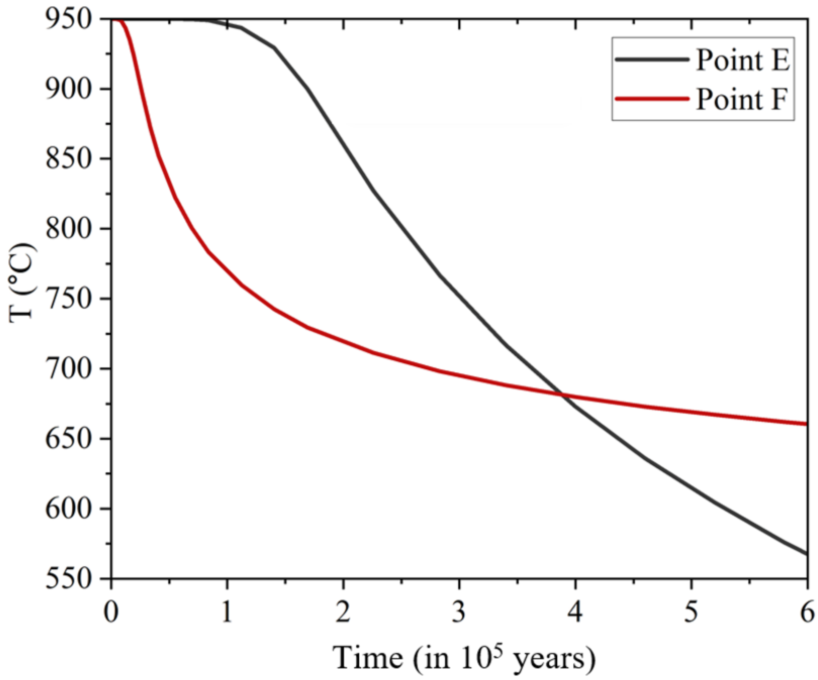

Figure 3.3. Temperature profiles

Temperature change with time for points E and F are outputted. Starting with a rapid temperature drop because of being close to the solid-liquid interface, point F fits to the temperature value around 650°C. Conversely, point E preserved its temperature for a significant initial time period because it is surrounded by a large body of high temperature magma. However, as the surrounding magma cooled and solidified, Point E gradually approached the solid-liquid interface, eventually lying directly on it. Finally, due to the relatively low temperature of the host rock domain, the temperature at Point E dropped below the phase change temperature, leading to complete solidification. After $6x10^5$ years, temperature distribution of the domain obtained for the end of this time domain which enables us to make comparison with the literature data is given in Figure 3.4.

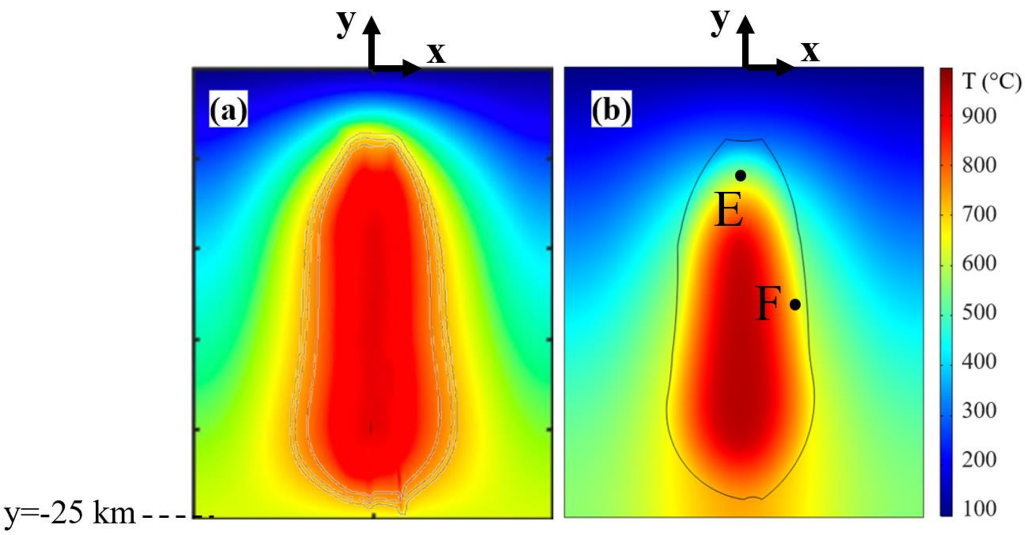

Figure 3.4. Temperature distributions at 600000th year for (a) the model referenced in Glazner's study [81] and (b) developed model

It can clearly be seen that the magma is still not solidified completely but started to crystallize from outer boundaries. As the host rock has a temperature gradient increasing with depth, significant solidification and cooling of magma at the upper part of the chamber domain is observed.

Temperature distribution at Figure 3.4 fits with the distribution data outputted in Bindeman et al.'s study in the literature [91] enabling the preliminary model to be verified by means of heat transfer and material properties and model methodology.

3.1.3 3D Casting Analysis

Casting experiment in the referenced Jin's studies [92] gives temperature outputs for 4 points taken with thermocouples for the whole-time domain. For the validation of the 3D coupled thermomechanical model, output values of the model and the literature data are compared. Temperature profiles through the time domain can be seen in Figure 3.5.

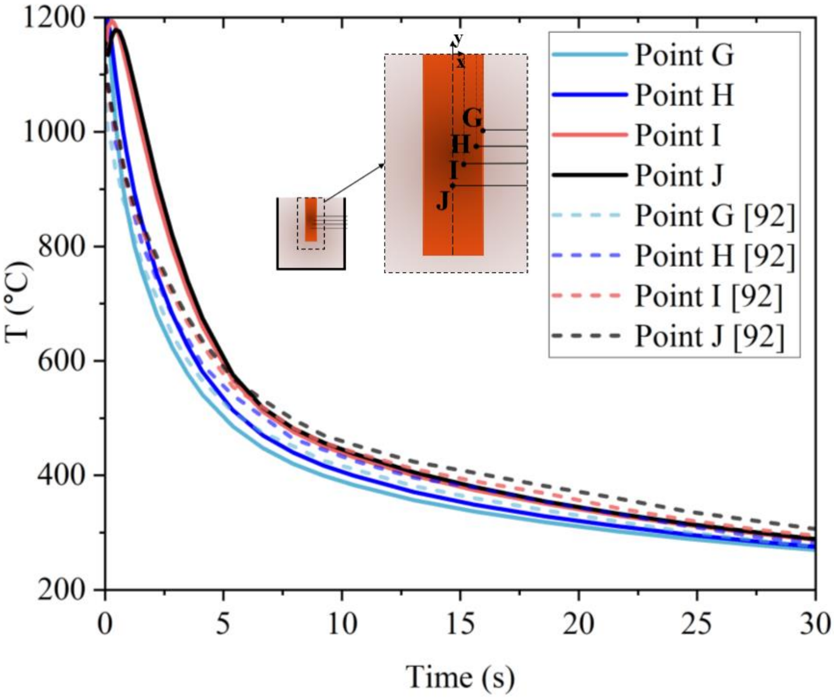

Figure 3.5. Temperature profiles

Temperature distributions over time fit to the profile in the referenced paper with a maximum error of 22% occurring at the beginning of the time period (0-3 seconds) at point J. It is assumed that this error is caused because of the unclear material properties of the melt and sand around mold. In the experiment, initial cooling process occurs too rapidly, might be caused because of the higher thermal conductivity value in the real experiment caused by alloy difference. End of the process overlaps with the model output, as process is dominated by phase change, rather than heat transfer between the mold and casting sand.

3.2 Target Geological Model Results

From previous discussions and preliminary models, an exponentially decreasing temperature profile is expected for the regions in magma chambers. Stresses are expected to concentrate around magma chambers, therefore highest stress concentrations are supposed to be around them. As the shape of magma chambers are ellipsoidal and have edge like geometries at the lateral axis, stress areas are likely to occur at those lateral edges as indicated in Section 1.1. All the results of thermal and solid mechanics are indicated in this section.

3.2.1 Solidification and Temperature Distributions

This section discusses the solidification process and temperature distributions observed within the magma chambers, highlighting key findings from the simulations. The computations are conducted for $15x10^4$ Gs, which corresponds approximately to $4.75x10^6$ years. The system reaches thermal equilibrium in a maximum of $5x10^6$ years for all cases but the change in the system becomes too slight after $4.5x10^6$ years for 2D and $3x10^6$ years for 3D. The entire time domain up to the steady state has been analyzed. Temperature profiles for all cases through the whole time domain and for the center point of chambers obtained from the 2D analyses are given in Figures 3.6-3.17.

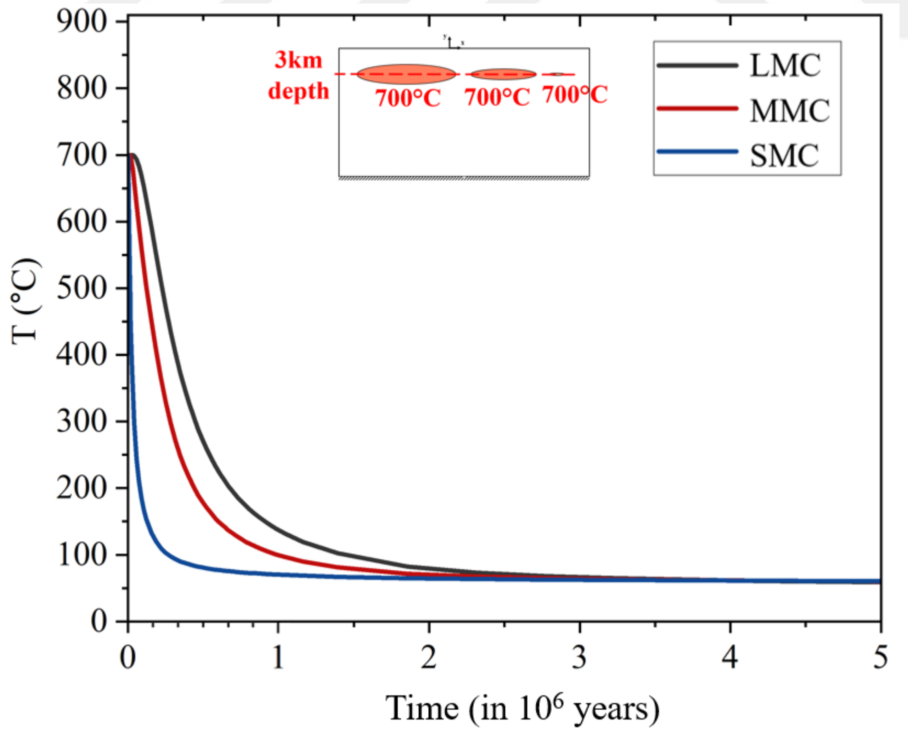

Figure 3.6. Temperature profile - D_3-3-3, T_7-7-7 (2D)

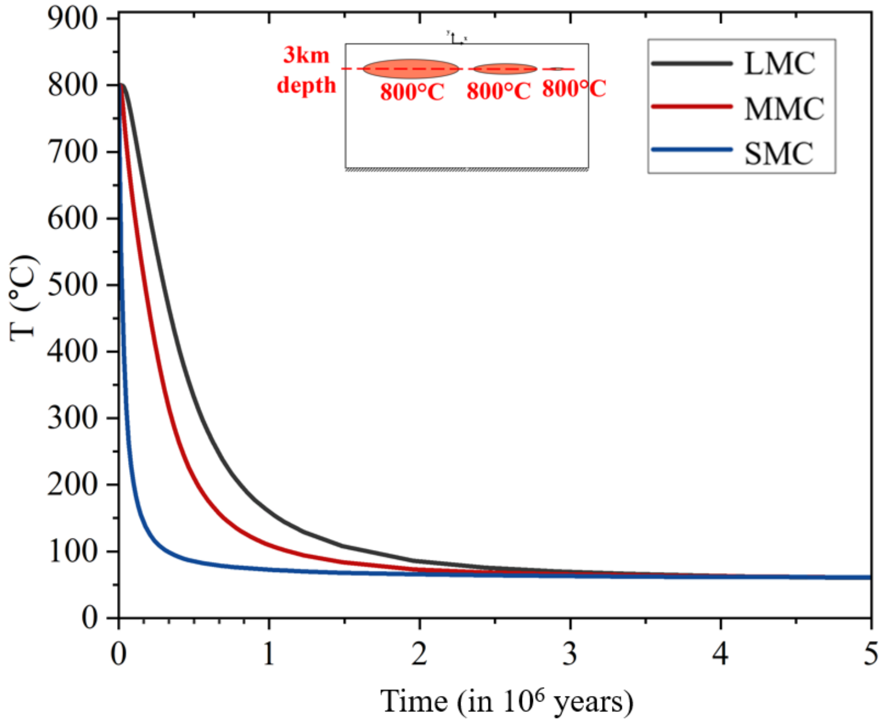

Figure 3.7. Temperature profile - D_3-3-3, T_8-8-8 (2D)

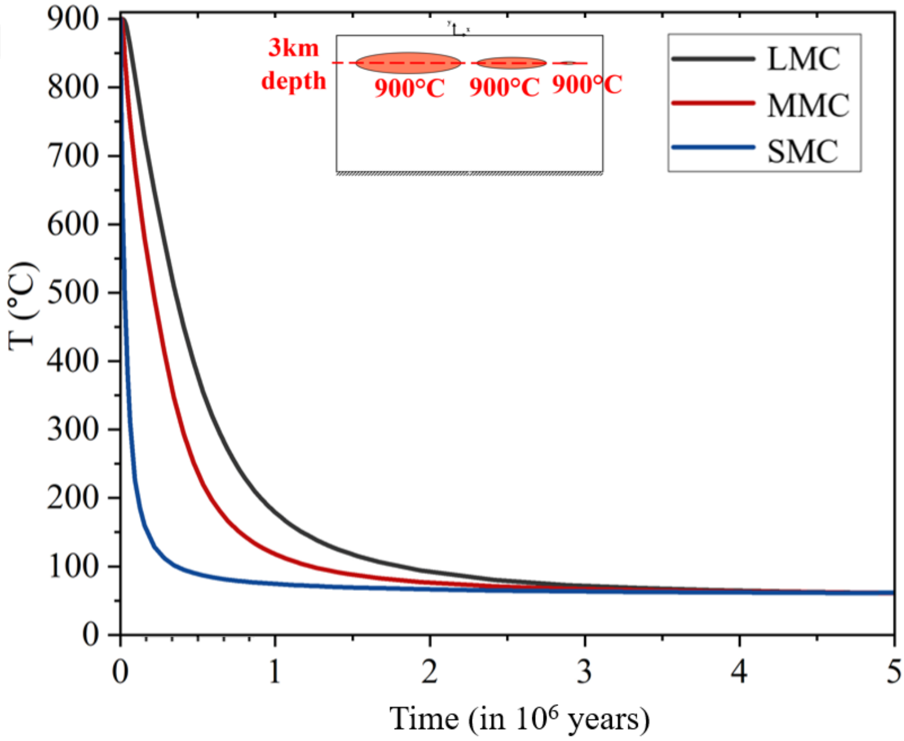

Figure 3.8. Temperature profile - D_3-3-3, T_9-9-9 (2D)

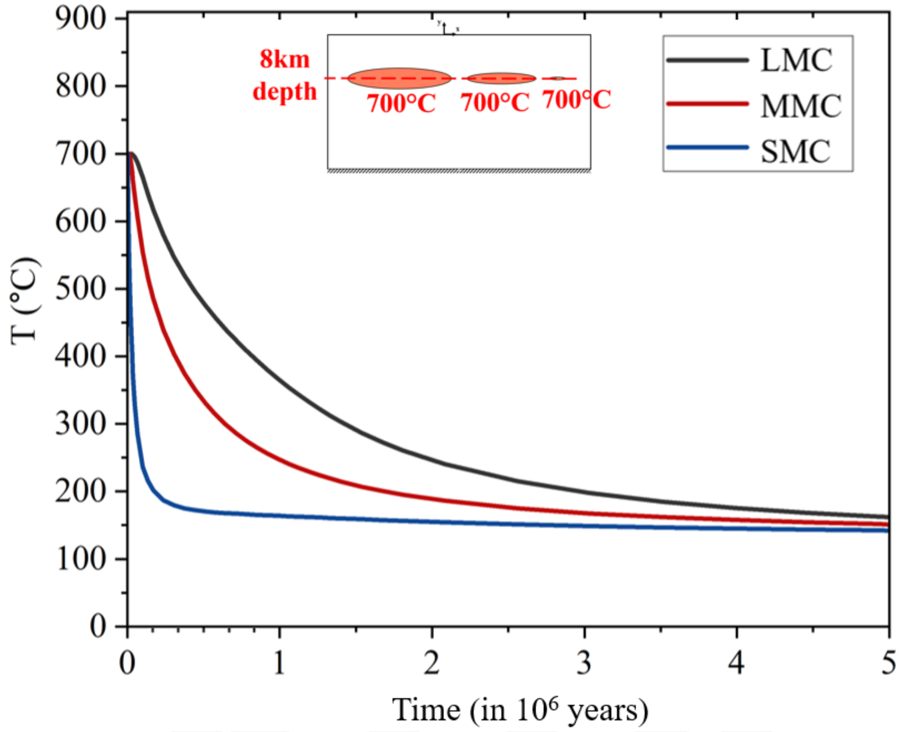

Figure 3.9. Temperature profile - D_8-8-8, T_7-7-7 (2D)

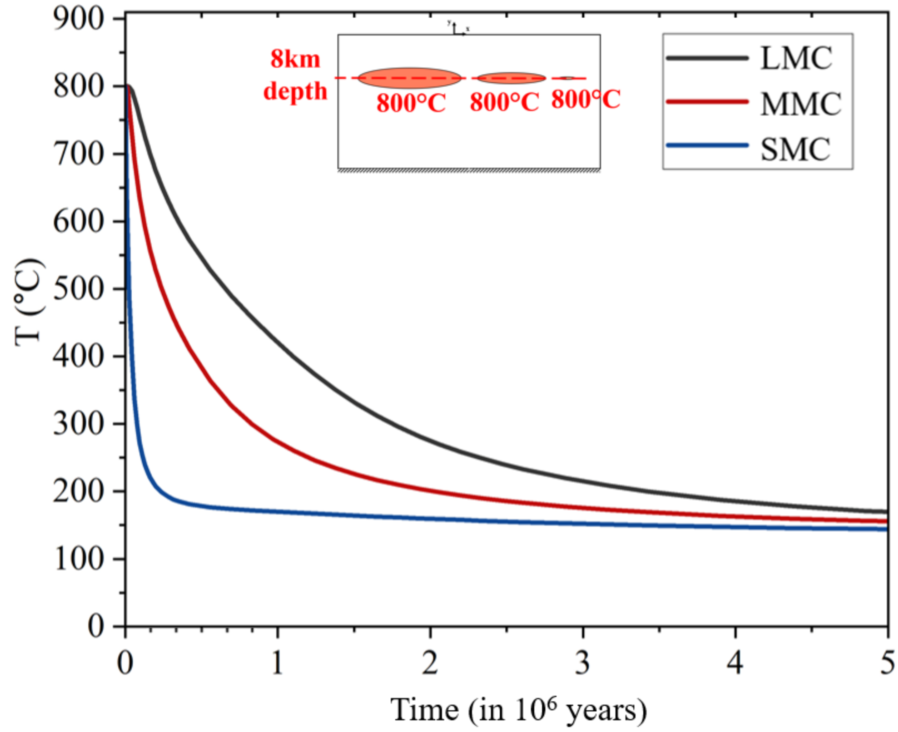

Figure 3.10. Temperature profile - D_8-8-8, T_8-8-8 (2D)

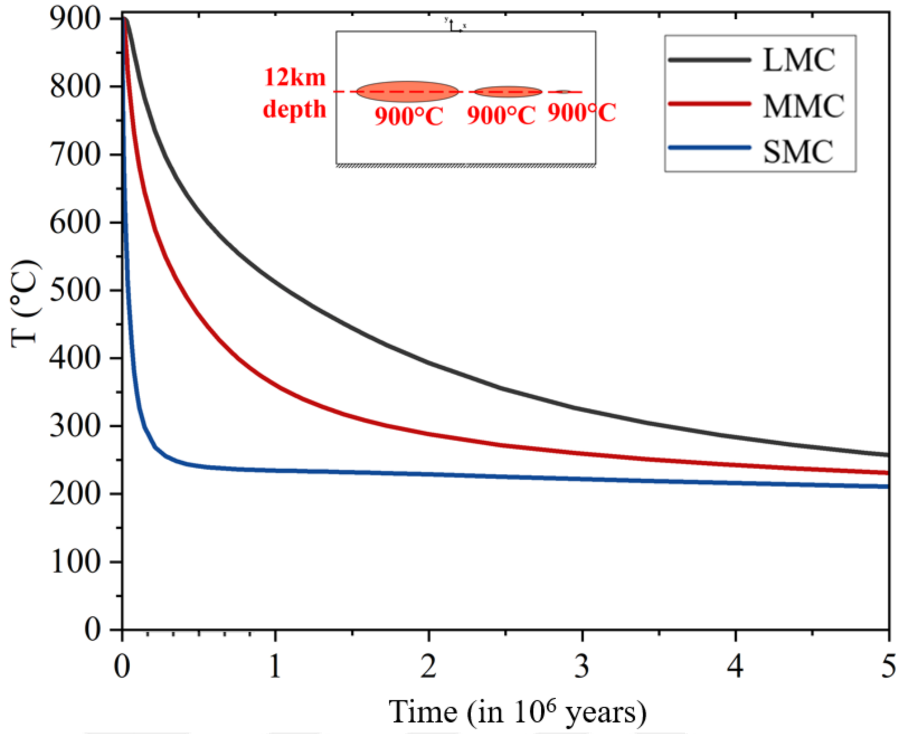

Figure 3.11. Temperature profile - D_12-12-12, T_9-9-9 (2D)

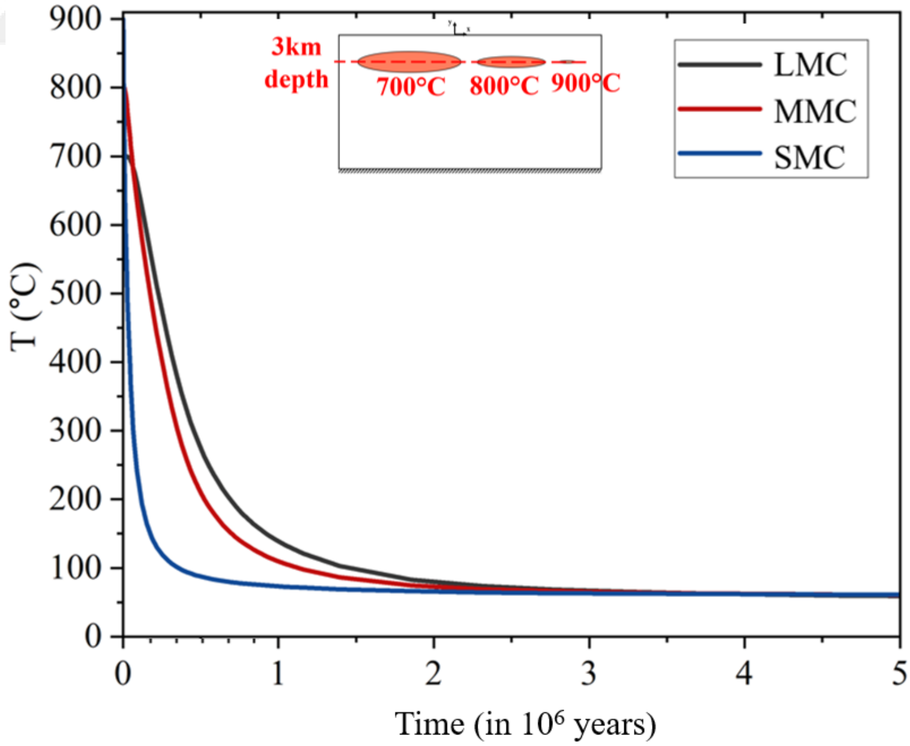

Figure 3.12. Temperature profile - D_3-3-3, T_7-8-9 (2D)

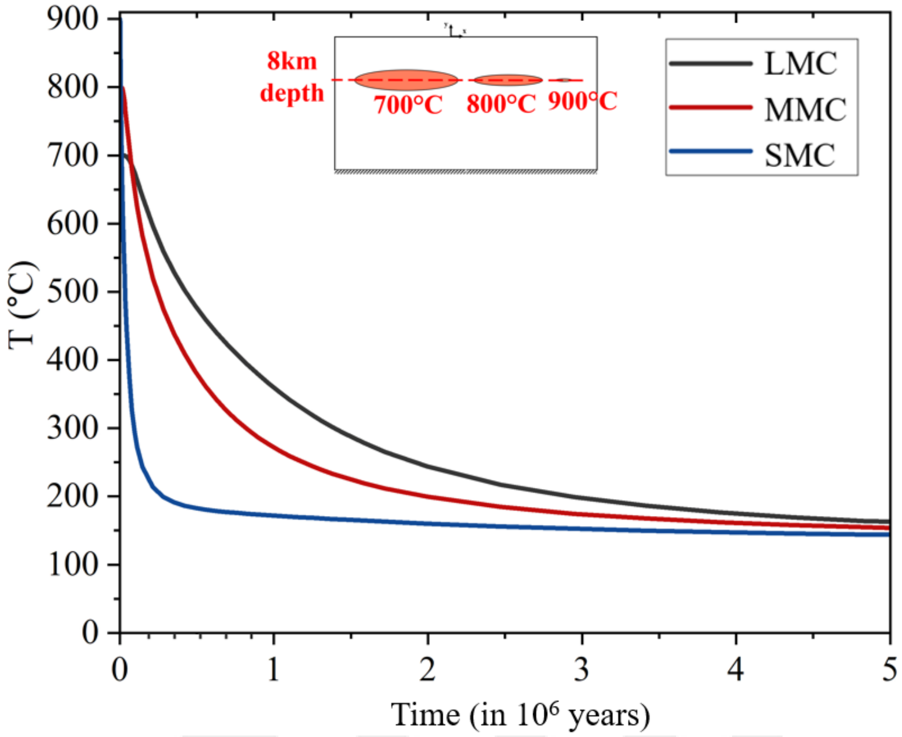

Figure 3.13. Temperature profile - D_8-8-8, T_7-8-9 (2D)

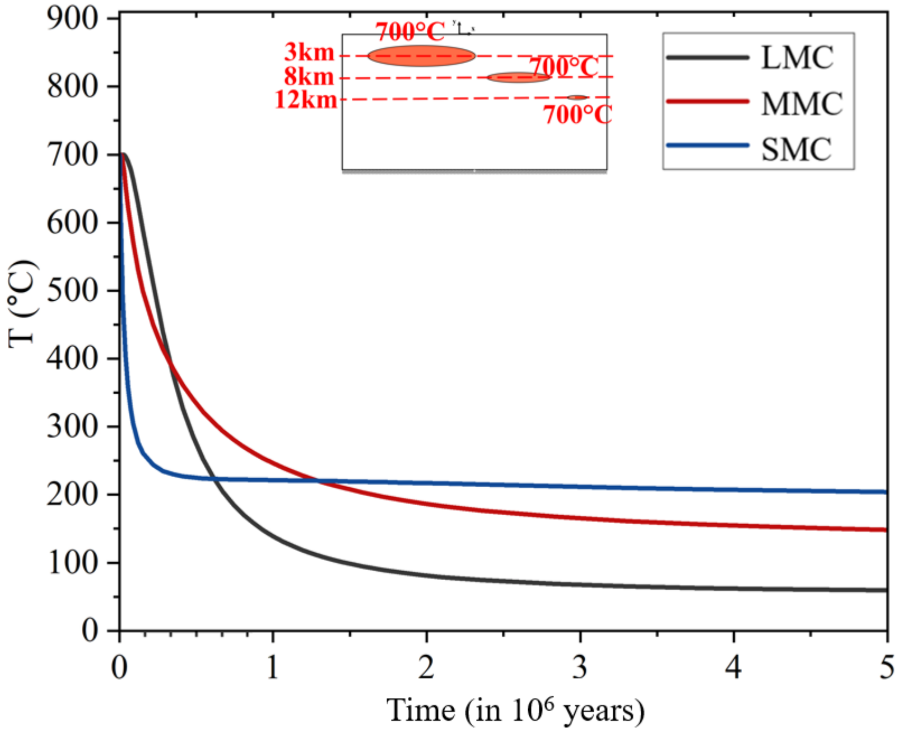

Figure 3.14. Temperature profile - D_3-8-12, T_7-7-7 (2D)

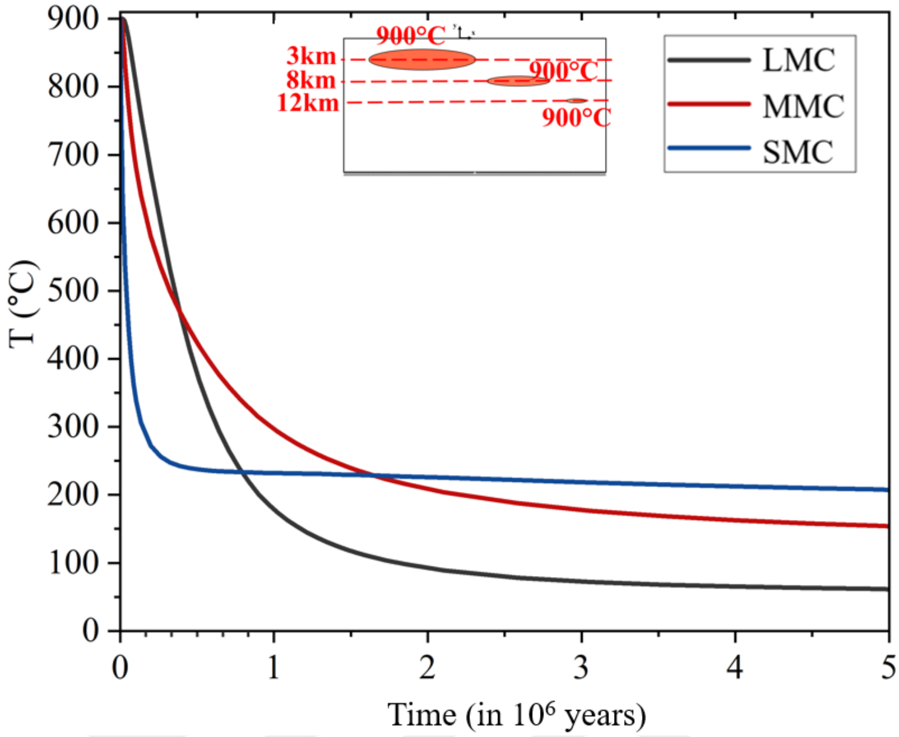

Figure 3.15. Temperature profile - D_3-8-12, T_9-9-9 (2D)

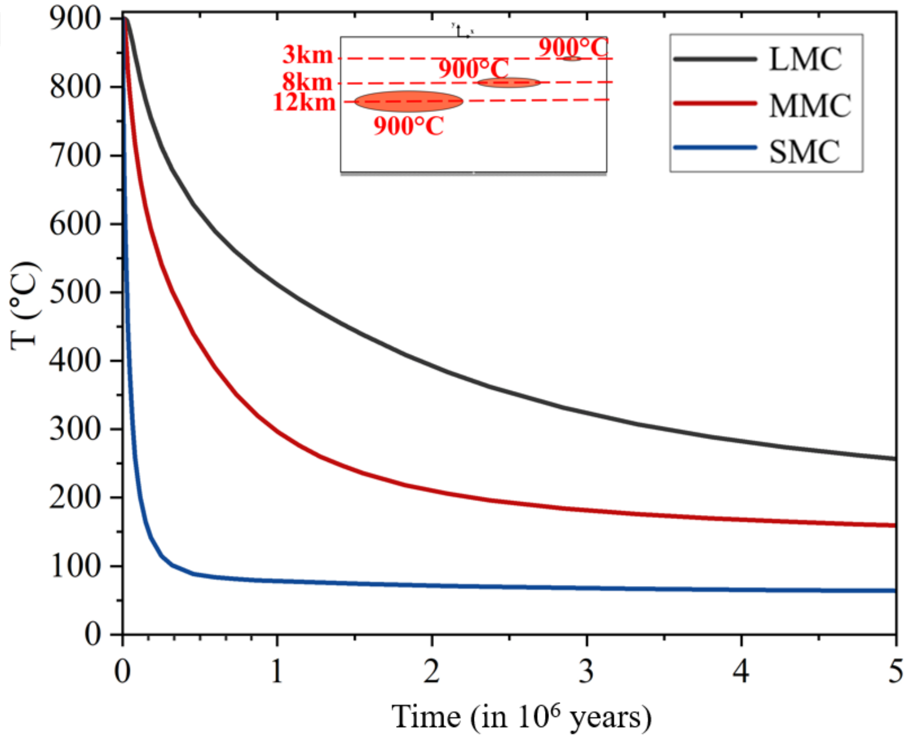

Figure 3.16. Temperature profile - D_12-8-3, T_9-9-9 (2D)

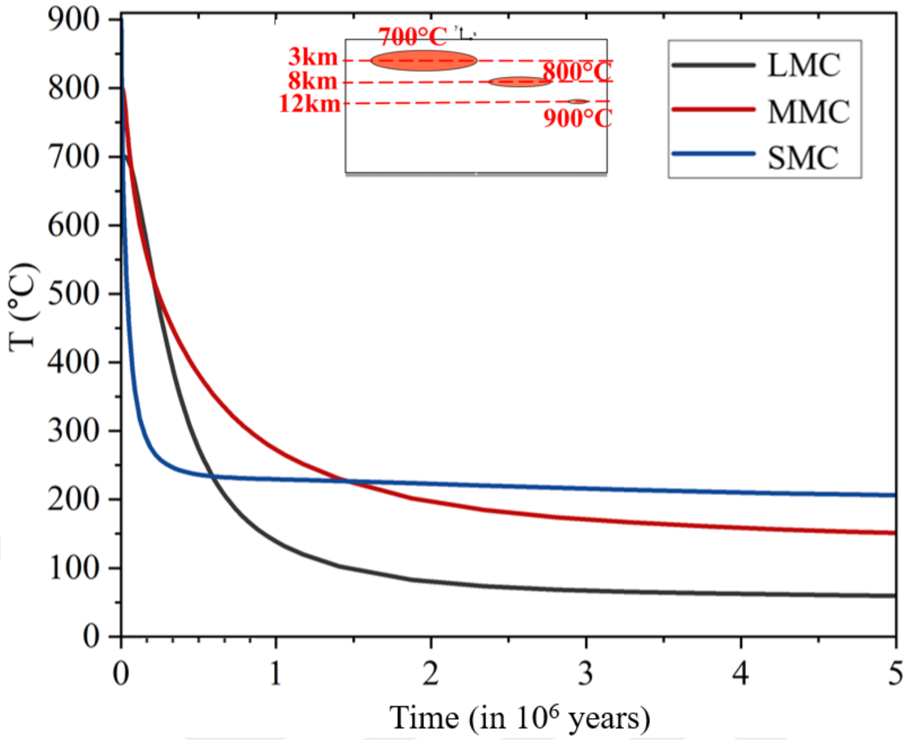

Figure 3.17. Temperature profile - D_3-8-12, T_7-8-9 (2D)

As anticipated, when all magma chambers are located in the deepest coordinate like in case D_12-12-12,T_9-9-9, the elevated host rock temperatures at these depths result in extended cooling durations and a longer time to reach steady state such that the total time domain of 5 million years is not sufficient for this case to reach steady state. LMC, which has the largest volume of phase change material, takes upto 2.5 times longer to cool when it is at 12 km depth, compared to the cases it settles at 3 km. Whereas SMC, which has the smallest volume can cool rapidly even at 12 km depth the cooling rate difference is only 32%. In Case D_3-8-12, T_9-9-9, despite SMC being at the greatest depth and therefore in the hottest region, it is the first chamber to cool down. Throughout the entire time domain, the temperature profile reflects very simple heat transfer physics and the findings are consistent with prior predictions, with no unexpected variations. For a more detailed examination, the total time required for complete solidification is provided for each of the three studied magma chambers.

Table 3.1. Solidification times (years) in 2D model

2D	LMC	MMC	SMC
D_3-3-3, T_7-7-7	169403	84027	8955
D_3-3-3, T_8-8-8	233076	126221	14094
D_3-3-3, T_9-9-9	285541	162048	19405
D_8-8-8, T_7-7-7	249806	87771	9587
D_8-8-8, T_8-8-8	417342	147425	15869
D_12-12-12, T_9-9-9	670920	242907	25694
D_3-3-3, T_7-8-9	166120	126289	19414
D_8-8-8, T_7-8-9	258631	156931	23961
D_3-8-12, T_7-7-7	166395	87379	10893
D_3-8-12, T_9-9-9	286508	208050	25732
D_12-8-3, T_9-9-9	671258	208879	18584
D_3-8-12, T_7-8-9	166123	148027	25192

Upon examining Table 3.1, varying cooling rates and patterns are obtained based on different size, depth and initial temperature values of magma chambers. The first noticeable aspect is that all magma chambers solidifies before one million year time period even at the greatest depth and temperature. It is because all chambers are surrounded by host rock having temperature lower than the phase change temperature, enabling the steady state to be completely solid material. Even when at deepest coordinate and with highest initial temperature value, case D_3-8-12, T_7-8-9, SMC solidifes earlier than the others. Since it is the smallest volume that will undergo a phase change this rapid cooling is an expected output. When all chambers are at the same depth, SMC solidifies around 10 times earlies than MMC and 15 to 20 times earlier than LMC. Those ratios decrease to 5.5 and 6.6 when SMC is at 12 km, surrounded by high temperature host rock domain and have greater initial temperature than the other chambers.

Meanwhile, cooling profile of LMC is mainly controlled by depth. When LMC is at the greatest depth, the effect of depth on its solidification time is much more significant compared to the changes in cooling rate ratios of the other chambers. For instance, in the comparison between the D_3-3-3, T_7-7-7 case and the D_8-8-8, T_7-7-7 case, the solidification time of LMC shows 48% increase where this value is 5% and 7% for other chambers. This is due to the fact that, in LMC, the ratio of the heat transfer interface to the liquid material is lower compared to the other chambers. LMC, the largest phase change body, always solidifes significantly later than others but solidifies rapidly if it is located close to the Earth's surface. The underlying cause of this is the thermal gradient present in the host rock domain. Cooling at the deep regions occurs slowly due to the high temperature of the surrounding area caused by increasing temperature gradient.

On the other hand, increase in the magma initial temperature influences the solidification time; however, this effect is linear and does not exhibit the same ratios as those observed with changes in depth. For example, at the same depth, a one-unit increase in temperature results in a corresponding one-unit increase in cooling time. It occurs because the host rock maintains similar properties at the same depth, while as depth increases, factors such as heat transfer coefficient and thermal conductivity change, leading to more complex effects on the cooling rate. To sum up, change in initial magma temperature delays the total solidification time but does not strongly affects it. Therefore, depth of magma chambers is the dominating decision making parameter rather than the magma internal temperature. Thus far, the comments have pertained to the 2D simulations; for the sake of comparison, Figures 3.18-3.29 and Table 3.2 includes interpretations of the 3D model as well.

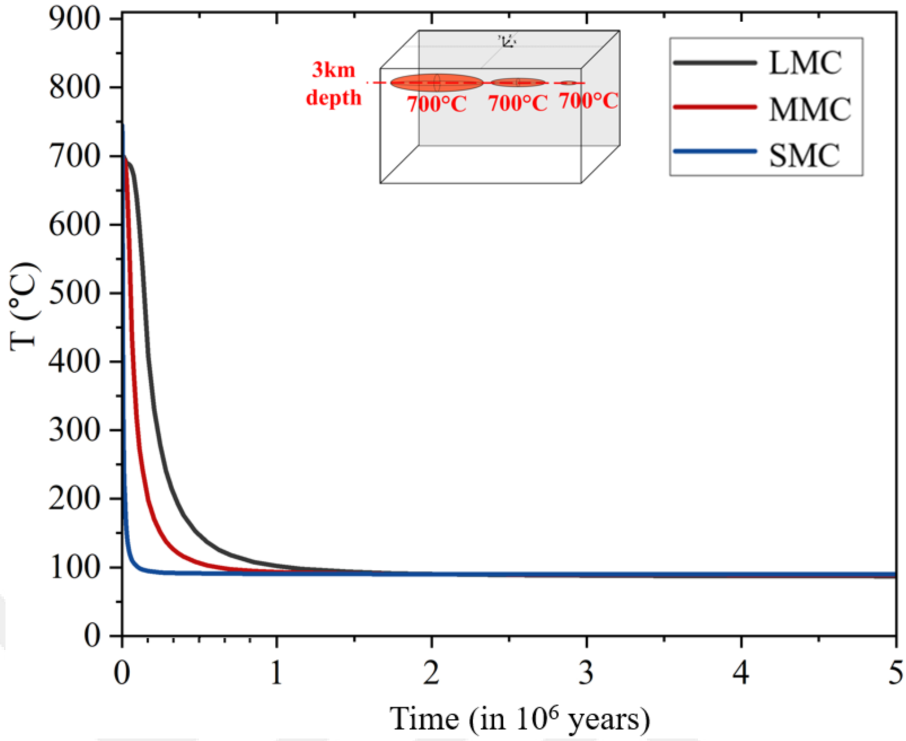

Figure 3.18. Temperature profile - D_3-3-3, T_7-7-7 (3D)

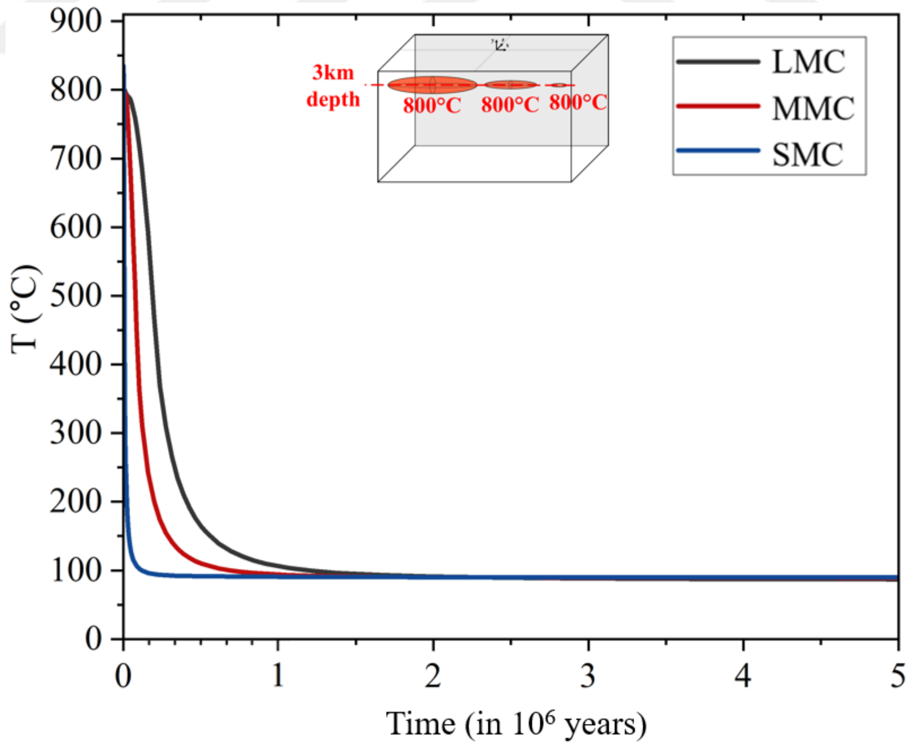

Figure 3.19. Temperature profile - D_3-3-3, T_8-8-8 (3D)

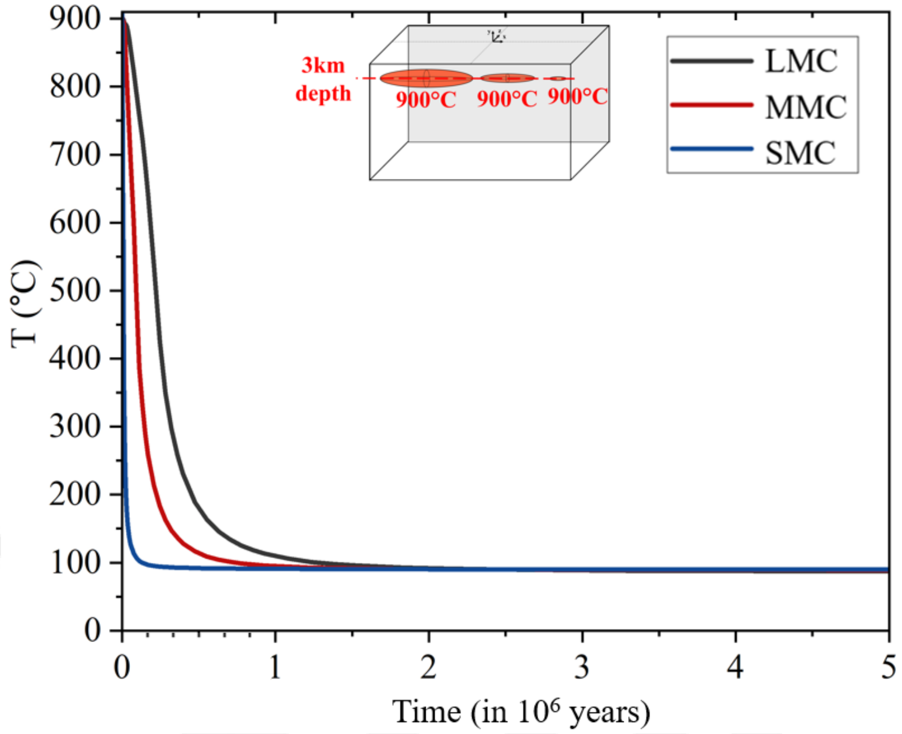

Figure 3.20. Temperature profile - D_3-3-3, T_9-9-9 (3D)

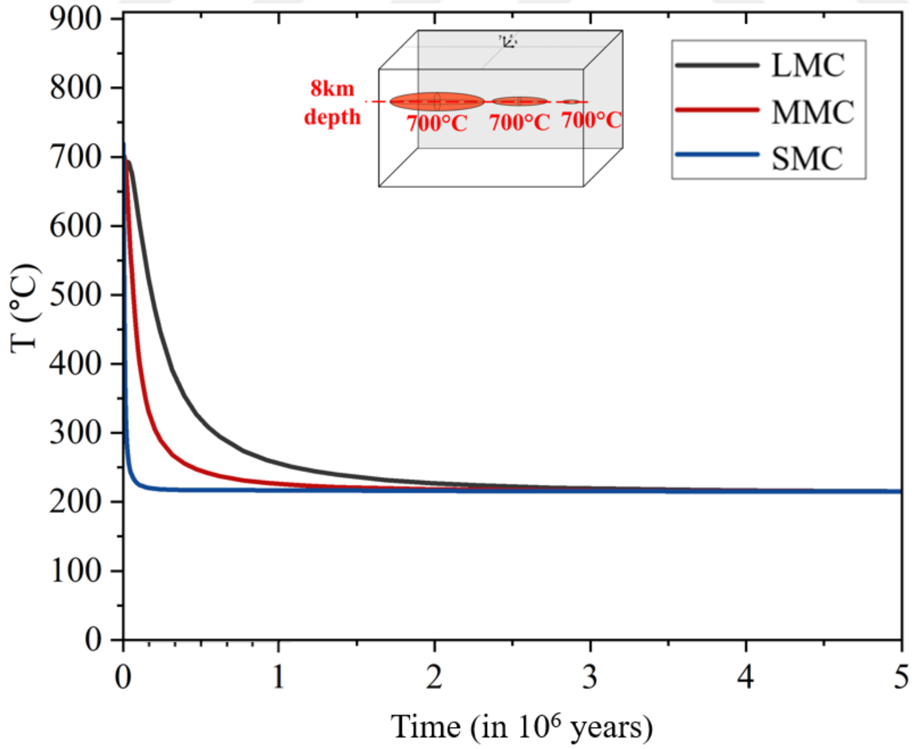

Figure 3.21. Temperature profile - D_8-8-8, T_7-7-7 (3D)

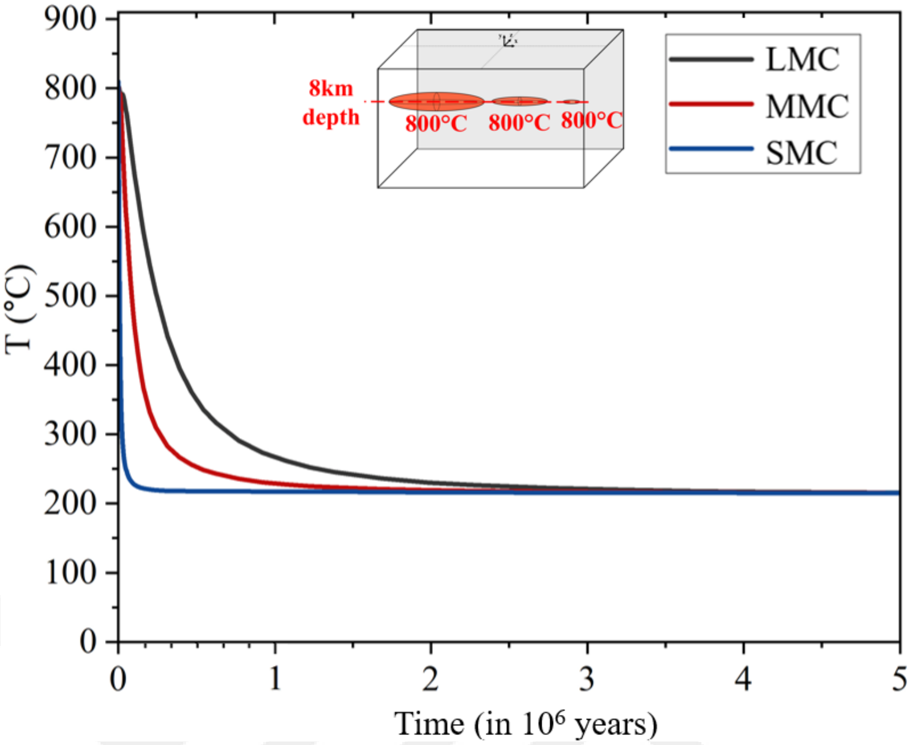

Figure 3.22. Temperature profile - D_8-8-8, T_8-8-8 (3D)

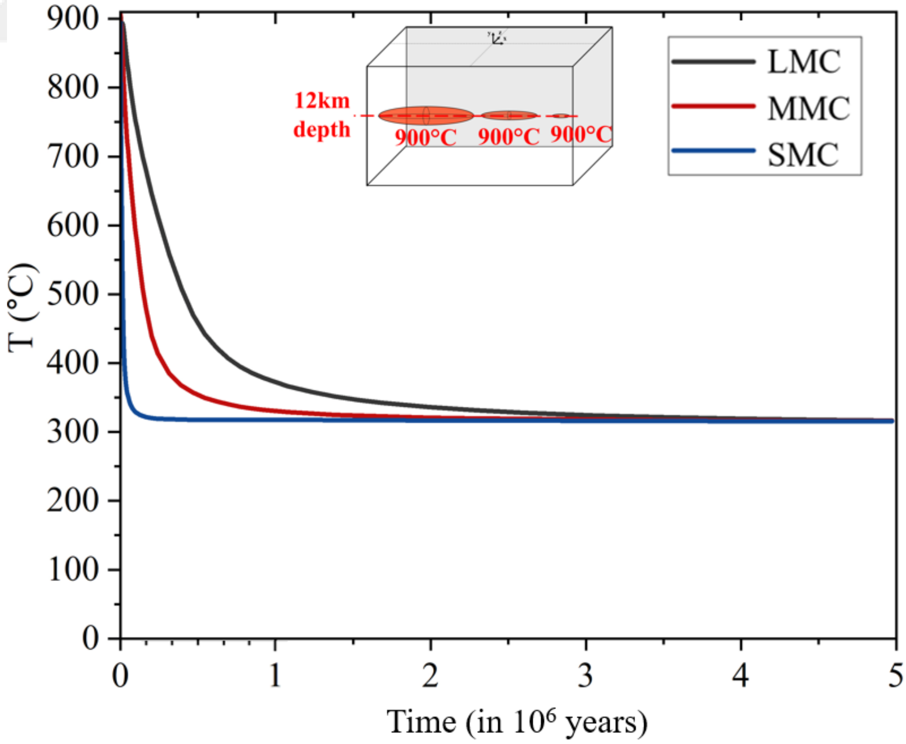

Figure 3.23. Temperature profile - D_12-12-12, T_9-9-9 (3D)

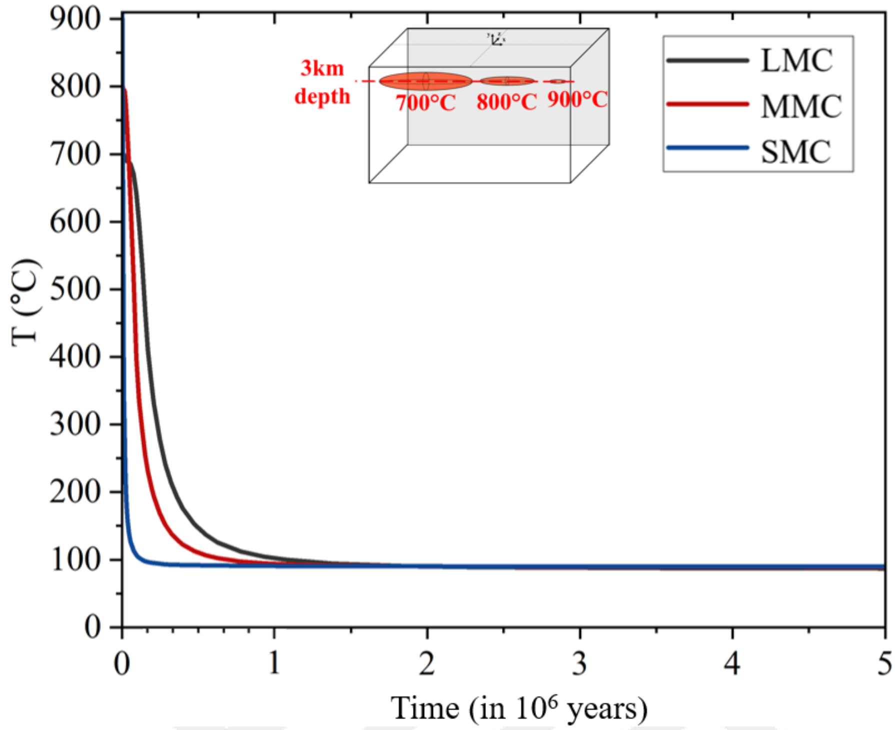

Figure 3.24. Temperature profile - D_3-3-3, T_7-8-9 (3D)

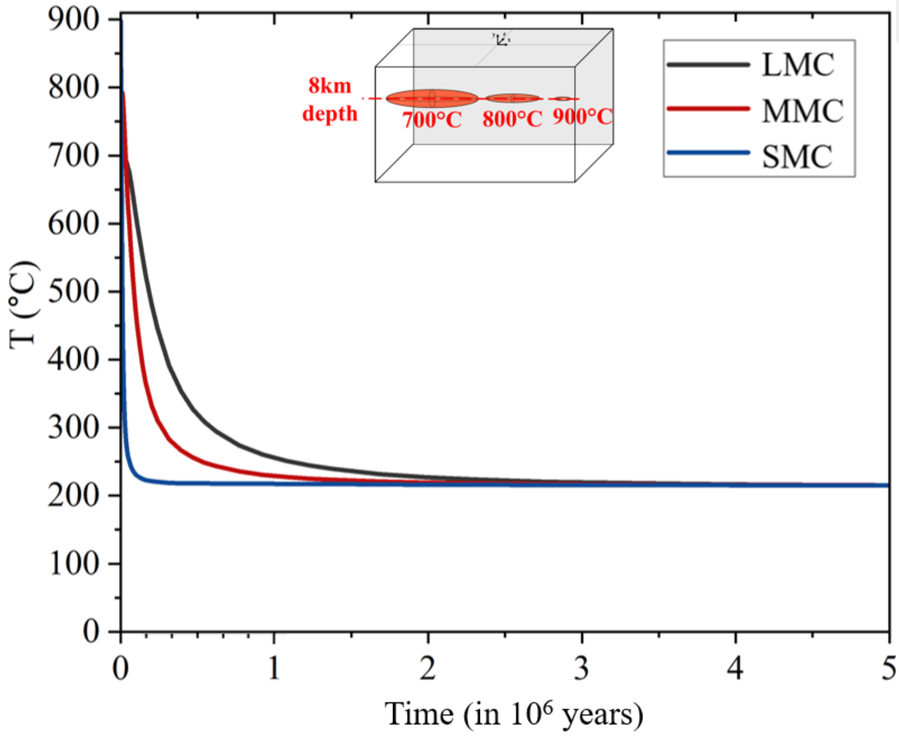

Figure 3.25. Temperature profile - D_8-8-8, T_7-8-9 (3D)

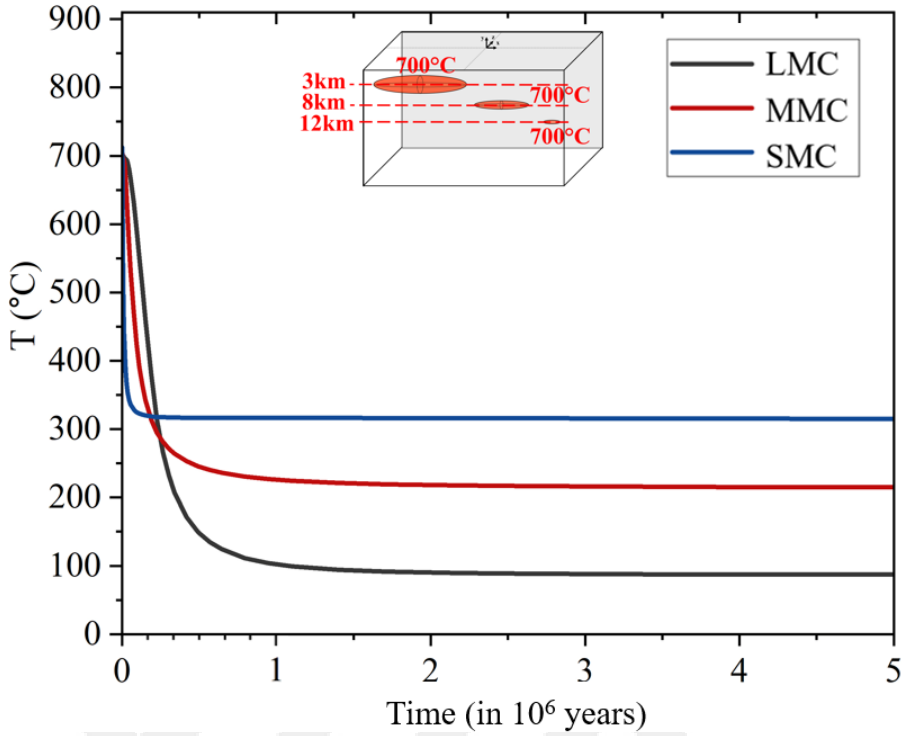

Figure 3.26. Temperature profile - D_3-8-12, T_7-7-7 (3D)

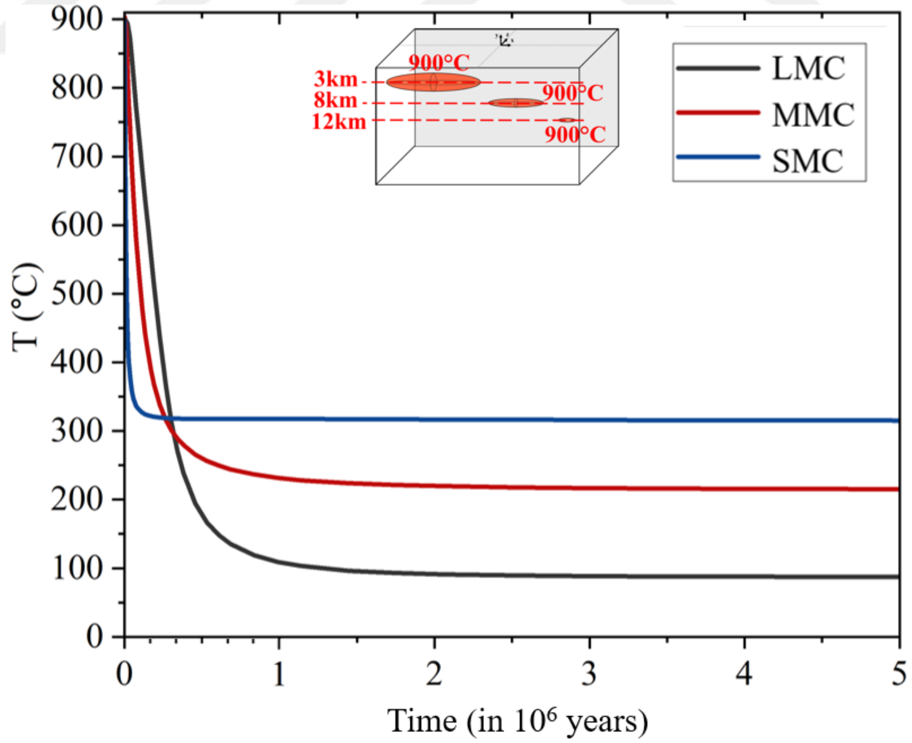

Figure 3.27. Temperature profile - D_3-8-12, T_9-9-9 (3D)

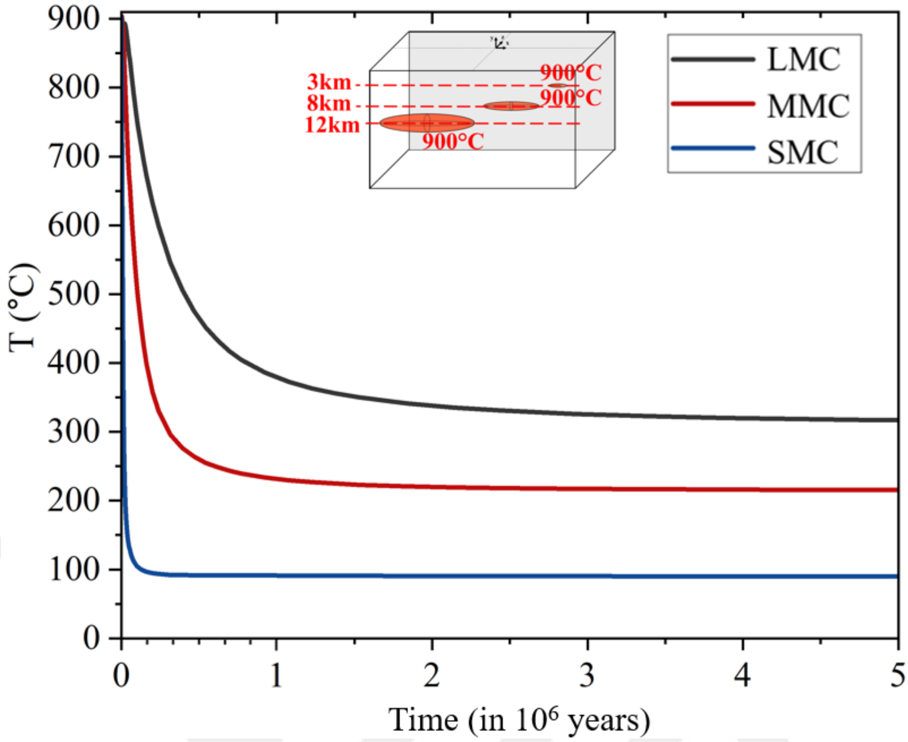

Figure 3.28. Temperature profile - D_12-8-3, T_9-9-9 (3D)

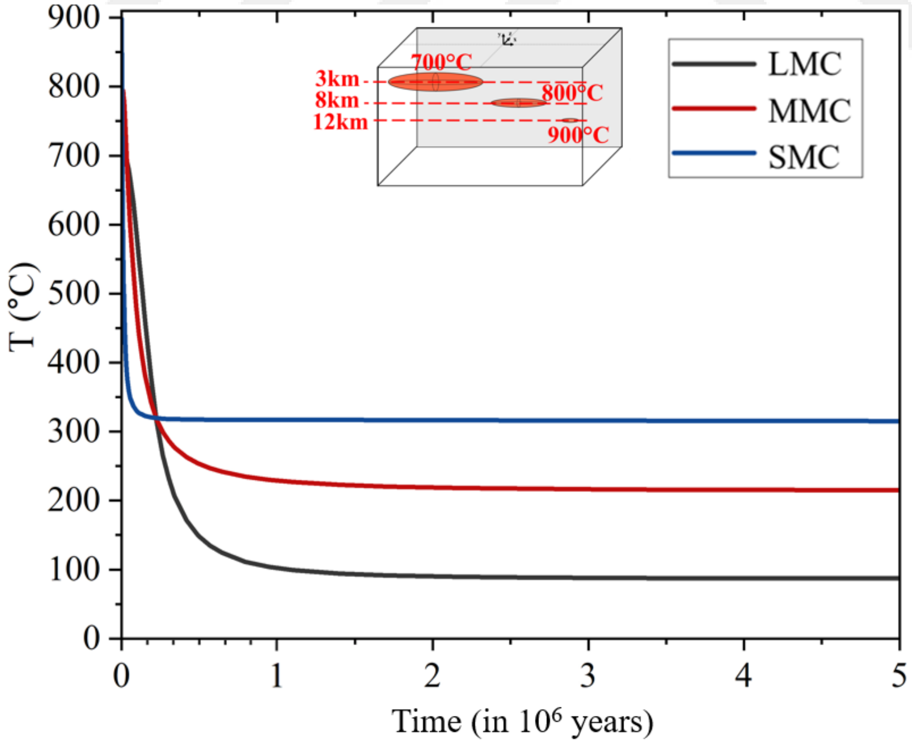

Figure 3.29. Temperature profile - D_3-8-12, T_7-8-9 (3D)

In all cases of the 2D and 3D simulations, the overall temperature patterns behave similarly but up to 3 times faster cooling occurs in the 3D model. The underlying cause of this is in 3D models, there is dimensioning in an additional geometry axis, enabling to assign a more rounded and compact geometric shape. This leads to greater conduction interface allowing heat to dissipate more rapidly. Additionally, heat transfer is more efficient in 3D models because the heat can spread in all three dimensions, allowing for more rapid cooling compared to the 2D model, where heat transfer is confined to a single plane.

Table 3.2. Solidification times (years) in 3D model

3D	LMC	MMC	SMC
D_3-3-3, T_7-7-7	120297	46195	4604
D_3-3-3, T_8-8-8	166084	64209	6557
D_3-3-3, T_9-9-9	195208	80096	8067
D_8-8-8, T_7-7-7	125598	44928	4320
D_8-8-8, T_8-8-8	180364	62940	6608
D_12-12-12, T_9-9-9	294616	106989	10802
D_3-3-3, T_7-8-9	120141	65653	8060
D_8-8-8, T_7-8-9	145446	62869	7836
D_3-8-12, T_7-7-7	102682	44843	5293
D_3-8-12, T_9-9-9	162489	76566	9852
D_12-8-3, T_9-9-9	276923	78000	6603
D_3-8-12, T_7-8-9	102683	63489	9881

2D and 3D analyses show similar behaviors by means of solidification sequence but significantly different values regarding solidification time. In the 3D model, the time required for cooling is lower than in the 2D model, with a difference in magnitude ranging from 1.4 to 3. The average increase in cooling rates are 178% for LMC, 220% for MMC and 242% for SMC. Reduction in time is not completely parallel with the solidification pattern in 2D. For instance, increase in the solidification rate of SMC in the 3D modeling approach is greater than the other chambers such that it shows up to 305% increase where this value is a maximum of 227% for LMC and 271% for MMC. This is because of the increased conduction surface area in 3D configuration; the heat transfer interface shifts to the surface area of the ellipsoidal, rather than the upper and lower boundaries in 2D. This ratio affecting the heat transfer rate is tabulated for all chambers and cases in Table 3.3. Calculations are held by assuming the unit thickness of the 2D domain as 1 km, which is the assigned value in the model.

Table 3.3. Surface area to volume ratio

	LMC (2D)	**MMC (2D)**	**SMC (2D)**	**LMC (3D)**	**MMC (3D)**	**SMC (3D)**
SA:V	0.53	0.88	2.68	1.05	0.96	4.77

MMC has a flatter shape in the xy plane, which allows its 2D and 3D SA:V's to be similar. In straightforward cases like D_3-3-3, T_9-9-9, the deviation between 2D and 3D analyses is in the order of magnitude of 1.5, 2.2 and 3 times for LMC, 2 and 3 respectively. SMC is the most deviated in all cases due to its high SA:V. Although the heat transfer interface of LMC increases with the addition of the third dimension in the 3D model, leading to a fivefold increase in its SA:V, the amount of phase change material remains the dominant factor for solidification. Therefore, the ratio between 2D and 3D is more significant in smaller magma chambers. However, as the cooling time for LMC is high, even when the ratio between 3D and 2D is small, the deviation becomes significant at the order of magnitude of 45 years minimum.

3.2.2 Stress Distributions

The von Mises stress data are collected from midlines of the chambers for years 60, $1.6x10^4$, $16x10^4$, $32x10^4$, $5x10^5$ and $5x10^6$. The reason for selecting these time steps is to analyze the stress variations and their effects during the following four conditions: at directly after initial time (60th year), while heat transfer occurs at a certain level and phase change is ongoing (1.6x10^{4th} and 1.6x10^{5th} year); when the phase change is completed but heat transfer is still occurring (1.6x10^{5th}, 32x10^{4th} and 5x10^{5th} year) and when heat transfer has ceased and steady state has been reached (5x10^{6th} year). Graphs are drawn for all cases in 2D and 3D.

In real-world circumstances, the type of stress to be analyzed is determined by the specific characteristics of the field under study. As outlined in Section 1, if the external loading conditions indicate that shear stress leads to fractures, von Mises stress should be the subject of the analysis. Conversely, if fractures are induced by tensile loads resulting in cracks, the maximum tensile principal stress should be analyzed. In this study, a shear stress-dominated field was assumed, therefore, von Mises stress results, which effectively represent shear stress in geological contexts, were computed and evaluated.

The temperature results were analyzed in two subgroups: 2D and 3D, as both simulations applied simple heat transfer physics, making them consistent within themselves but yielding different outcomes between the two. This time, a case-by-case comparison is made between the 2D and 3D results, as the solid mechanics outcomes are temperature-induced and too complex to interpret collectively. To obtain stresses defined as midline stresses, horizontal midlines passing through the center of each chamber are created in the xy plane. The von Mises data is then taken along these lines (i.e., along the x-coordinate). Before presenting the stress graphs, visual results for case D_3-3-3, T_7-7-7 obtained from both 2D and 3D models are provided in Figure 3.30-3.33 to facilitate easier interpretation of the general stress distribution graphs and to provide an example of study findings.

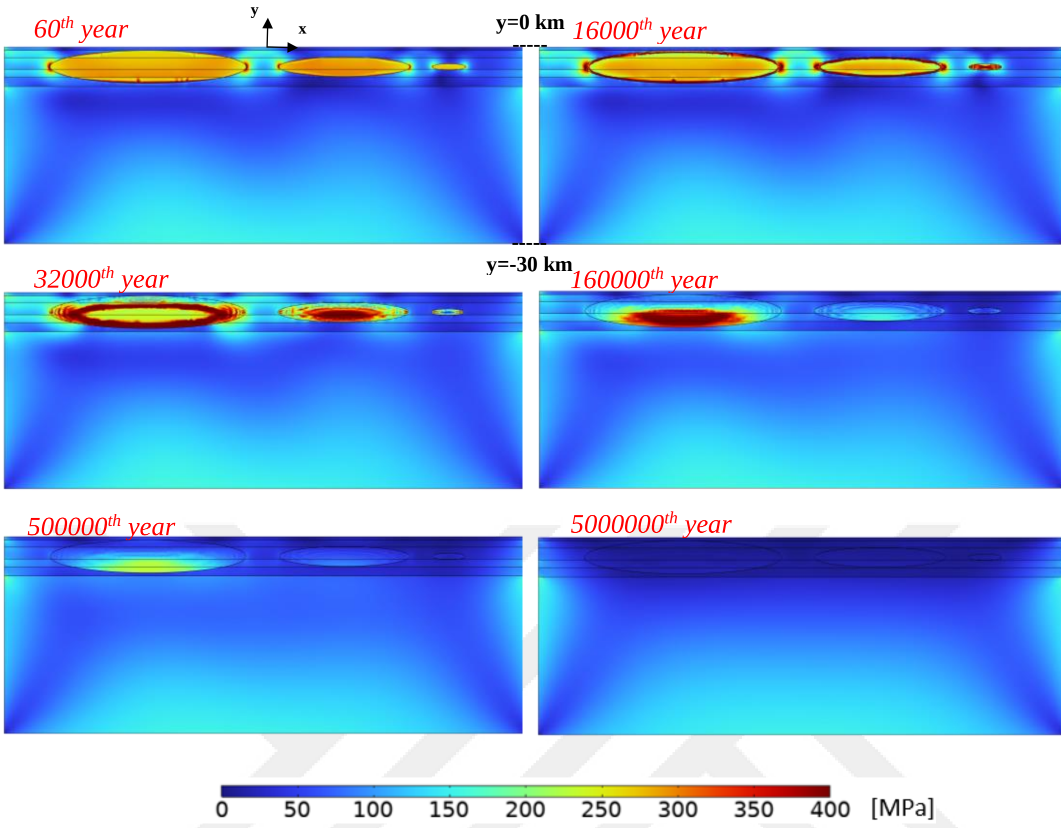

Figure 3.30. Stress distributions - D_3-3-3, T_8-8-8 (2D)

As observed in Figure 3.30 and 3.31, highest stress concentrations appear around the fluid region. As magma solidifies and the solid-fluid interface moves towards the center of the magma chamber, stresses continue to surround the liquid region. The reason of high stresses being observed around the liquid region is the thermal gradient which induces expansion that differs between the host rock and the magma.

Host rock layers with larger Young's modulus are subjected to higher stress than the less stiff ones. This distribution can be clearly seen from the difference between the layers. For instance, the deepest host rock layer exhibits higher stress concentrations due to its greater stiffness, which leads to a higher resistance to strain under applied loads. This mechanical contrast results in uneven stress distribution, with stiffer layers absorbing more stress compared to less stiff ones. As the side domains are fixed, even at steady state, stress concentrates at those regions. Because the upper surface is free, no stresses appear there at steady state.

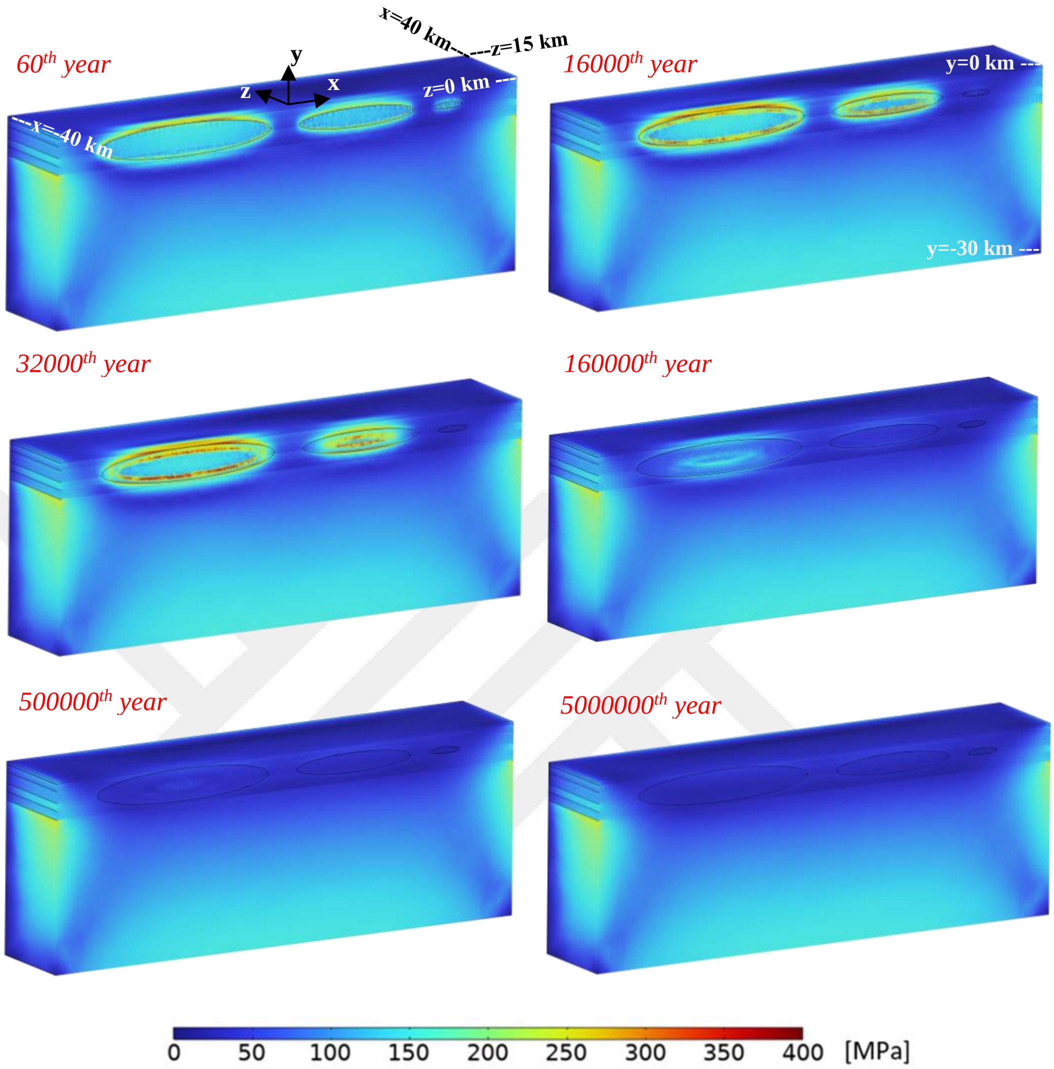

Figure 3.31. Stress distributions in x-y plane - D_3-3-3, T_8-8-8 (3D)

Stress concentration in the order of magnitude of 400MPa occurs at the phase change interface, with both magnitude and concentration being higher in the 2D model. This could be due to the reduced geometric complexity in 2D, which amplifies stress accumulation by neglecting out-of-plane stress redistribution. Once solidification is complete and only solid-solid heat transfer occurs, stress values decrease, though a clear pattern remains, indicating regions with temperature gradients. Upon reaching a steady state, stress levels further decrease, and no additional stress induced by the magma is observed. Distribution from the y-z plane is also given to investigate the effect of magma chambers on Earth's surface.

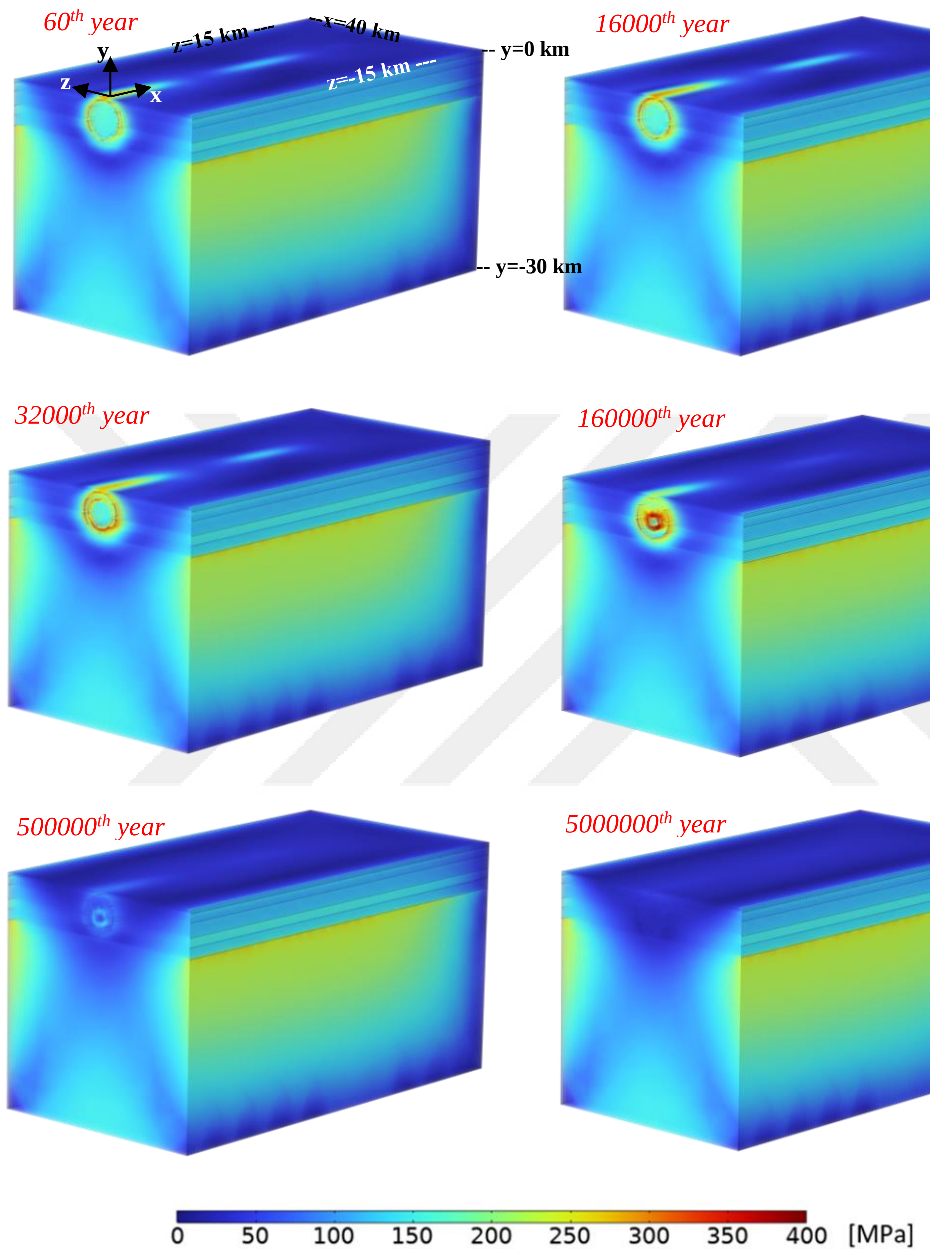

Figure 3.32. Stress distributions in y-z plane - D_3-3-3, T_8-8-8 (3D)

As observed in the distribution on the y-z plane, magma chambers located at a depth of 3 km exert a significant stress effect on the surface. The maximum obtained von Mises stress value is at the projection of LMC, with a magnitude of 300 MPa. This value is 4 to 5 times high relative to real-world conditions, where the likelihood of such a large magma chamber being located so close to the surface is very low. While the calculated stress values are generally much higher than those expected in real scenarios, it is apparent that magma chambers influence surface stresses. Distribution from the x-z plane is also given in Figure 3.33 as a top view to comment on the stress distribution on lateral section.

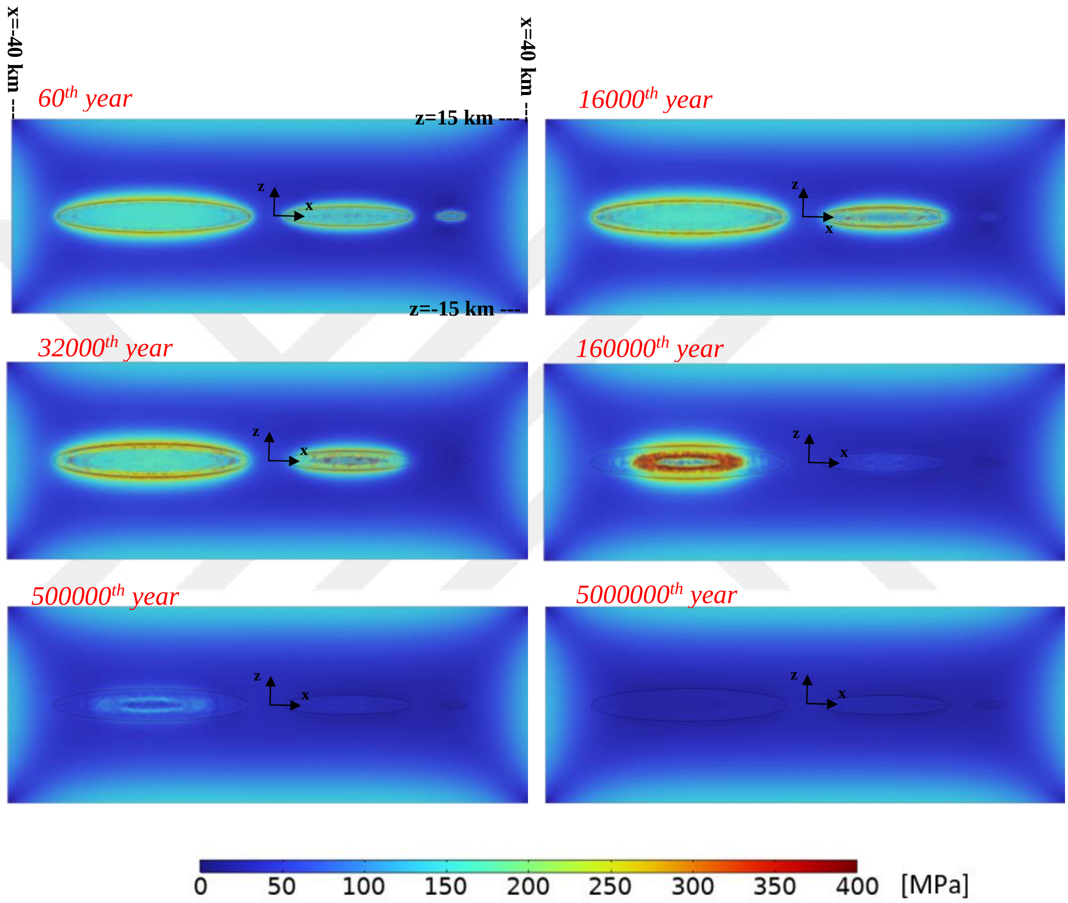

Figure 3.33. Stress distributions in x-z plane - D_3-3-3, T_8-8-8 (3D)

The cross-sectional images on the x-z plane clearly illustrate how stress intensity becomes concentrated at the interface between the remaining magma and the host rock as solidification progresses. Additionally, an examination of the sections reveals stress concentrations in regions that began crystallizing earlier. In light of this information, the subsequent stress distribution graphs are analyzed.

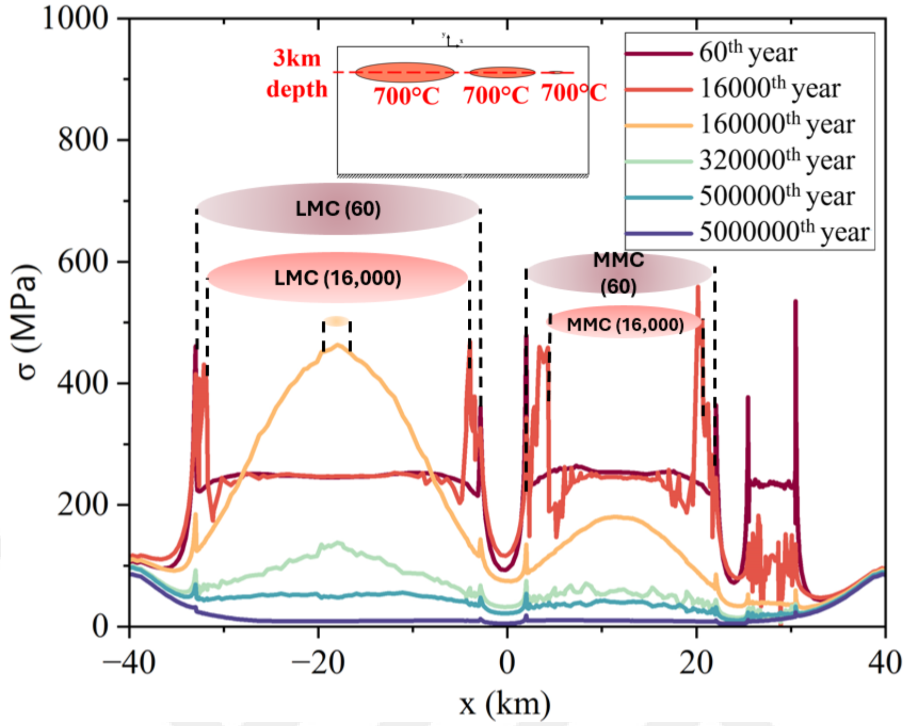

Figure 3.34. Von mises stress on midline (-3 km) - D_3-3-3, T_7-7-7 (2D)

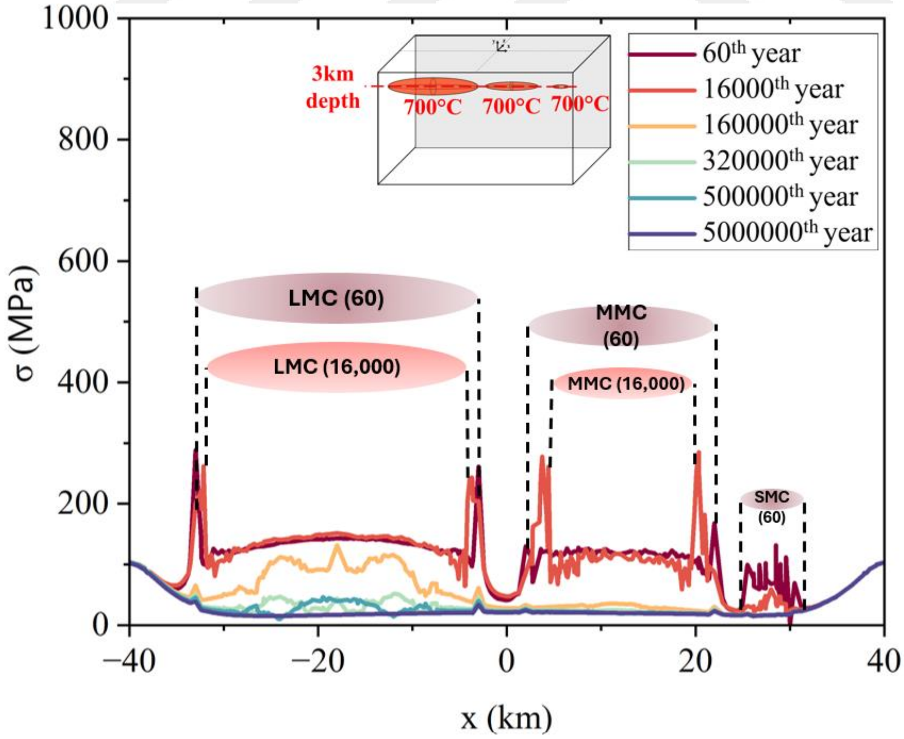

Figure 3.35. Von mises stress on midline (-3 km) - D_3-3-3, T_7-7-7 (3D)

In Figure 3.34-3.35, unsolidified portion of magma for LMC at related year is illustrated by ellipsoidal visuals in order to clarify the explanations. The first noticeable feature is that, at each stage, the stresses in the 3D model are lower with an average of 33% compared to those in the 2D model. Reason of this is the stresses distributed over a larger area in 3D model. In the 2D model, the stresses around the magma chamber are concentrated in a specific plane, leading to sharper, localized stresses. However, in the 3D model, stresses are spread out in three dimensions, which results in a more homogeneous distribution of stress.

When thermal effects on stress distributions are considered, as also indicated in the previous section, temperature change occurs more rapidly in the 3D model resulting in faster and more homogeneous heat distribution, which reduces temperature gradients. Lower temperature differences lead to lower thermal stresses, as thermal expansion-induced stresses are lower when temperature differences are smaller.

Magnitudes and patterns of stresses around LMC and MMC are similar in 60^{th} year and 16000^{th} year because they are both times of early phases of heat transfer. Early phase stresses are high as a result of the great temperature gradient presence between magma and host rock domain. For SMC, at 60^{th} and 16000^{th} year, there are significant differences between 2D and 3D graphs where the patterns for LMC and MMC remains similar. The reason for this is that SMC's solidification is complete in both the 2D and 3D models, but in the 2D case, solidification takes longer, leading to continued intense heat transfer and consequently higher stresses at 16000^{th} year. In contrast, in the 3D model, solidification is completed much earlier, resulting in reduced thermal gradients and stabilized heat flow, leading to lower thermal effects at that time step. At 16000^{th} year, stresses inside LMC of the 2D model reach their highest values, 450MPa on the graph. This is due to most part of the magma being already solidified, while phase change is still occurring in the central region until 169403^{th} year. The high thermal gradient in this area causes significant expansion, resulting in intense stress. The reason we do not observe this in the 3D model during the same time period is that solidification has already been completed, cooling has progressed, and thermal gradients have decreased. In the last two time steps, stresses drop to their lowest values as the system approaches steady state, with thermal effects having diminished significantly.

Especially for MMC and SMC, there are abnormal fluctuations at earlier time domains. These may be due to the combined effect of phase change and heat transfer, leading to a more complex, crystal material behavior in this region and time. Other than the erratic trend caused by material inconsistency, to get rid of the unstable profiles, mesh refinements in magma domain can be made by equating one element size to a typical crystal size. As this size is in the order of magnitude of micrometers, this will lead to huge number of mesh elements and a high computational cost.

Stress values exceed 50MPa, which is a typical host rock ultimate strength, both in 2D and 3D inside and at the boundary of the chambers. As stresses of such magnitudes are too high, whether the thermal expansion effects of those chambers are too effective, or a viscoelastic buffer region for the interface between magma and host rock should be considered to be added to the model to act as a damping region.

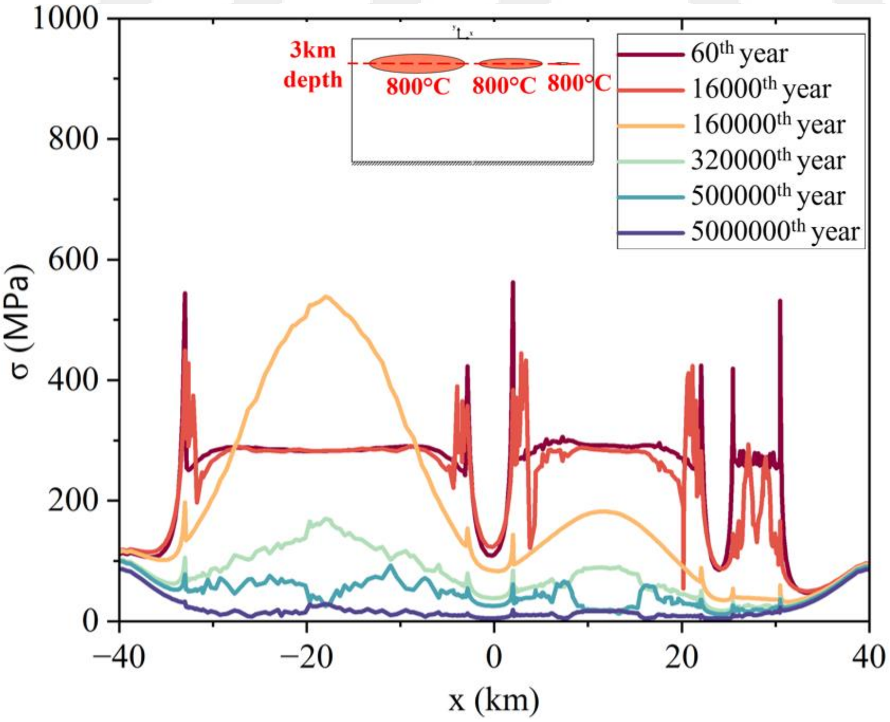

Figure 3.36. Von mises stress on midline (-3 km) - D_3-3-3, T_8-8-8 (2D)

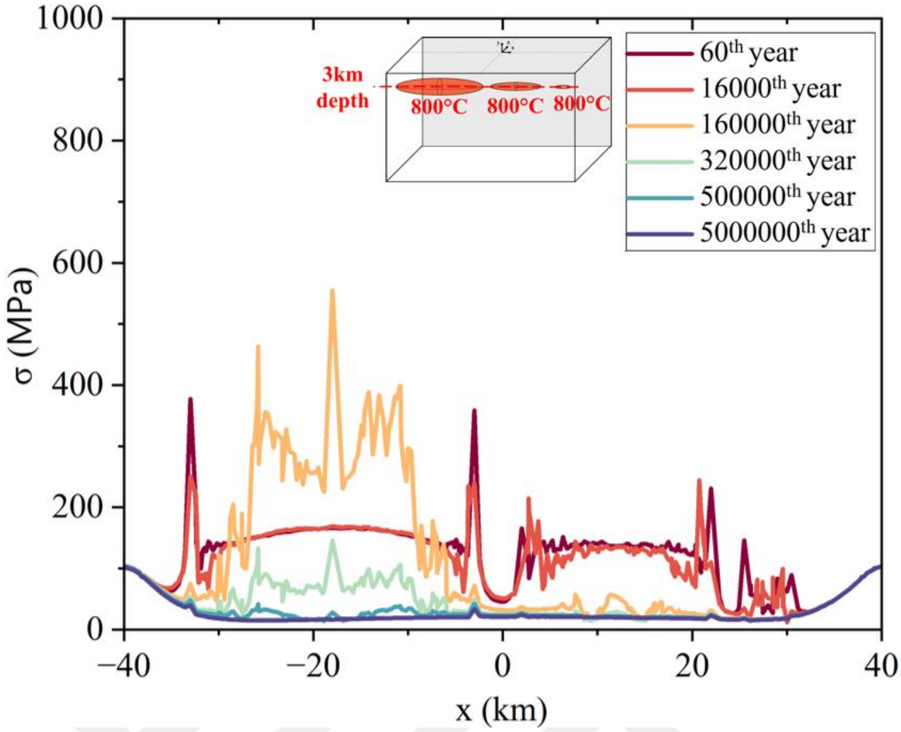

Figure 3.37. Von mises stress on midline (-3 km) - D_3-3-3, T_8-8-8 (3D)

When the analysis is conducted for the same configuration with a magma initial temperature of 800°C, a very similar pattern emerges in 2D, but with higher stress values and lagged profile. The formation of higher stresses is due to the increased thermal expansion caused by a higher temperature gradient and the delay after the early phase is because of later solidification times. In 3D graph, there are abnormal fluctuations inside the magma chamber at year 160000 caused by the ongoing crystallization process at this time period. As observed in the previous configuration, D_3-3-3; T_7-7-7 given in Figure 3.34-3.35, the highest stresses are found in LMC during the phase change process. The rise in stresses observed in the 3D model at the 160000th year is attributed to a delayed solidification process, which occurs later than in the previous case, due to the increase in the initial magma temperature.

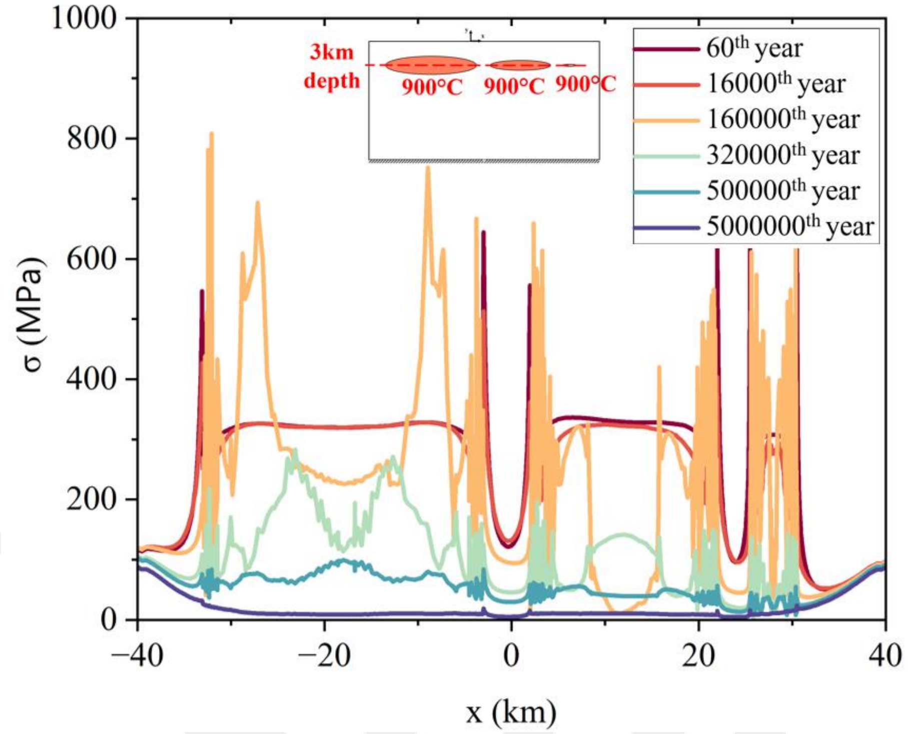

Figure 3.38. Von mises stress on midline (-3 km) - D_3-3-3, T_9-9-9 (2D)

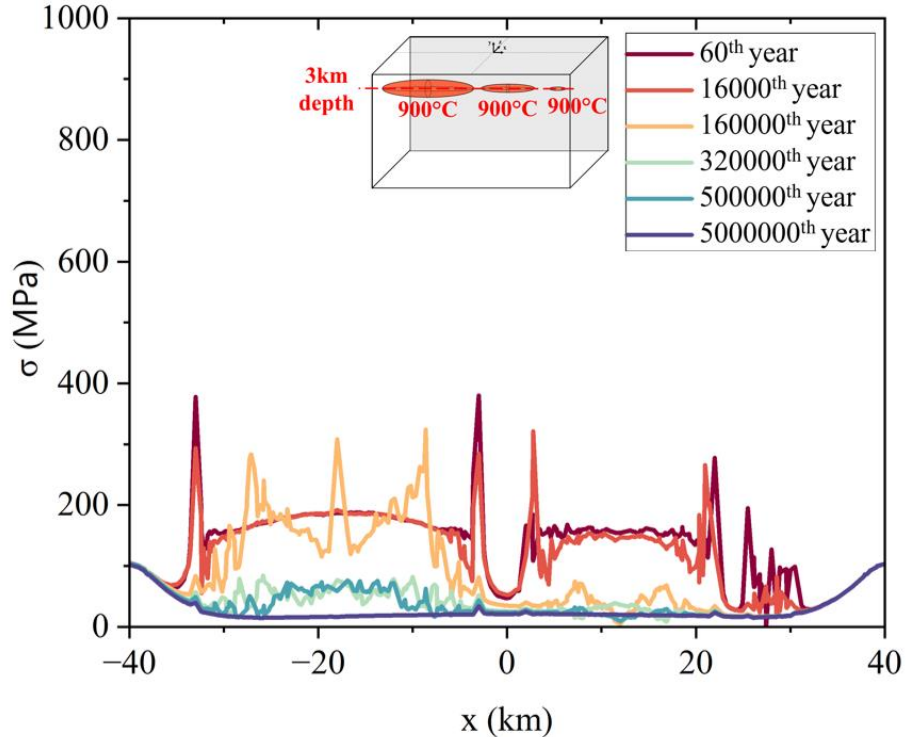

Figure 3.39. Von mises stress on midline (-3 km) - D_3-3-3, T_9-9-9 (3D)

When the initial magma temperature is set to the highest value of 900°C, the overall stresses increase up to 15% when compared to the case D-3-3-3, T_7-7-7 having lower temperature. This increase in the overall stresses highlights the effect of temperature on the stress distributions. As anticipated, the solidification time of LMC is significantly delayed because of the increase in cooling time. Consequently, the high stresses that are previously observed at the center of the magma chamber during phase change in previous cases are not yet present by the 160000^{th} year in case D_3-3-3,T_7-7-7. Instead, as expected based on literature, the presence of magma causes stresses to be observed at the chamber's shallow tail regions.

In the previous cases, the lower stresses observed in the 2D model at the 320000^{th} year are due to the ongoing solidification process, which is still active at this time. However, due to the delayed solidification, these stresses are now higher. The delayed solidification effect in 2D leads to a delay in reaching steady state, which results in higher stresses at the midplane of LMC in the final time step. In contrast, in the 3D model, magma solidifies much earlier than in the 2D case and approaches thermal equilibrium, so all outputs after the 320000^{th} year are significantly lower than in the previous cases.

In the 2D model, during the early time domain, the stress distribution inside the magma chambers are concave, while in the 3D model, it increases toward the center, forming a dome like convex shape. This difference could be attributed to the fact that, in 3D, forces acting in the third coordinate are also considered and the expansion effects include contributions from these directions as well. This leads to higher stress concentrations at the center in the 3D model.

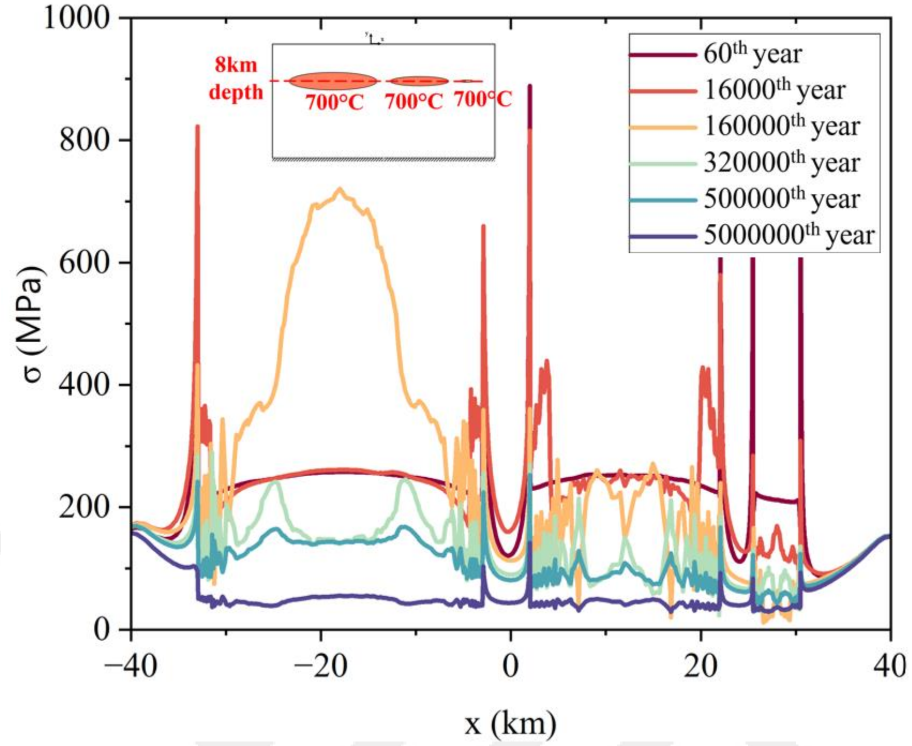

Figure 3.40. Von mises stress on midline (-8 km) - D_8-8-8, T_7-7-7 (2D)

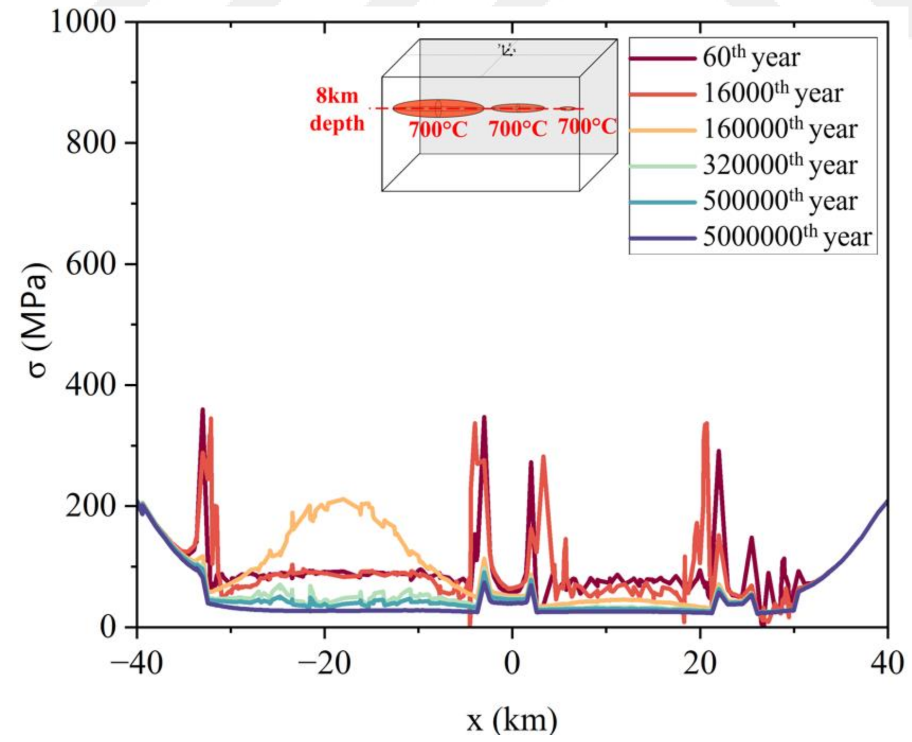

Figure 3.41. Von mises stress on midline (-8 km) - D_8-8-8, T_7-7-7 (3D)

In case D_8-8-8, T_7-7-7, since solidification and heat transfer occur at later time steps than the previous cases, we observe intense stresses in the 2D model up until the final time step. In contrast, in the 3D model, thermal equilibrium is reached much more quickly, so stresses in the last two time steps are lower, with high stresses only localized at the shallow tails as expected. The profile observed in LMC at the 160000th year in the 2D model, which is different from previous cases, is due to the stresses decreasing as the solidification process progresses from the outside in, with the chamber edges transitioning to host rock, where there is no temperature gradient. By the 360000th year, the stresses are fully concentrated at the temperature gradient boundaries. The 3D profile is very similar to the 2D profile of the D_3-3-3, T_7-7-7 case. This may be due to the solidification delay caused by the high temperature of the host rock at a depth of 8 km, which corresponds to the slow-progressing solidification process typically observed in the 2D model. Although the pattern is similar, the lower temperature difference in this case results in a smaller stress magnitude.

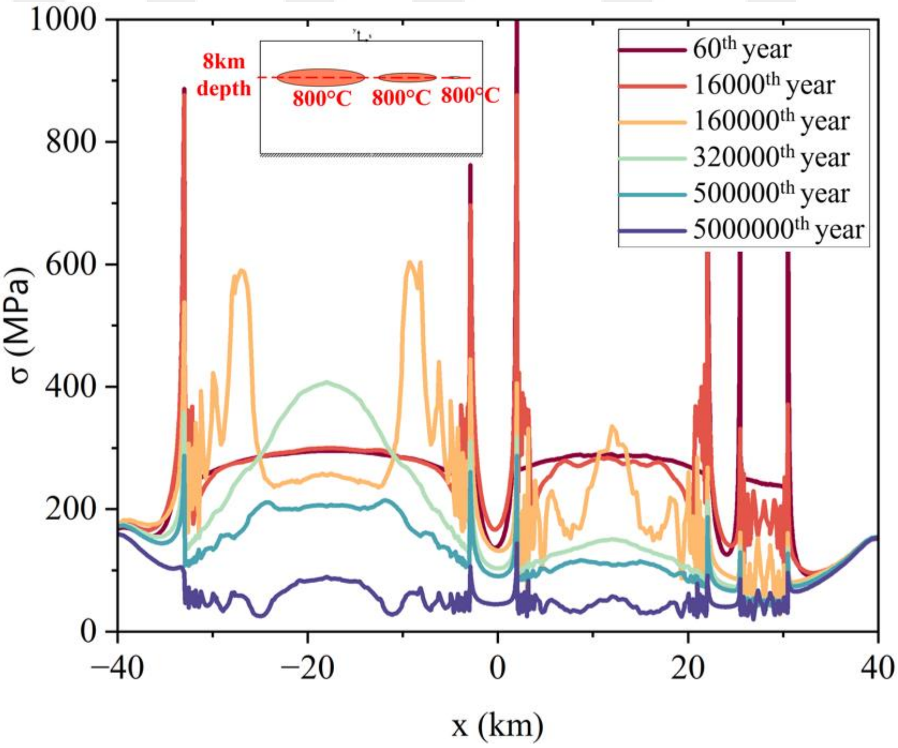

Figure 3.42. Von mises stress on midline (-8 km) - D_8-8-8, T_8-8-8 (2D)

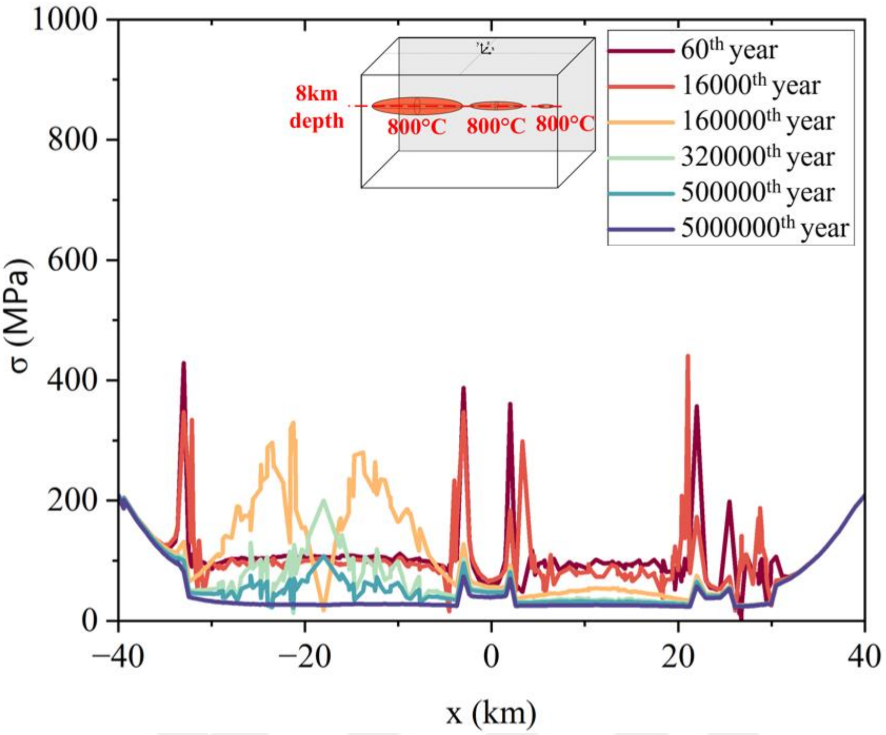

Figure 3.43. Von mises stress on midline (-8 km) - D_8-8-8, T_8-8-8 (3D)

The graph in Figure 3.42, with higher magma internal temperature, shows behavior that occurs earlier in the phase compared to the previous case (Figure 3.40-3.41). As solidification begins, the stress at the edges of the chamber moves from the region that has transitioned to host rock towards the new fluid area and the shallow tail. This is visible in the 2D graph at the 160000th year. Since thermal equilibrium is reached later, stresses decrease more slowly in the subsequent time steps. In the 2D model, while the other chambers approach equilibrium and show significantly reduced stresses, since solidification in LMC is not complete, the stresses at its midline remain high. The 3D and 2D graphs, however, show quite different behavior. The erratic trend is strongly observed in 3D for time domains and coordinates where crystallization occurs due to the complex, crystal material behavior. Especially in LMC, while crystallization is occurring, stress at the middle of the center drops abruptly in 160000^{th} year. Lower stresses are expected in the completely liquid regions of magma but this instant drop is considered as a model inconsistency as its value is the bottom value.

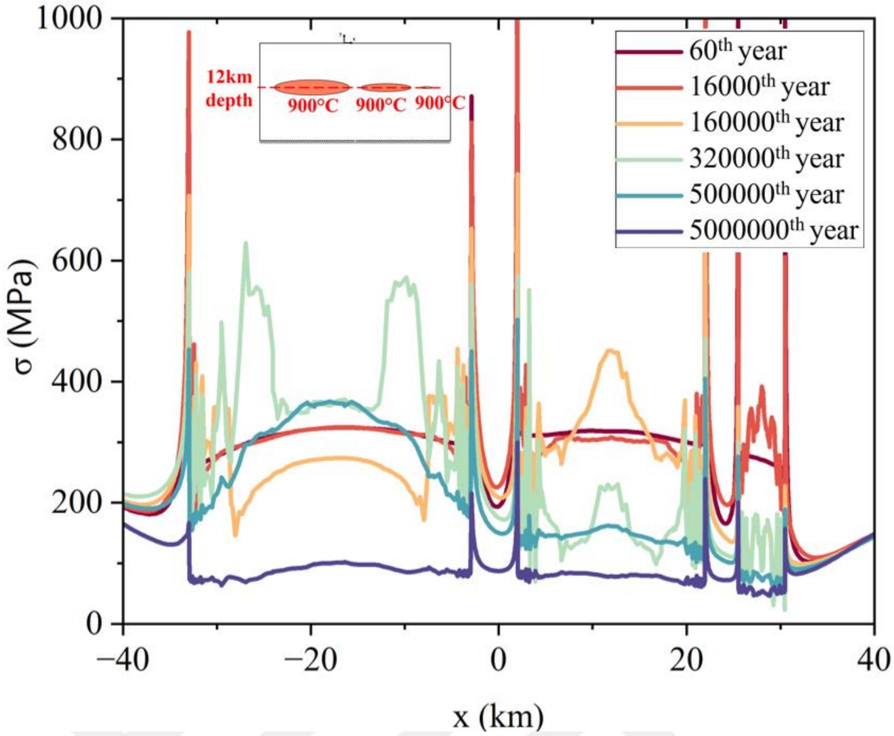

Figure 3.44. Von mises stress on midline (-12 km) - D_12-12-12, T_9-9-9 (2D)

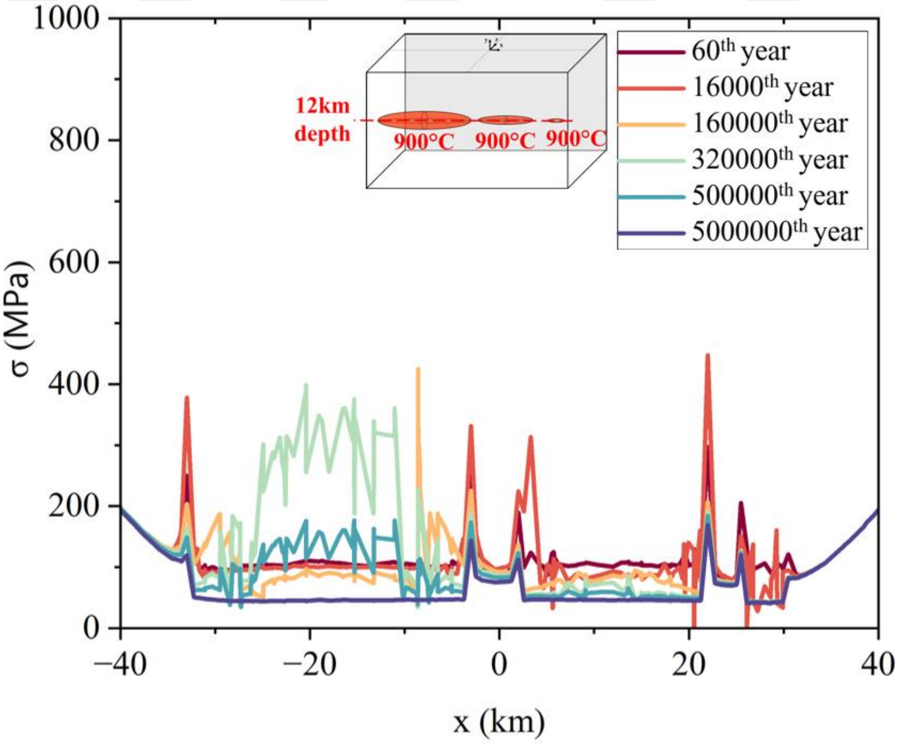

Figure 3.45. Von mises stress on midline (-12 km) - D_12-12-12, T_9-9-9 (3D)

In all cases, high localized stresses are observed at the shallow tail regions of the chambers in the early stages in 2D. This is a common behavior for all cases and can be interpreted not as a physical phenomenon, but rather as a discontinuity resulting from the abrupt material transition in the initial configuration. The presence of this is significant in the 2D domain but not in the 3D domain. It may be attributed to the point-wise transition observed in the 2D model. As in the previous results, stresses accumulate at the edges, moving from the chamber sides toward the center as solidification begins at the chamber walls. In all models, fluctuations due to material complexity are observed at the curved regions corresponding to the phase where LMC is in its crystalline material state. On the other hand, the abnormal anomalous fluctuations might be caused because of the insufficient number of mesh elements especially in 3D as the domain is too huge to divide elements smaller than meters.

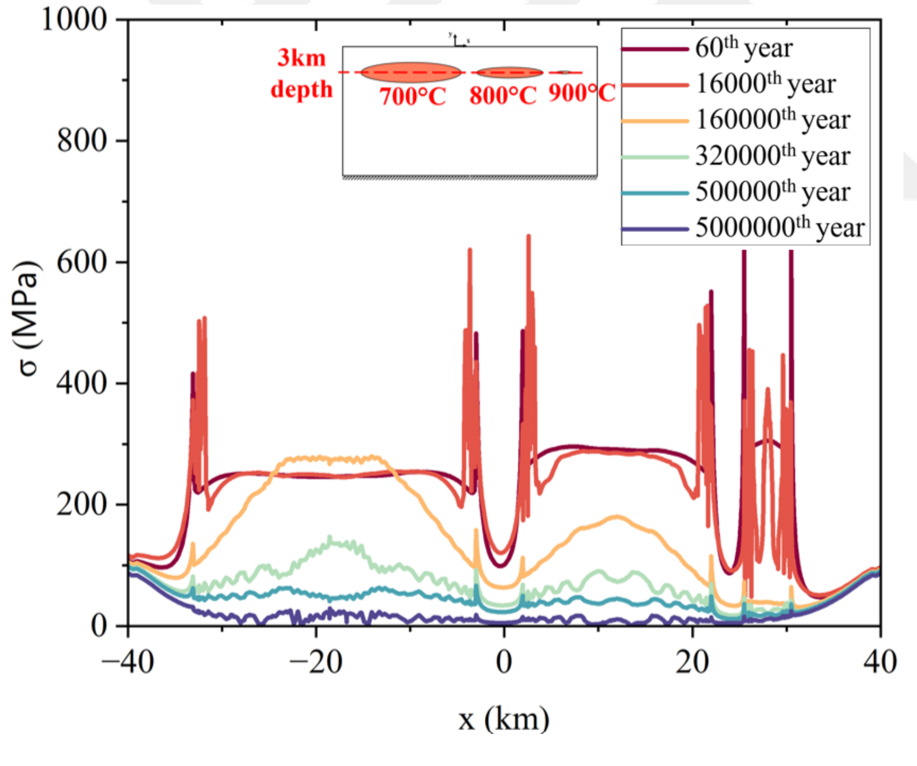

Figure 3.46. Von mises stress on midline (-3 km) - D_3-3-3, T_7-8-9 (2D)

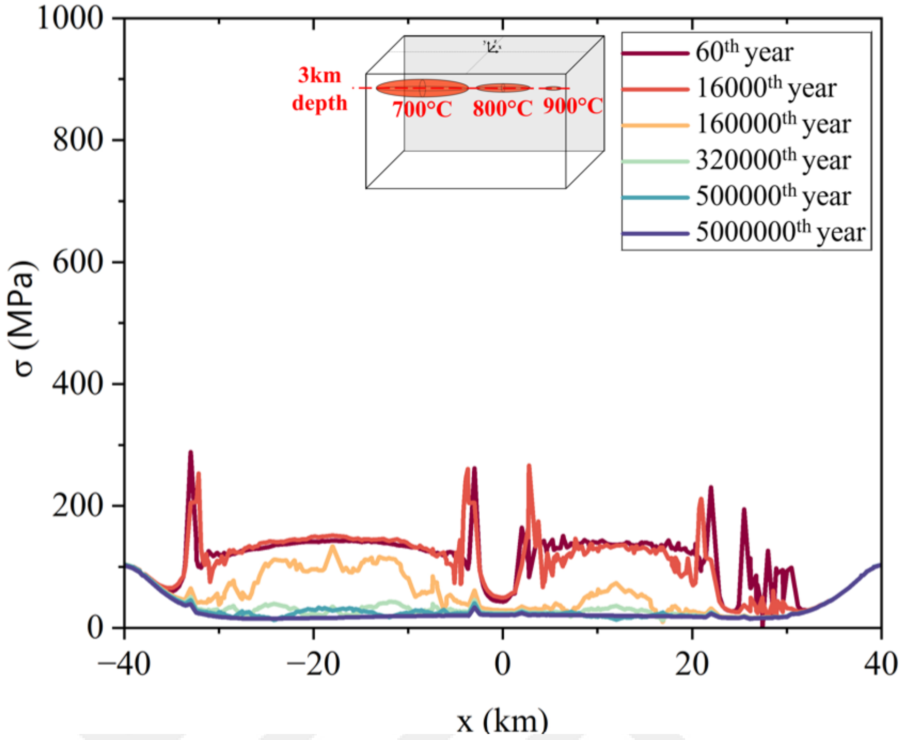

Figure 3.47. Von mises stress on midline (-3 km) - D_3-3-3, T_7-8-9 (3D)

Case D_3-3-3, T_7-8-9 exhibits very similar behavior to the cases at a depth of 3 km in the previous simulations. Since the solidification process of SMC is delayed because of the high initial magma temperature, and the 16000th year corresponding to a time when two phases are still present, the stress profile for SMC at this time step is both higher in magnitude and more fluctuated in 2D. Another difference is that, in the 2D model, LMC solidifies slightly later than in previous cases because more heat is transferred through the boundary of MMC where the higher temperature difference present; so the center of the chamber has not yet reached high stresses. As in the previous cases, the difference between the 2D and 3D models lies in the lower stress magnitudes observed in the 3D model, as well as the earlier occurrence of phase change stages in the 3D simulations. The small peak regions around the ellipsoidal geometry at steady state is because the newly generated rock material with the solidification of magma is not totally same with the parent melt as in real life conditions. A rock structure having the average E value of the surrounding host rock is assigned to magma after phase change.

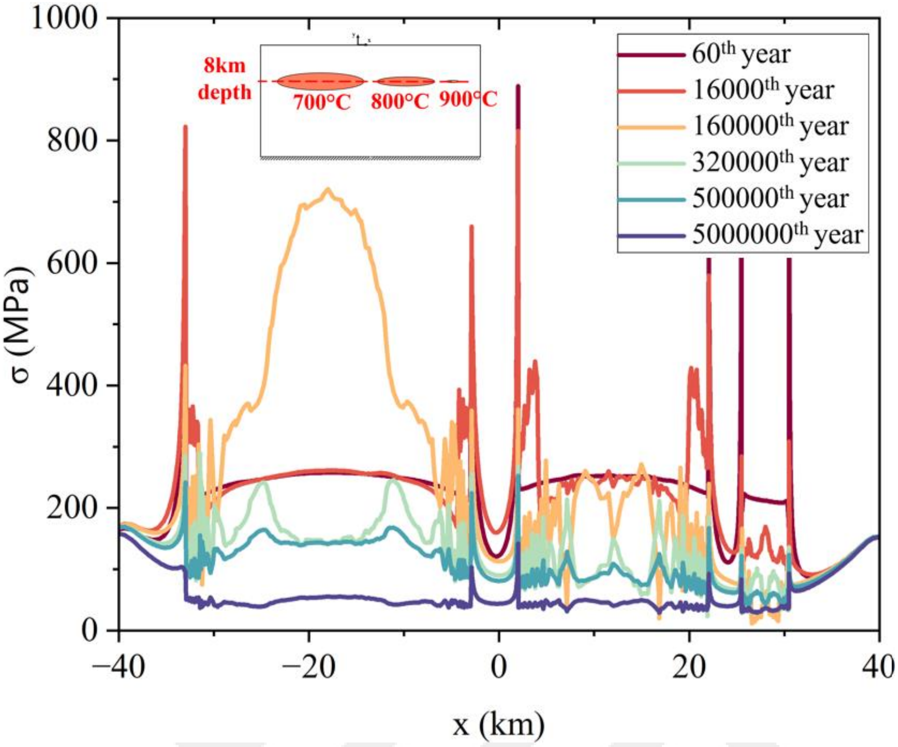

Figure 3.48. Von mises stress on midline (-8 km) - D_8-8-8, T_7-8-9 (2D)

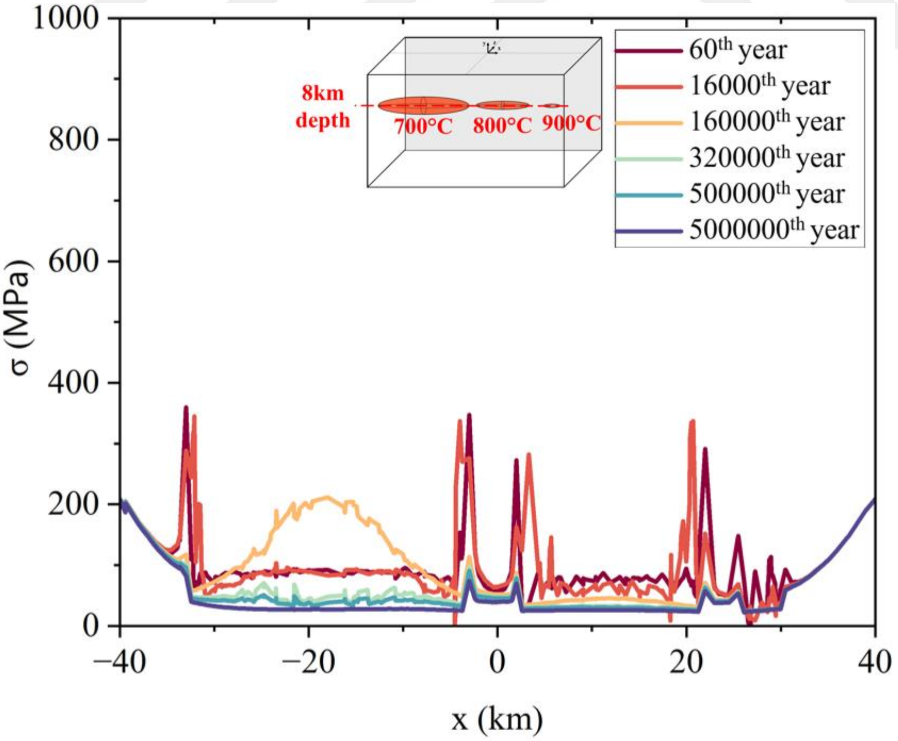

Figure 3.49. Von mises stress on midline (-8 km) - D_8-8-8, T_7-8-9 (3D)

Similar to the situation in case D_3-3-3, T_7-8-9, previous results obtained at 8 km depth are very comparable to case D_8-8-8, T_7-8-9. We can infer that, rather than the initial magma temperature, the depth, or more specifically the surrounding temperature, is much more dominant in these profiles, with the initial magma temperature only serving to shift the process. Although the difference between pattern of the 2D and 3D models appears significant, it is primarily due to the much faster thermal stages in the 3D model, which completes them more rapidly and reflects the later stages of the 2D model, showing the chamber edges with fewer discontinuities.

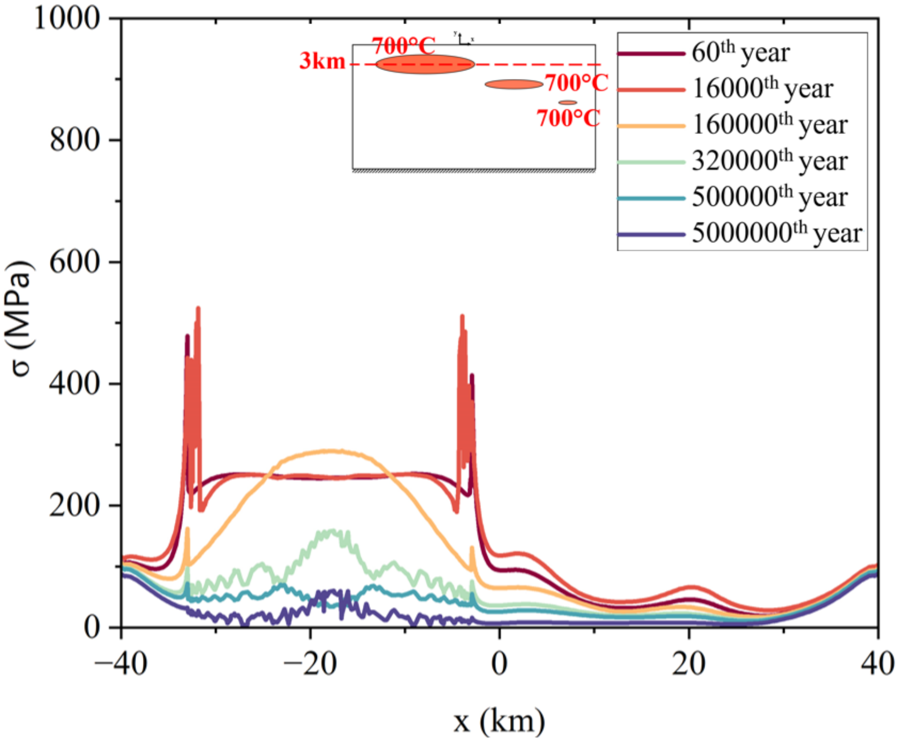

Figure 3.50. Von mises stress on midline (-3 km) - D_3-8-12, T_7-7-7 (2D)

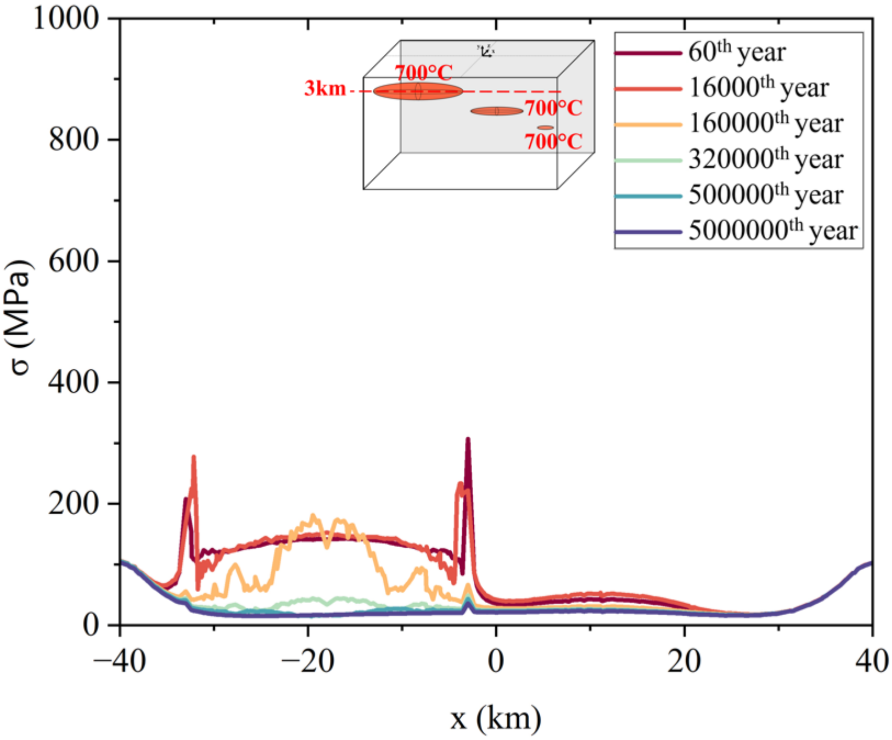

Figure 3.51. Von mises stress on midline (-3 km) - D_3-8-12, T_7-7-7 (3D)

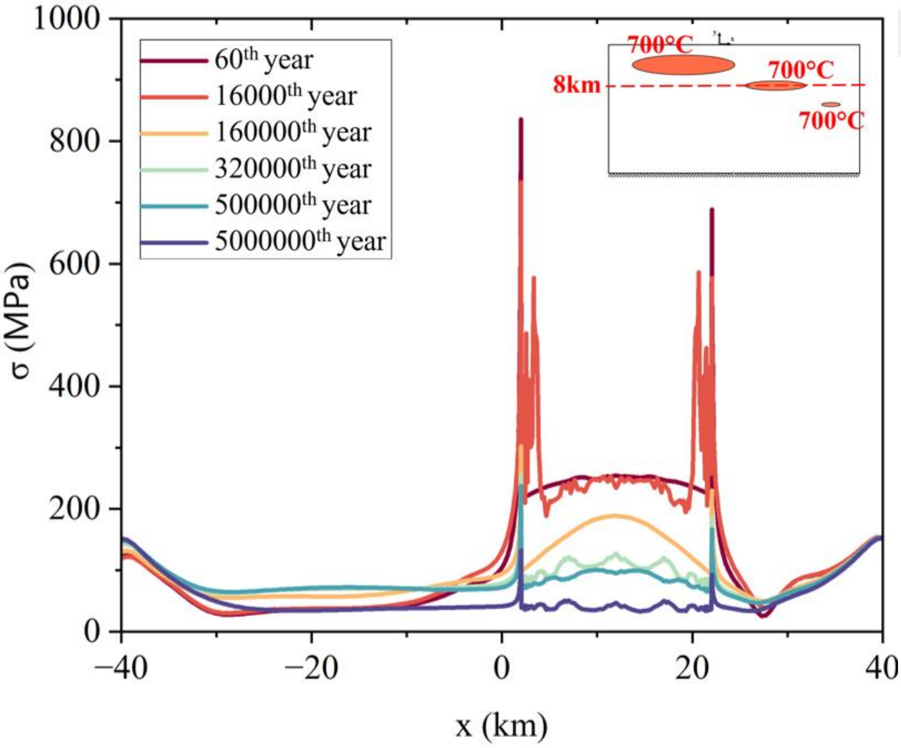

Figure 3.52. Von mises stress on midline (-8 km) - D_3-8-12, T_7-7-7 (2D)

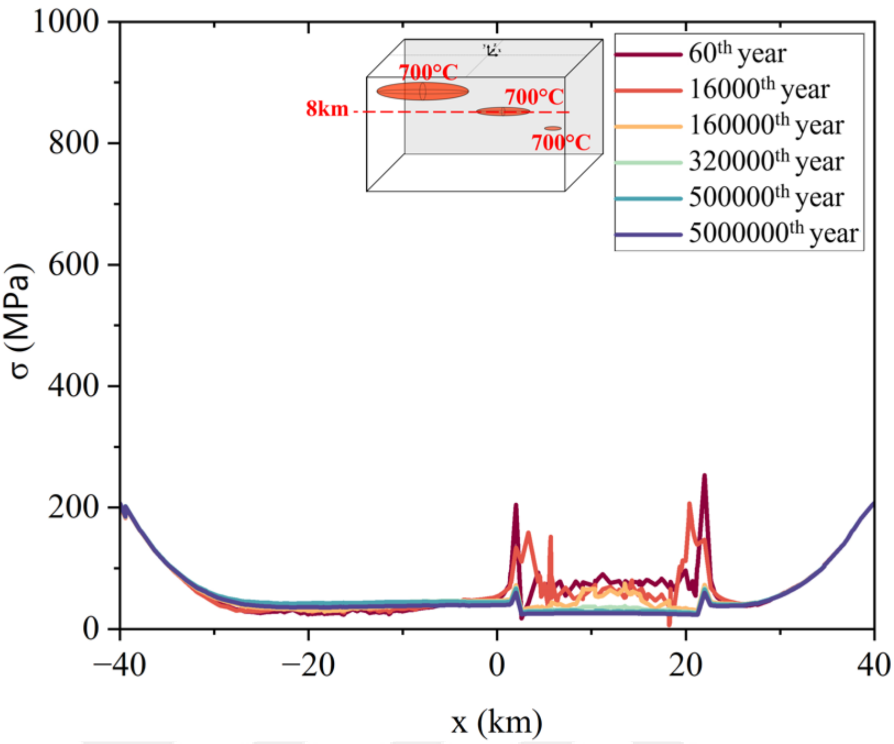

Figure 3.53. Von mises stress on midline (-8 km) - D_3-8-12, T_7-7-7 (3D)

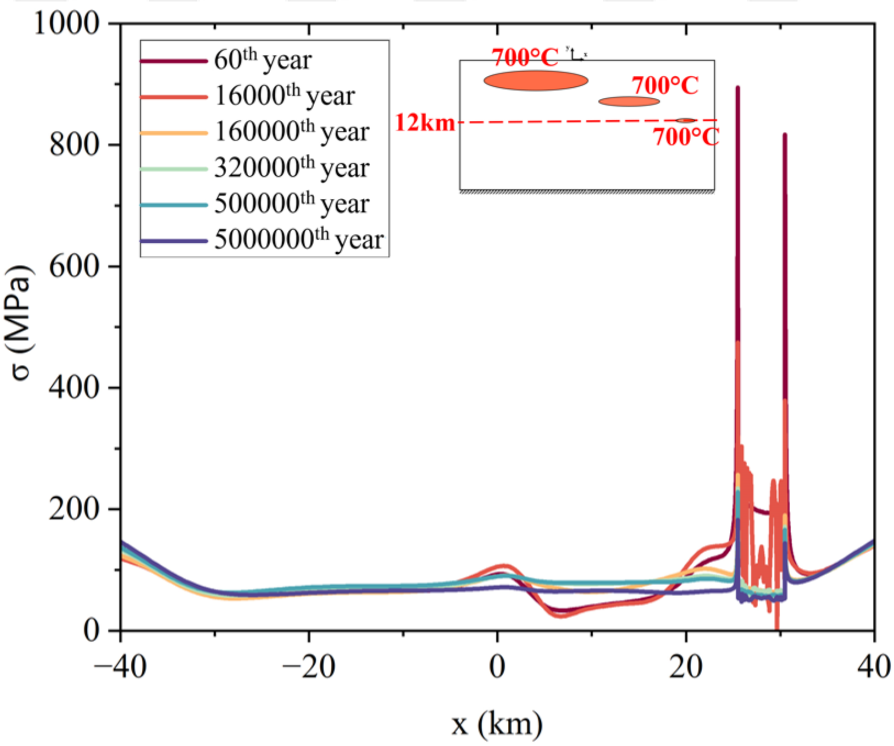

Figure 3.54. Von mises stress on midline (-12 km) - D_3-8-12, T_7-7-7 (2D)

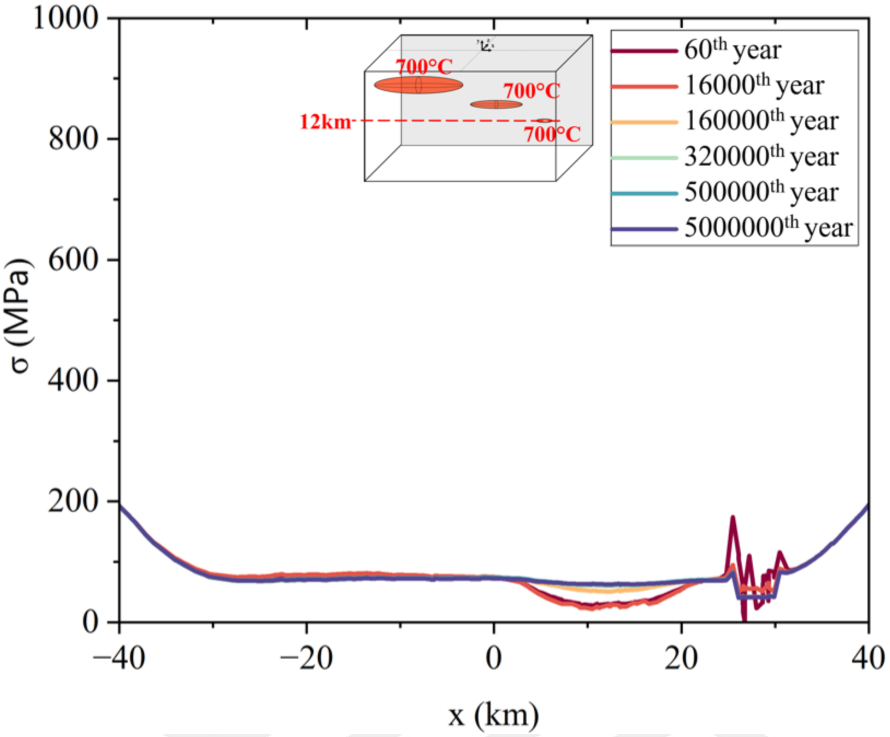

Figure 3.55. Von mises stress on midline (-12 km) - D_3-8-12, T_7-7-7 (3D)

In the case where the magma chambers are at the same temperature but at different depths, whose stress profiles at midlines are given in Figures 3.50-3.55, stresses around the chambers exhibit very similar behavior to those observed in previous configurations at the same depth. The differences that arise are due to the presence of the three chambers affecting the domain's temperature gradient in a different direction, resulting in a significant deviation from the previous results in 3D.

In 2D, when compared to the D_3-3-3, T_7-7-7 case, the time for stress to concentrate at the center of LMC is earlier. This is because, in this case, the solidification process occurs 0.18% earlier. As a result, stress concentration, which tends to accumulate around the liquid material, takes shorter to reach the center due to the acceleration in solidification. This may be because the heat affected area, which is present at near lateral shallow tails of chambers when the chambers are placed side by side, now is not present near the chambers. In the 3D model, the overall stress magnitudes are 40% lower than in the 2D model, reflecting a trend of faster solidification.

In the previous cases, midline for both chambers were common, therefore the stresses caused by magma chambers could be obtained only inside the magma domain and lateral edges. As D_3-8-12, T_7-7-7 stress results are taken from three different midlines passing from each magma chamber center, investigation of magma chambers effects to neighbor host rocks are also applicable. At 3 km depth (Figures 3.50-3.51), MMC cause a maximum stress of 80MPa at 16000th year. At earlier phase, the stress it caused is 12% lower because temperature has not yet been distributed and expansion effects are not yet significant. Stresses caused by chambers at lower depths occurs at the trajectory of their host rock-magma interface, at the shallow tails. It is not abrupt as the peak stresses occurring at the midlines at those shallow tails to influence the host rock at 5 km away.

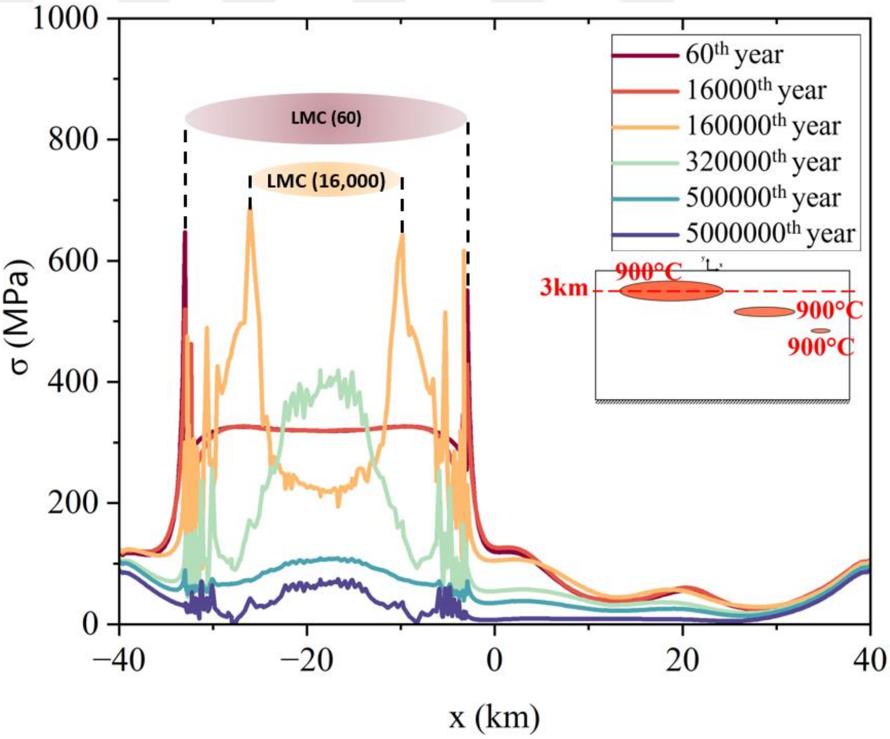

Figure 3.56. Von mises stress on midline (-3 km) - D_3-8-12, T_9-9-9 (2D)

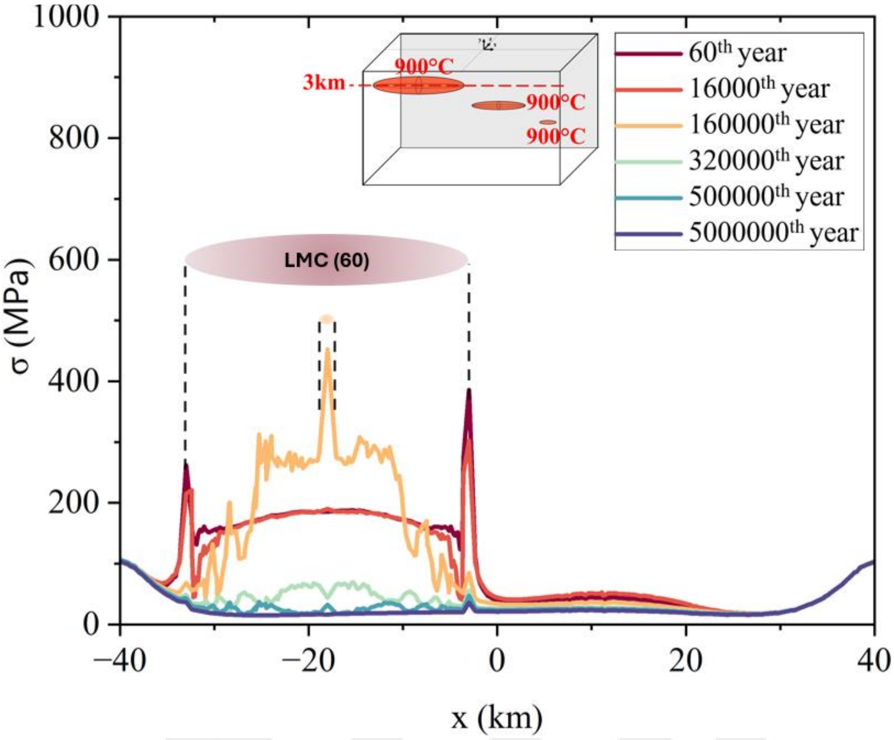

Figure 3.57. Von mises stress on midline (-3 km) - D_3-8-12, T_9-9-9 (3D)

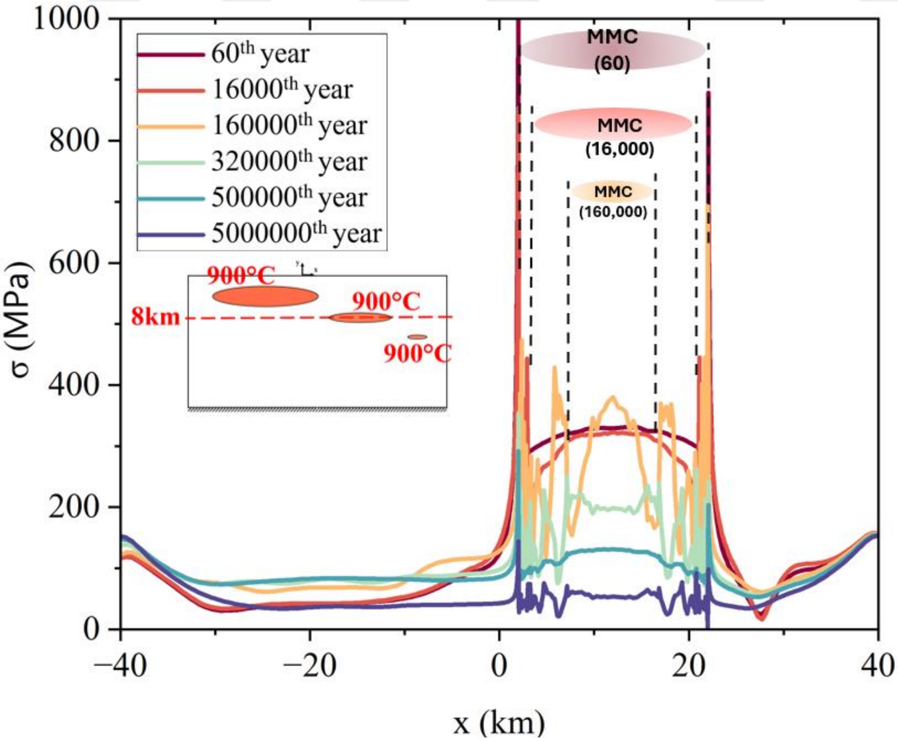

Figure 3.58. Von mises stress on midline (-8 km) - D_3-8-12, T_9-9-9 (2D)

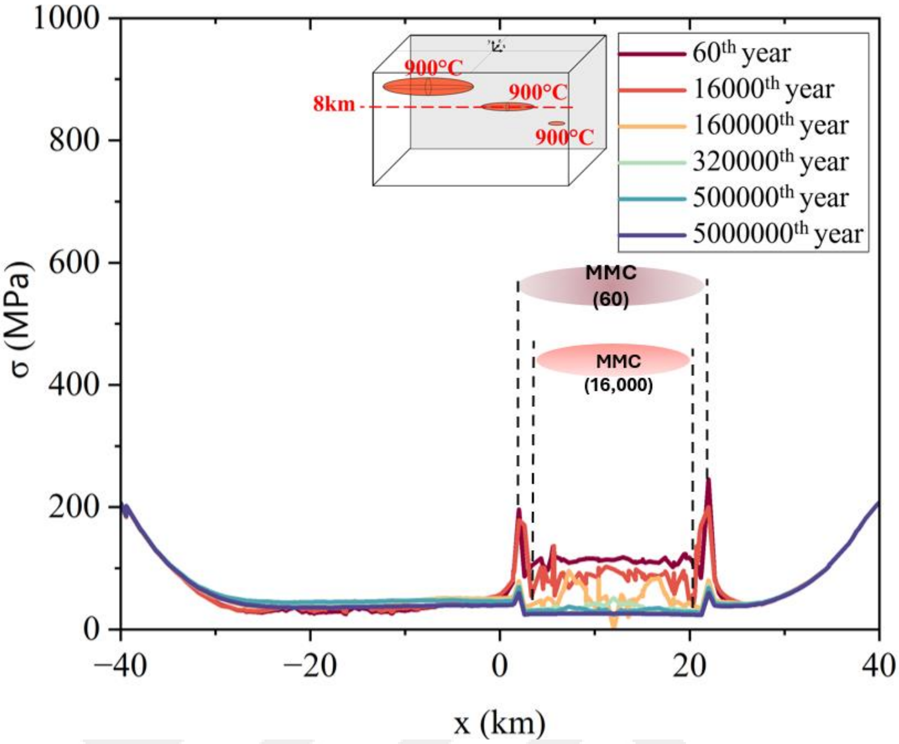

Figure 3.59. Von mises stress on midline (-8 km) - D_3-8-12, T_9-9-9 (3D)

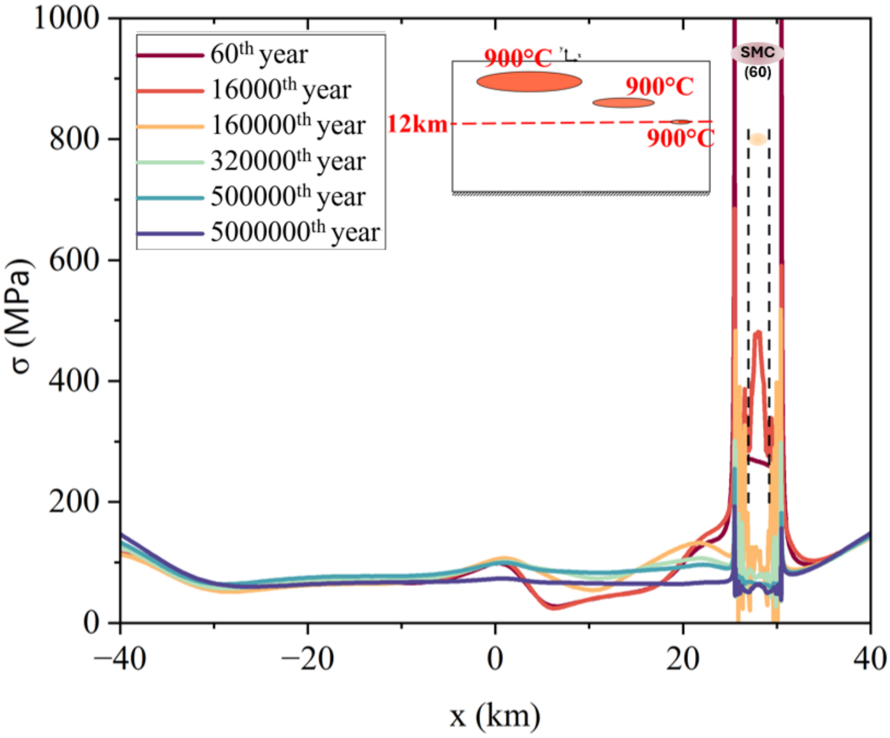

Figure 3.60. Von mises stress on midline (-12 km) - D_3-8-12, T_9-9-9 (2D)

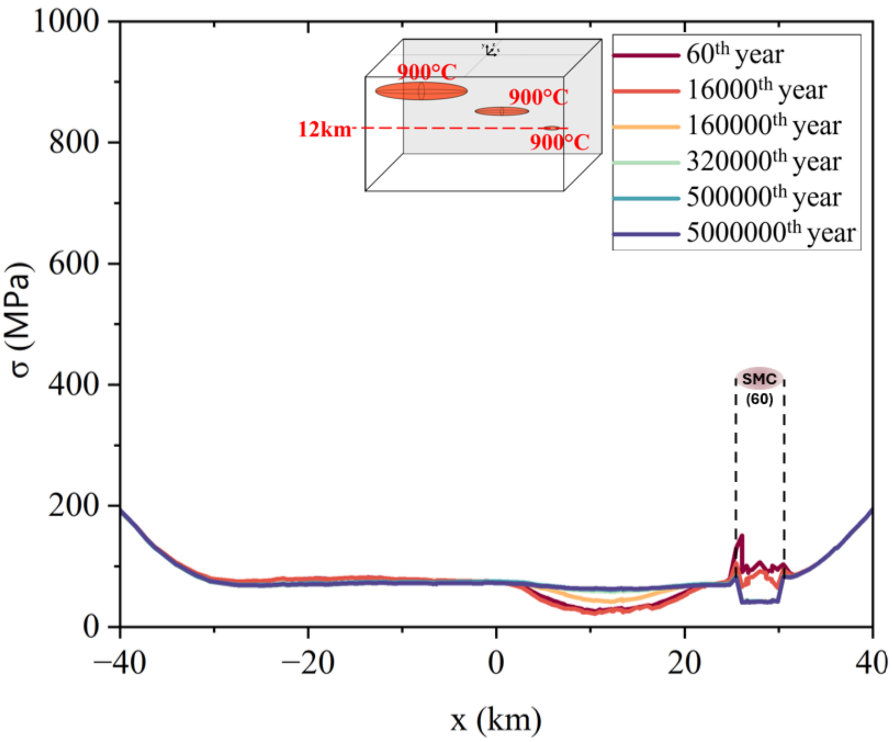

Figure 3.61. Von mises stress on midline (-12 km) - D_3-8-12, T_9-9-9 (3D)

In case D_3-8-12, T_9-9-9, the results closely resemble those of the case D_3-8-12, T_7-7-7. Differences arise from the higher initial temperature, which delays the solidification process and shifts the temperature dependent stress formation over time. Higher stresses are exhibited due to the elevated initial magma temperature.

LMC totally solidifies at year 286508 years in 2D for this case. The horn like stress profile at 160000th year in Figure 3.56 is because part of magma has solidified and the new solid fluid interface at that moment is at the peaks of this graph in x direction. In year 320000 total solidification has completed but a great temperature gradient is present at between x coordinates -25 and -15; leading to thermal expansion/contraction caused high stresses. When it is compared to the 3D case given in Figure 3.57, where the solidification is complete at 162489th year, it is clearly seen that the crystal region only remained at the center of LMC at 160000th year, therefore the highest stress is present there, with thermal expansion still occurring at the old magma chamber regions transformed to host rock. The magma geometries remained unsolidified are given on Figures 3.56-3.57.

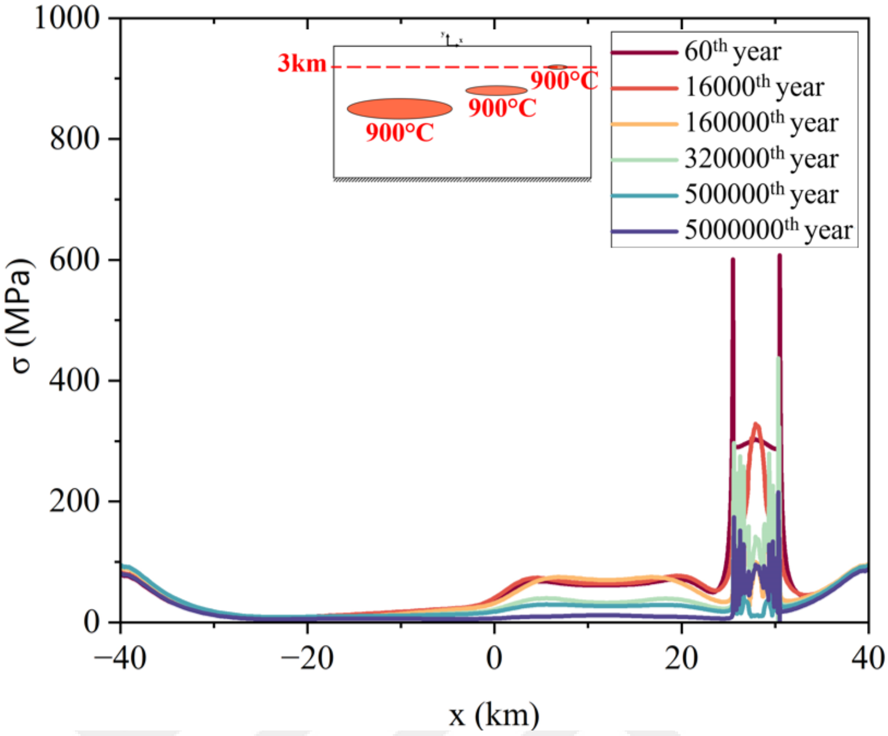

Figure 3.62. Von mises stress on midline (-3 km) - D_12-8-3, T_9-9-9 (2D)

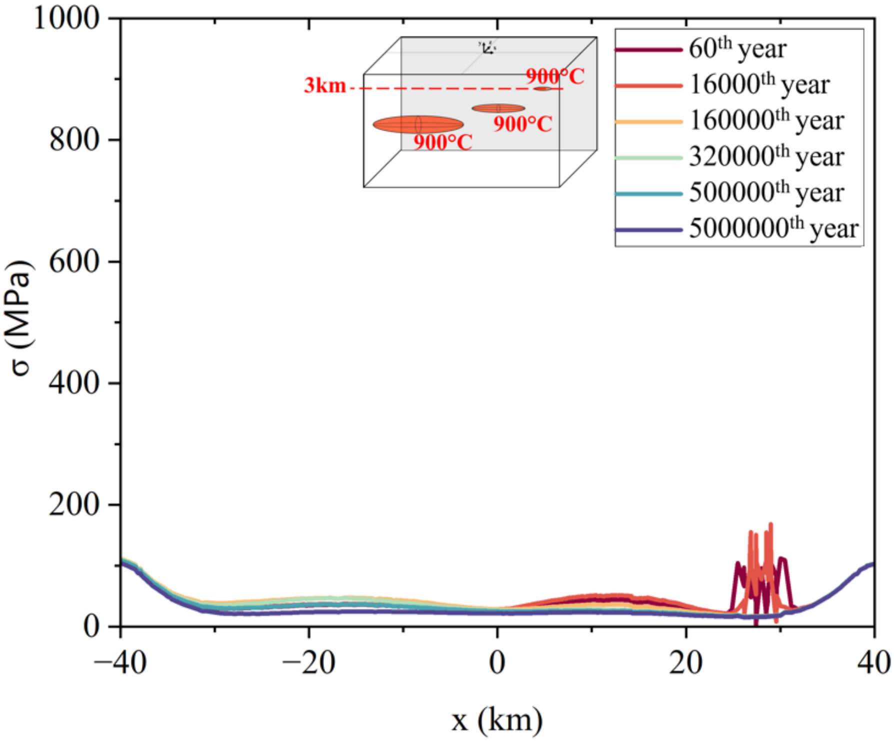

Figure 3.63. Von mises stress on midline (-3 km) - D_12-8-3, T_9-9-9 (3D)

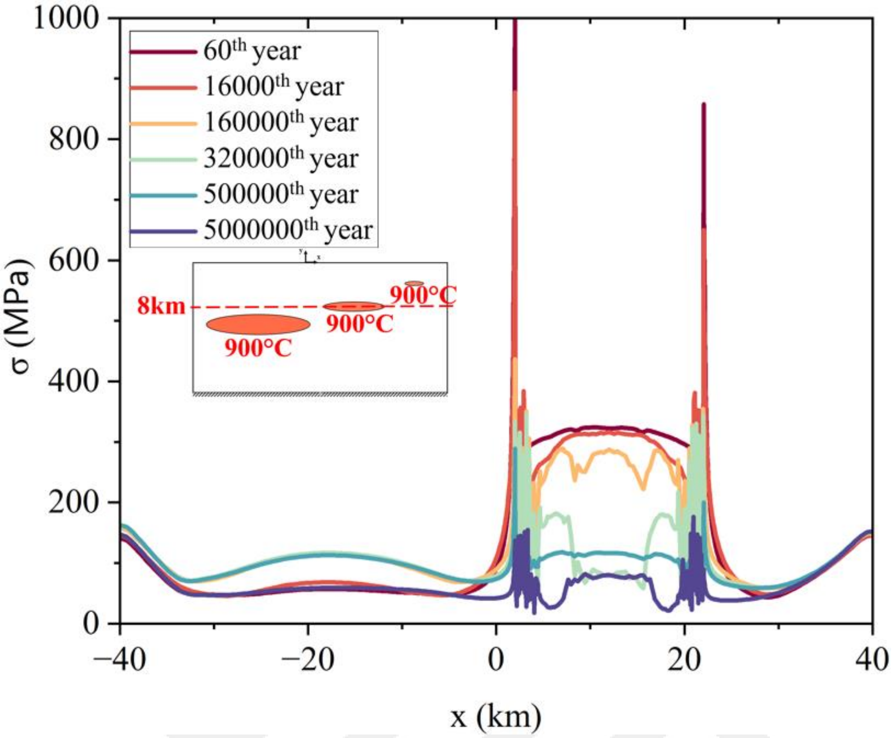

Figure 3.64. Von mises stress on midline (-8 km) - D_12-8-3, T_9-9-9 (2D)

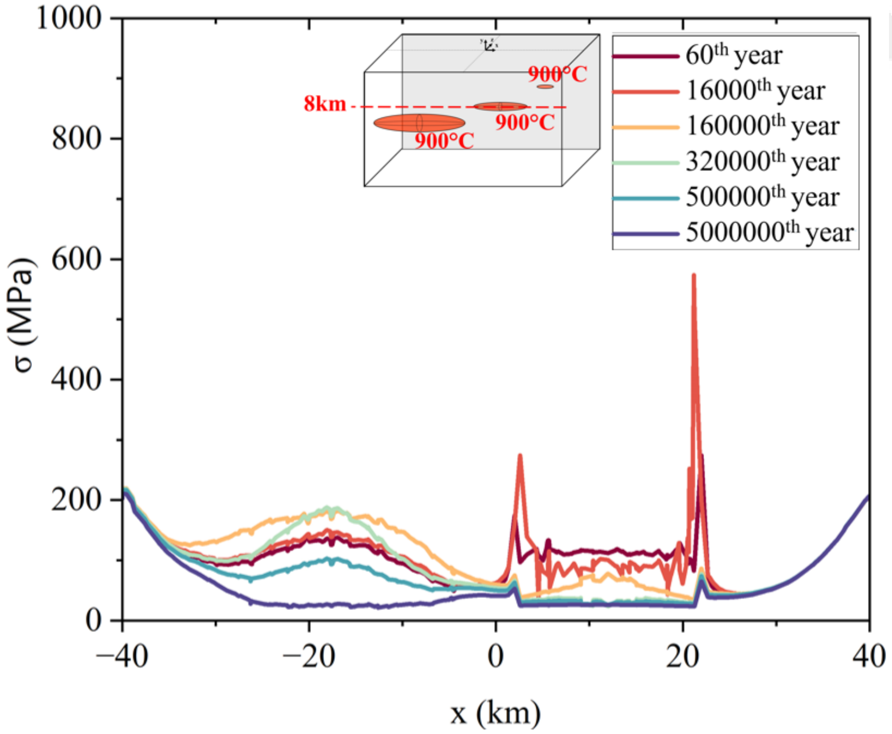

Figure 3.65. Von mises stress on midline (-8 km) - D_12-8-3, T_9-9-9 (3D)

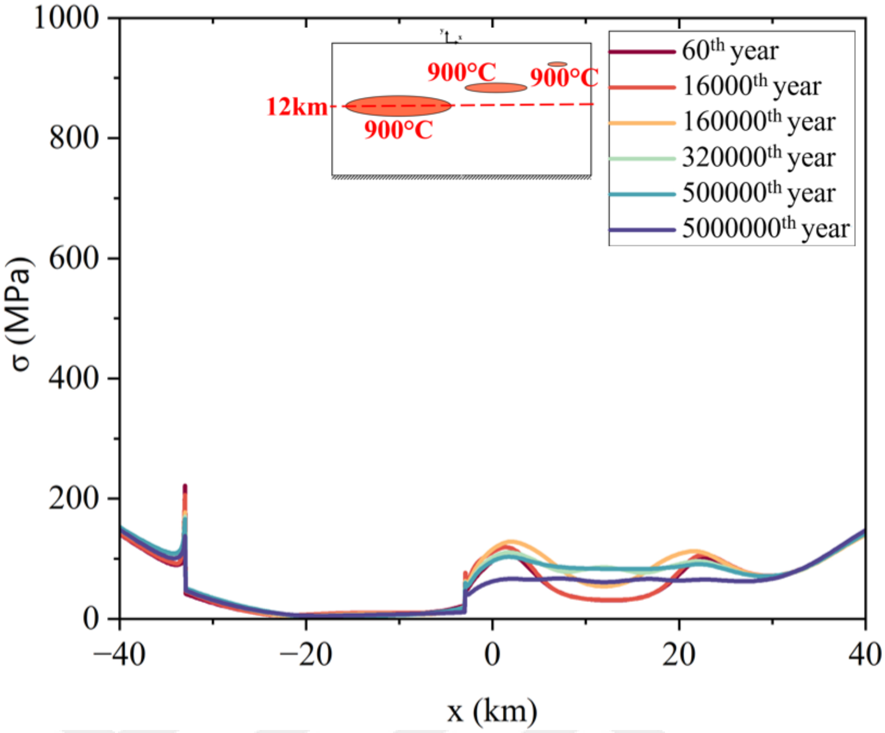

Figure 3.66. Von mises stress on midline (-12 km) - D_12-8-3, T_9-9-9 (2D)

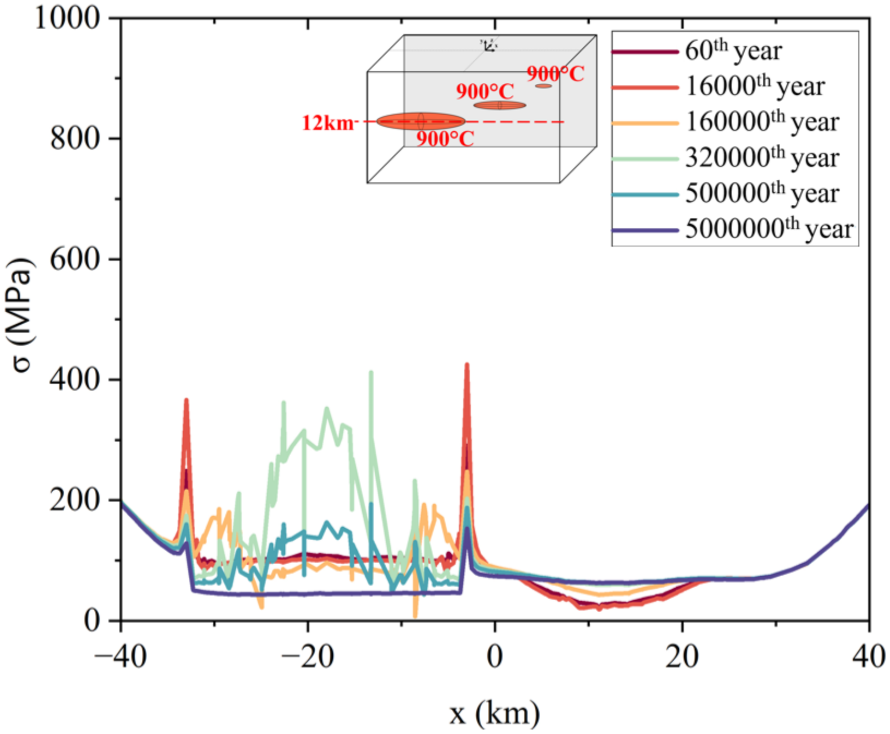

Figure 3.67. Von mises stress on midline (-12 km) - D_12-8-3, T_9-9-9 (3D)

Case D_12-8-3, T_9-9-9 represents the most geologically plausible configuration, characterized by the largest chamber, which can be described as a reservoir existing in a deeper region. The most notable difference in this configuration is the extremely low stress observed within LMC along its midline. Upon investigation, this is attributed to the exclusion of the thermal expansion effect for this chamber in the model. This adjustment is intentionally left unchanged to highlight the significance of the thermal expansion effect, as the behavior of this chamber across numerous cases provides insight into an important detail. While stress values considering thermal expansion are unrealistically high compared to natural processes, neglecting thermal expansion results in stress values ranging between 0–20 MPa, illustrating the substantial impact of thermal effects. The very high stress magnitudes observed within the magma chamber suggest that these arise from differential expansion caused by temperature gradients within the magma itself.

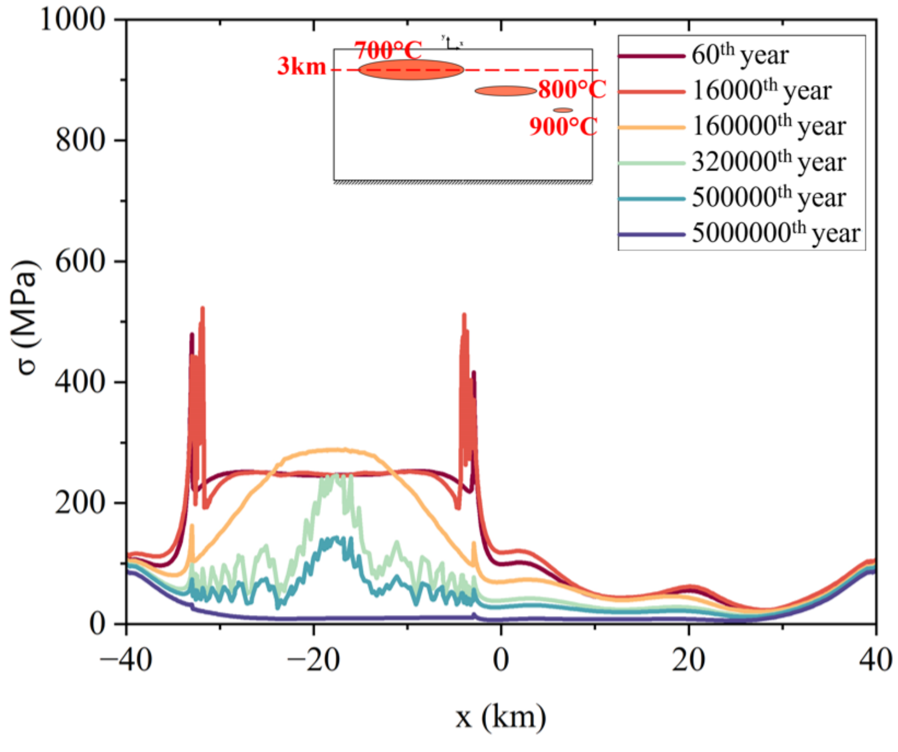

Figure 3.68. Von mises stress on midline (-3 km) - D_3-8-12, T_7-8-9 (2D)

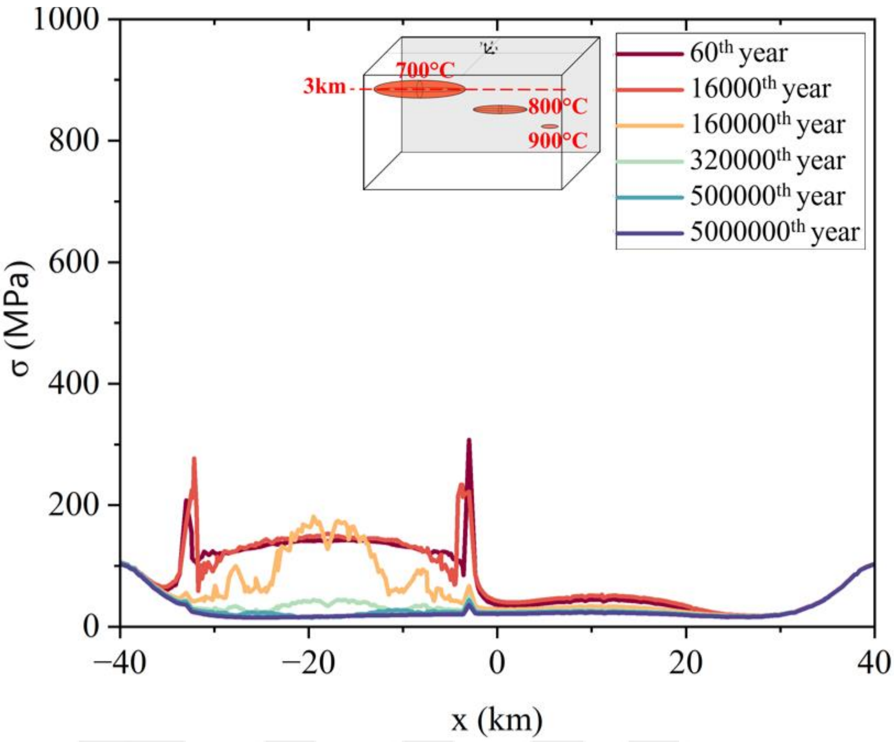

Figure 3.69. Von mises stress on midline (-3 km) - D_3-8-12, T_7-8-9 (3D)

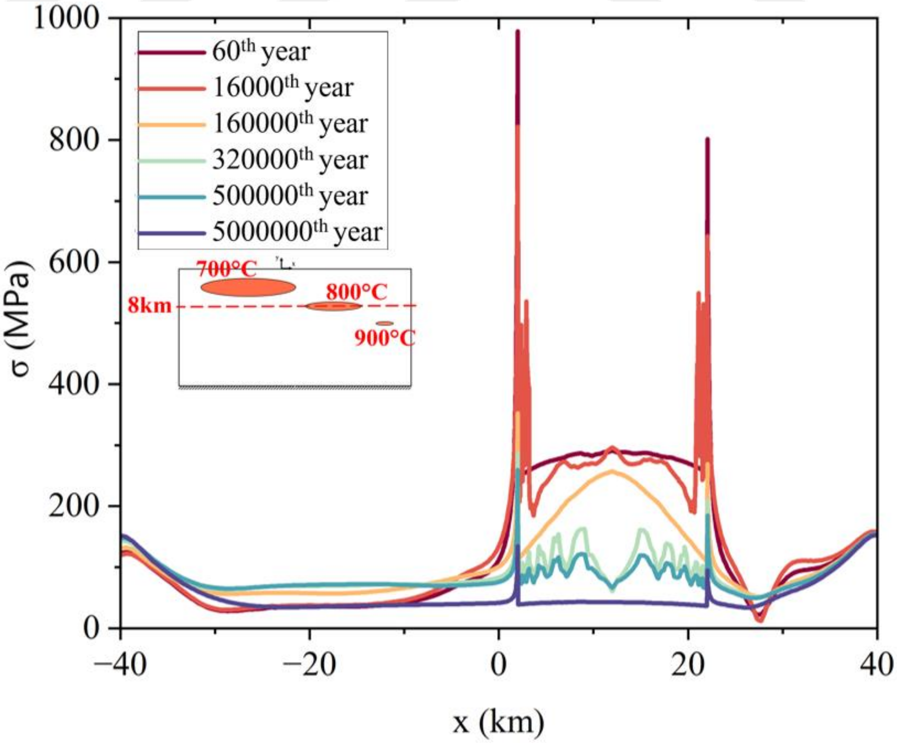

Figure 3.70. Von mises stress on midline (-8 km) - D_3-8-12, T_7-8-9 (2D)

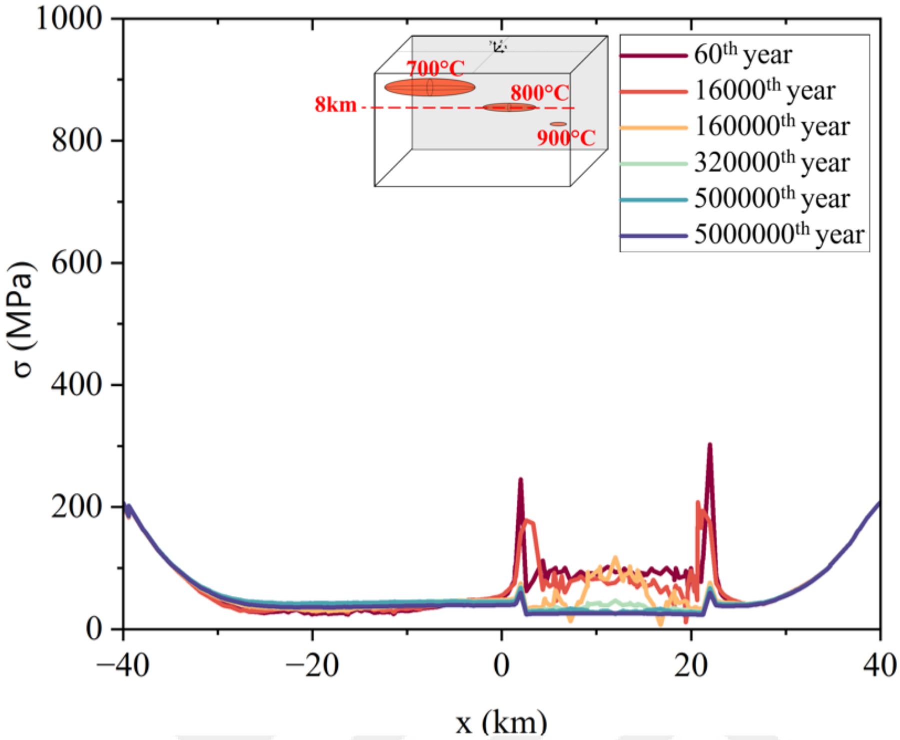

Figure 3.71. Von mises stress on midline (-8 km) - D_3-8-12, T_7-8-9 (3D)

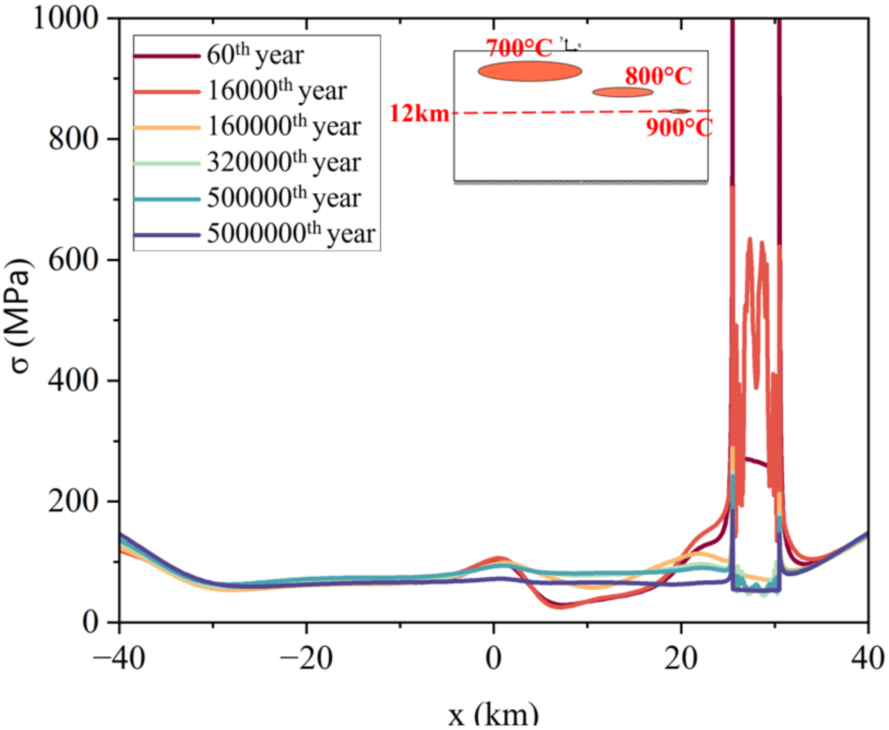

Figure 3.72. Von mises stress on midline (-12 km) - D_3-8-12, T_7-8-9 (2D)

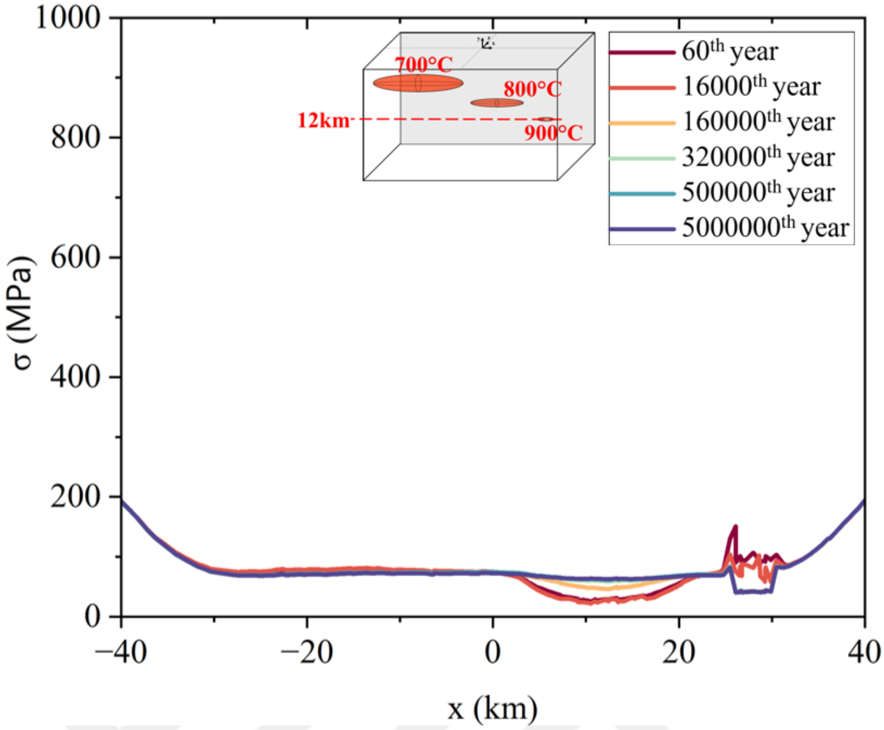

Figure 3.73. Von mises stress on midline (-12 km) - D_3-8-12, T_7-8-9 (3D)

D_3-8-12, T_7-8-9 has similar physical explanations as the previous cases, but it serves as a good example for observing anomalous fluctuations in the graphs. This behavior is more prominent in the 3D model, and the reason for this is the assignment of mesh elements at a meter scale, even with a fine mesh, over a very large domain. Particularly in the 3D model, due to the large control volume and extended time domain, it is not feasible to use very high mesh resolutions to avoid convergence issues. Although element inconsistencies occur in this case, the overall trends are clear, and the results are considered sufficient for interpretation.

When Figures 3.70-3.73 are examined, it is seen that LMC does not have a significant effect on the stress distributions at 12 km but shows slight effects on 8 km. MMC, however, cause the stresses at its projection on 12 km depth to decrease where it causes the stresses to increase at 3 km depth. This could be attributed to the effects of volumetric contraction as the magma cools and solidifies, influencing stress transfer differently with varying depths. In deeper regions, where lithostatic stress and Young’s modulus is higher, the material’s contraction may reduce stress as surrounding rocks pull the solidified magma while in shallower regions, the material compresses the near surface layers having lower stiffness, causing an increase in stress. SMC does not have a significant effect even on the closer upper midline (8 km depth) because of its small volume.

CHAPTER 4

CONCLUSION AND FUTURE WORK

Two-dimensional and three-dimensional analyses are conducted for magma chamber cases with varying depths and initial internal temperature values. The resulting findings and observations from these analyses are summarized in this section.

In all cases of the 2D and 3D simulations, the overall temperature patterns are consistent; however, significantly faster cooling -in the order of magnitude of an average of 2.14 times- is observed in the 3D model. This discrepancy arises from the inherent differences in heat transfer dynamics between 2D and 3D systems. In the 3D model, heat is dissipated in all three spatial directions, allowing for a more efficient transfer of thermal energy to the surroundings. Conversely, the 2D model restricts heat flow to a plane, effectively limiting the pathways for heat dissipation. Additionally, the increased surface area available for heat exchange in the 3D configuration further accelerates cooling, particularly in cases involving larger temperature gradients or significant thermal conductivity contrasts. These factors collectively account for the more rapid cooling observed in the 3D model.

The rate of change of cooling rates of each magma chamber differ with distinct values between 2D and 3D model. LMC solidifies rapidly with an average of %87 higher in the 3D model when compared to the 2D model, where this value is 124% for MMC and 146% for SMC. The reason why ellipsoidal magma chambers solidify more slowly in 2D analysis compared to 3D analysis lies in the difference in heat dissipation and phase transition dynamics.

In terms of structural analysis, although 2D and 3D analyses have overlapping results by means of stress concentration pattern, the magnitudes in the 3D model differ from that in the 2D model due to the more complex structure and heat distribution. Under the same conditions, the von Mises stress outcomes in the 3D model turns out to be around 33% lower compared to those in the 2D model. When 3D model is considered, the stresses around the magma chambers can spread over a larger area, just as heat that can dissipate more efficiently in all three dimensions. This results in a more homogeneous temperature gradient in the surrounding rock, leading to lower stress values.

The analysis of thermal effects in the 2D and 3D models reveals significant differences in stress distribution, primarily driven by the behavior of thermal gradients, solidification timing, and heat transfer. At early phases, when the temperature effects are low, stresses are consistent through the chambers and concentrated at the lateral edges as expected from the physics introduced in section 1. As the host rock begins to heat and expand, magnitudes of stresses increase. Although thermal expansion of rocks and the contraction of magma chamber provides higher stresses around magma chamber boundaries, magma chamber rupture is prevented with the compressive loads around the magma chambers. Besides this, the stress values obtained from the models shows that a development of the modeling approach is required as the magnitudes are too high to encounter in nature.

As the magma chambers cool and solidify over time, the 3D model reaches thermal equilibrium much more quickly, leading to a stabilization of stresses. This is evident in the decrease in stress values towards the later time steps, steady state. Conversely, in the 2D model, due to the delayed solidification, temperature gradients remain steep for a longer period, causing higher stress concentrations, especially in the vicinity of phase transitions within the chamber. The discrepancy in solidification timing between the models significantly influences the stress patterns observed, with 3D models showing earlier phase transitions and more uniform stress distributions, while 2D models retain localized, higher stresses.

Furthermore, the geometry of the chambers and the surrounding host rock plays a crucial role. The 3D model, with its more rounded and smooth geometry, promotes a more uniform stress distribution, whereas the 2D model's more angular geometry contributes to sharper, localized stress concentrations. The differences in boundary conditions and edge effects further amplify this distinction, with 2D models showing higher stress values near the boundaries compared to the more homogeneously distributed stresses in the 3D model.

Besides the high magnitude of overall stress distributions, peak stress regions occurring at the lateral edges of the magma chambers might not represent the actual real values, they may primarily exist due to material discontinuities caused by the interface transition between magma and host rock. These high stress values are not indicative of the true stress distribution but are instead artifacts resulting from the abrupt change in material properties at the interface. Such discontinuities can lead to stress concentrations that are much higher than what would be encountered in a homogeneous material, which is why the peak stresses in these regions may appear significantly elevated.

In conclusion, the 3D model provides a more realistic representation of the stress distribution within the magma chamber system, as it accounts for more complex interactions in heat transfer and solidification processes. The 2D model, while useful for initial approximations, tends to overestimate stresses due to its simplified assumptions regarding heat flow and phase transitions. The unrealistically higher stresses in the 2D model, along with all the mentioned factors, make the 3D model more reliable for this particular physics research. Therefore, for accurate stress analysis and predictions in ellipsoidal shaped magma chamber dynamics, the 3D model proves to be more robust and appropriate.

This study has been conducted based on several assumptions and premises and it presents several areas that could be explored for further development. One of the primary issues which has been neglected is the topography effect. Although considering topography in a geological FEM model gives significant computation work and complexity in modelling, it might lead to significantly different outputs [103]. Therefore, an improvement of adding topography effects to the study or purely analyzing the topography effects can be made.

Another important aspect is that in general, the stress values obtained in the results are significantly higher than those expected in real-world scenarios, primarily due to the effects of thermal expansion. To achieve more realistic outcomes, the magma or its interface region with host rock can be modeled as a viscoelastic material as hot magma behaves as viscoelastic. However, when viscoelasticity is tried to be applied in the current modeling approach, despite solidification, the domain transitioning to host rock is still treated as viscoelastic in COMSOL. This results in outcomes that deviate from reality and fail to capture the thermal effects accurately. Therefore, a more comprehensive model that integrates viscoelasticity with the solidification process has been identified as an area for further study.

Another assumption in the modelling process is neglecting the anisotropy of rocks. As a further study, anisotropic thermal expansion can be considered because rocks having high Quartz composition can show expansions highly dependent on the axes of expansion [104].

Lastly, as validation is a highly challenging process in geology where the time domains are in million years and the geometry domain is in kilometers, some scaled down validation methods can be developed. It is an undeniable fact that in situ measurements are too hard to handle besides needing massive amount of investments. To obtain a well-verified model, temperature of a Crust geometry with a magma chamber whose age is well-known, might be obtained with an in situ measurement. A realistic modeling of this existing magma chamber should be built and the results should be fitted to the measurement. Then, a similar geometry must be scaled down and held as an experiment in situ or in a laboratory. It again should be built as a FEM model with the same methodology used in the huge domain and timescale, now adapted to the experimental domain and time. By this way, the effects of scaling down and the error can be obtained. If the error is acceptable, this method of scaling down can be useful in many forecasts.

REFERENCES

[1] Clemens, J. D., & Stevens, G. (2016). Melt segregation and magma interactions during crustal melting: Breaking out of the matrix. *Earth-Science Reviews, 160*, 333-349.

[2] Gudmundsson, A., Drymoni, K., Browning, J., Acocella, V., Amelung, F., Bonali, F. L., ... & Walter, T. R. (2022). Volcanotectonics: the tectonics and physics of volcanoes and their eruption mechanics. *Bulletin of Volcanology, 84*(8), 72.

[3] Grove, T. L. (2000). Origin of Magmas. *Encyclopedia of Volcanoes*, 133-148.

[4] Annen, C. (2009). From plutons to magma chambers: Thermal constraints on the accumulation of eruptible silicic magma in the upper crust. *Earth and Planetary Science Letters, 284*(3-4), 409-416.

[5] Sparks, R. S. J., Annen, C., Blundy, J. D., Cashman, K. V., Rust, A. C., & Jackson, M. D. (2019). Formation and dynamics of magma reservoirs. *Philosophical Transactions of the Royal society A, 377*(2139), 20180019.

[6] Jaupart, C., & Tait, S. (1995). Dynamics of differentiation in magma reservoirs. *Journal of Geophysical Research: Solid Earth, 100*(B9), 17615-17636.

[7] Ackerson, M. R., Mysen, B. O., Tailby, N. D., & Watson, E. B. (2018). Low-temperature crystallization of granites and the implications for crustal magmatism. *Nature, 559*(7712), 94-97.

[8] Paterson, S. R., Okaya, D., Memeti, V., Economos, R., & Miller, R. B. (2011). Magma addition and flux calculations of incrementally constructed magma chambers in continental margin arcs: Combined field, geochronologic, and thermal modeling studies. *Geosphere, 7*(6), 1439-1468.

[9] Bower, S. M., & Woods, A. W. (1997). Control of magma volatile content and chamber depth on the mass erupted during explosive volcanic eruptions. *Journal of Geophysical Research: Solid Earth*, *102*(B5), 10273-10290.

[10] Karaoğlu, Ö., Bayer, Ö., & Turgay, M. B. (2019). Magma odalarının termomekanik modellenmesi: Doğu Anadolu'dan bir örnek çalışma.

[11] Chaussard, E., & Amelung, F. (2014). Regional controls on magma ascent and storage in volcanic arcs. *Geochemistry, geophysics, geosystems*, *15*(4), 1407-1418.

[12] Johnson, C., Inkenbrandt, P. C., Affolter, M., & Mosher, C. (2017). OPENGEOLOGY.ORG: A free textbook for college-level introductory geology classes. *Geological Society of America Abstracts with Programs.* doi: 10.1130/abs/2017AM-307489

[13] Lesher, C. E., & Spera, F. J. (2015). Thermodynamic and transport properties of silicate melts and magma. In *The encyclopedia of volcanoes* (pp. 113-141). Academic Press.

[14] Le Maitre, R. W., Streckeisen, A., Zanettin, B., Le Bas, M. J., Bonin, B., Bateman, P., ... & Woolley, A. R. (2002). Igneous rocks. *A Classification and Glossary of Terms: Recommendations of the International Union of Geological Sciences Subcommission on the Systematics of Igneous Rocks, Cambridge University Press, Cambridge*, *2*.

[15] Rogers, N. (2015). The composition and origin of magmas. In *The encyclopedia of volcanoes* (pp. 93-112). Academic Press.

[16] Brown, M. (2013). Granite: From genesis to emplacement. *GSA bulletin*, *125*(7-8), 1079-1113.

[17] Acocella, V. (2021). *Volcano-tectonic processes* (Vol. 567). Switzerland: Springer.

[18] Gregg, P. M., Grosfils, E. B., & de Silva, S. L. (2015). Catastrophic caldera-forming eruptions II: The subordinate role of magma buoyancy as an eruption trigger. *Journal of Volcanology and Geothermal Research, 305*, 100-113.

[19] Schmincke, H. U. (2004). *Volcanism* (Vol. 28). Springer Science & Business Media.

[20] Swanson, S. E., & Fenn, P. M. (1986). Quartz crystallization in igneous rocks. *American Mineralogist, 71*(3-4), 331-342.

[21] Bateman, P. C., & Chappell, B. W. (1979). Crystallization, fractionation, and solidification of the Tuolumne intrusive series, Yosemite National Park, California. *Geological Society of America Bulletin, 90*(5), 465-482.

[22] Gudmundsson, A. (2011). *Rock fractures in geological processes.* Cambridge University Press, 22.

[23] Amadei, B., & Stephansson, O. (2012). *Rock stress and its measurement.* Springer Science & Business Media.

[24] Gudmundsson, A. (1990). Emplacement of dikes, sills and crustal magma chambers at divergent plate boundaries. *Tectonophysics, 176*(3-4), 257-275.

[25] Cai, X., Yuan, J., Zhou, Z., Pi, Z., Tan, L., Wang, P., ... & Wang, S. (2023). Effects of hole shape on mechanical behavior and fracturing mechanism of rock: Implications for instability of underground openings. *Tunnelling and Underground Space Technology, 141*, 105361.

[26] Karaoğlu, Ö., Browning, J., Bazargan, M., & Gudmundsson, A. (2016). Numerical modelling of triple-junction tectonics at Karlıova, Eastern Turkey, with implications for regional magma transport. *Earth and Planetary Science Letters, 452*, 157-170.

[27] Yao, Y. (2012). Linear elastic and cohesive fracture analysis to model hydraulic fracture in brittle and ductile rocks. *Rock mechanics and rock engineering, 45*, 375-387.

[28] Gercek, H. (2007). Poisson's ratio values for rocks. *International Journal of Rock Mechanics and Mining Sciences, 44*(1), 1-13.

[29] Rybacki, E., Reinicke, A., Meier, T., Makasi, M., & Dresen, G. (2015). What controls the mechanical properties of shale rocks?–Part I: Strength and Young's modulus. *Journal of Petroleum Science and Engineering, 135*, 702-722.

[30] Suppe, J. (2014). Fluid overpressures and strength of the sedimentary upper crust. *Journal of Structural Geology, 69*, 481-492.

[31] Fredrich, J. T., & Wong, T. F. (1986). Micromechanics of thermally induced cracking in three crustal rocks. *Journal of Geophysical Research: Solid Earth, 91*(B12), 12743-12764.

[32] Rahimi, R., & Nygaard, R. (2015). Comparison of rock failure criteria in predicting borehole shear failure. *International Journal of Rock Mechanics and Mining Sciences, 79*, 29-40.

[33] Sparks, R. S. J., Huppert, H. E., & Turner, J. S. (1984). The fluid dynamics of evolving magma chambers. *Philosophical Transactions of the Royal Society of London. Series A, Mathematical and Physical Sciences, 310*(1514), 511-534.

[34] Huppert, H. E., & Sparks, R. S. J. (1988). The generation of granitic magmas by intrusion of basalt into continental crust. *Journal of Petrology, 29*(3), 599-624.

[35] Petcovic, H. L., & Dufek, J. D. (2005). Modeling magma flow and cooling in dikes: Implications for emplacement of Columbia River flood basalts. *Journal of Geophysical Research: Solid Earth, 110*(B10).

[36] Annen, C., Pichavant, M., Bachmann, O., & Burgisser, A. (2008). Conditions for the growth of a long-lived shallow crustal magma chamber below Mount Pelee volcano (Martinique, Lesser Antilles Arc). *Journal of Geophysical Research: Solid Earth*, *113*(B7).

[37] Gutiérrez, F., Payacán, I., Gelman, S. E., Bachmann, O., & Parada, M. A. (2013). Late-stage magma flow in a shallow felsic reservoir: Merging the anisotropy of magnetic susceptibility record with numerical simulations in La Gloria Pluton, central Chile. *Journal of Geophysical Research: Solid Earth*, *118*(5), 1984-1998.

[38] Cashman, K. V., & Marsh, B. D. (1988). Crystal size distribution (CSD) in rocks and the kinetics and dynamics of crystallization II: Makaopuhi lava lake. *Contributions to Mineralogy and Petrology*, *99*(3), 292-305.

[39] Cashman, K. V. (1990). Textural constraints on the kinetics of crystallization of igneous rocks. *Reviews in mineralogy and geochemistry*, *24*(1), 259-314.

[40] Cashman, K. V. (1992). Groundmass crystallization of Mount St. Helens dacite, 1980–1986: a tool for interpreting shallow magmatic processes. *Contributions to Mineralogy and Petrology*, *109*(4), 431-449.

[41] Albarede, F., & Bottinga, Y. (1972). Kinetic disequilibrium in trace element partitioning between phenocrysts and host lava. *Geochimica et Cosmochimica Acta*, *36*(2), 141-156.

[42] Lofgren, G. (1980). Experimental studies on the dynamic crystallization of silicate melts. *Physics of magmatic processes*, *487*, 551.

[43] Grove, T. L., & Bence, A. E. (1977). Experimental study of pyroxene-liquid interaction in quartz-normative basalt 15597. In: *Lunar Science Conference, 8th, Houston, Tex., March 14-18, 1977, Proceedings. Volume 2.(A78-41551 18-91) New York, Pergamon Press, Inc., 1977, p. 1549-1579.* (Vol. 8, pp. 1549-1579).

[44] Kotash, A. K. (2021). Volatiles and Geochemical Fingerprinting of Plagioclase-Hosted Melt Inclusions from Mid-Ocean Ridge Lavas: Determination of Depth of Crystallization and Melt Composition in the Lower Crust.

[45] Rubin, A. E., Cooper, K. M., Till, C. B., Kent, A. J., Costa, F., Bose, M., ... & Cole, J. (2017). Rapid cooling and cold storage in a silicic magma reservoir recorded in individual crystals. *Science, 356*(6343), 1154-1156.

[46] Ackerson, M. R., Mysen, B. O., Tailby, N. D., & Watson, E. B. (2018). Low-temperature crystallization of granites and the implications for crustal magmatism. *Nature, 559*(7712), 94-97.

[47] Bea, F. (2010). Crystallization dynamics of granite magma chambers in the absence of regional stress: multiphysics modeling with natural examples. *Journal of Petrology, 51*(7), 1541-1569.

[48] Delaney, P. T., & Pollard, D. D. (1982). Solidification of basaltic magma during flow in a dike. *American Journal of Science, 282*(6), 856-885.

[49] Annen, C., Pichavant, M., Bachmann, O., & Burgisser, A. (2008). Conditions for the growth of a long-lived shallow crustal magma chamber below Mount Pelee volcano (Martinique, Lesser Antilles Arc). *Journal of Geophysical Research: Solid Earth, 113*(B7).

[50] de Silva, S. L., & Gregg, P. M. (2014). Thermomechanical feedbacks in magmatic systems: Implications for growth, longevity, and evolution of large caldera-forming magma reservoirs and their supereruptions. *Journal of Volcanology and Geothermal Research, 282*, 77-91.

[51] Bea, F. (2010). Crystallization dynamics of granite magma chambers in the absence of regional stress: multiphysics modeling with natural examples. *Journal of Petrology, 51*(7), 1541-1569.

[52] Douglas, M. M., Geyer, A., Álvarez-Valero, A. M., & Martí, J. (2016). Modeling magmatic accumulations in the upper crust: Metamorphic implications for the country rock. *Journal of Volcanology and Geothermal Research, 319,* 78-92.

[53] Mollo, S., Lanzafame, G., Masotta, M., Iezzi, G., Ferlito, C., & Scarlato, P. (2011). Cooling history of a dike as revealed by mineral chemistry: a case study from Mt. Etna volcano. *Chemical Geology, 288*(1-2), 39-52.

[54] Monteux, J., Andrault, D., & Samuel, H. (2016). On the cooling of a deep terrestrial magma ocean. *Earth and Planetary Science Letters, 448,* 140-149.

[55] Gelman, S. E., Gutiérrez, F. J., & Bachmann, O. (2013). On the longevity of large upper crustal silicic magma reservoirs. *Geology, 41*(7), 759-762.

[56] Nabelek, P. I., Hofmeister, A. M., & Whittington, A. G. (2012). The influence of temperature-dependent thermal diffusivity on the conductive cooling rates of plutons and temperature-time paths in contact aureoles. *Earth and Planetary Science Letters, 317,* 157-164.

[57] Liu, L., & Lowell, R. P. (2011). Modeling heat transfer from a convecting, crystallizing, replenished silicic magma chamber at an oceanic spreading center. *Geochemistry, Geophysics, Geosystems, 12*(9).

[58] Costa, F., Shea, T., & Ubide, T. (2020). Diffusion chronometry and the timescales of magmatic processes. *Nature Reviews Earth & Environment, 1*(4), 201-214.

[59] Daniels, K. A., Bastow, I. D., Keir, D., Sparks, R. S. J., & Menand, T. (2014). Thermal models of dyke intrusion during development of continent–ocean transition. *Earth and Planetary Science Letters, 385,* 145-153.

[60] Mollo, S., Lanzafame, G., Masotta, M., Iezzi, G., Ferlito, C., & Scarlato, P. (2011). Cooling history of a dike as revealed by mineral chemistry: a case study from Mt. Etna volcano. *Chemical Geology, 288*(1-2), 39-52.

[61] Jackson, M. D., Blundy, J., & Sparks, R. S. J. (2018). Chemical differentiation, cold storage and remobilization of magma in the Earth's crust. *Nature*, *564*(7736), 405-409.

[62] Jiang, C. H., Wang, D., Du, D. H., & Wang, X. L. (2023). Estimation of an ephemeral cooling for silicic magma reservoirs using thermal simulation. *Journal of Asian Earth Sciences, 241*, 105442.

[63] Webber, K. L., Simmons, W. B., Falster, A. U., & Foord, E. E. (1999). Cooling rates and crystallization dynamics of shallow level pegmatite-aplite dikes, San Diego County, California. *American Mineralogist*, *84*(5-6), 708-717.

[64] Karakas, O., Degruyter, W., Bachmann, O., & Dufek, J. (2017). Lifetime and size of shallow magma bodies controlled by crustal-scale magmatism. *Nature Geoscience*, *10*(6), 446-450.

[65] Dunbar, N. W., Jacobs, G. K., & Naney, M. T. (1995). Crystallization processes in an artificial magma: variations in crystal shape, growth rate and composition with melt cooling history. *Contributions to Mineralogy and Petrology, 120*, 412-425.

[66] Rodríguez, C., Geyer, A., Castro, A., & Villaseñor, A. (2015). Natural equivalents of thermal gradient experiments. *Journal of Volcanology and Geothermal Research*, *298*, 47-58.

[67] Tarhan, N., (1991). Hınıs–Varto–Karlıova (Erzurum–Muş–Bingöl) dolayındaki neojen volkanitlerinin jeolojisi ve petrolojisi. *MTA Dergisi 113,* 1–15.

[68] Gudmundsson, A. (2004). Effects of Young's modulus on fault displacement. Comptes rendus. *Géoscience, 336*(1), 85-92.

[69] Gudmundsson, A., & Brenner, S. L. (2001). How hydrofractures become arrested. *Terra Nova*, *13*(6), 456-462.

[70] Gudmundsson, A. (2003). Surface stresses associated with arrested dykes in rift zones. *Bulletin of Volcanology, 65,* 606-619.

[71] Gudmundsson, A. (2006). How local stresses control magma-chamber ruptures, dyke injections, and eruptions in composite volcanoes. *Earth-science reviews, 79*(1-2), 1-31.

[72] Gudmundsson, A. (2012). Magma chambers: Formation, local stresses, excess pressures, and compartments. *Journal of Volcanology and Geothermal Research, 237,* 19-41.

[73] Karaoğlu, Ö., Erkül, F., Erkül, S. T., & Lustrino, M. (2022). 3-D numerical constraints for the Triassic mafic igneous system of Antalya (SW Turkey): Magma generation associated with southern Neotethyan slow seafloor spreading. *Tectonophysics, 826,* 229236.

[74] Browning, J., Drymoni, K., & Gudmundsson, A. (2015). Forecasting magma-chamber rupture at Santorini volcano, Greece. *Scientific reports, 5*(1), 15785.

[75] Karaoğlu, Ö., Bayer, Ö., & Turgay, M. B. (2019). Magma odalarının termomekanik modellenmesi: Doğu Anadolu'dan bir örnek çalışma.

[76] Karaoğlu, Ö., Bayer, Ö., Turgay, M. B., & Browning, J. (2020). Thermomechanical interactions between crustal magma chambers in complex tectonic environments: Insights from Eastern Turkey. *Tectonophysics, 793,* 228607.

[77] Browning, J., Karaoğlu, Ö., Bayer, Ö., Turgay, M. B., & Acocella, V. (2021). Stress fields around magma chambers influenced by elastic thermo-mechanical deformation: implications for forecasting chamber failure. *Bulletin of Volcanology, 83,* 1-13.

[78] Multiphysics, COMSOL. (2021). v6.1, COMSOL AB, Stockholm. Retrieved November 10, 2024 from http://www.comsol.com

[79] Dagher, E. E., Su, G., & Nguyen, T. S. (2014). Verification of the Numerical Simulation of Permafrost Using COMSOL Multiphysics® Software. In *2014 COMSOL Conference Boston. COMSOL AB, Newton, MA, United States.*

[80] Freeman, T. T., Chalaturnyk, R. J., & Bogdanov, I. I. (2008, October). Fully coupled thermo-hydro-mechanical modeling by COMSOL Multiphysics, with applications in reservoir geomechanical characterization. In *COMSOL conf* (Vol. 2008).

[81] Glazner, A. F., Bartley, J. M., Coleman, D. S., Gray, W., & Taylor, R. Z. (2004). Are plutons assembled over millions of years by amalgamation from small magma chambers?. *GSA today*, *14*(5-Apr), 4-11.

[82] Freire-Lista, D. M., Fort, R., & Varas-Muriel, M. J. (2016). Thermal stress-induced microcracking in building granite. *Engineering geology*, *206*, 83-93.

[83] Saiang, C., & Miskovsky, K. (2011, October). Effect of heat on the mechanical properties of selected rock types–a laboratory study. In *ISRM Congress* (pp. ISRM-12CONGRESS). ISRM.

[84] Wang, F., & Konietzky, H. (2019). Thermo-mechanical properties of granite at elevated temperatures and numerical simulation of thermal cracking. *Rock Mechanics and Rock Engineering*, *52*, 3737-3755.

[85] Gualda, G. A., Ghiorso, M. S., Lemons, R. V., & Carley, T. L. (2012). Rhyolite-MELTS: a modified calibration of MELTS optimized for silica-rich, fluid-bearing magmatic systems. *Journal of Petrology*, *53*(5), 875-890.

[86] Eppelbaum, L., Kutasov, I., Pilchin, A., Eppelbaum, L., Kutasov, I., & Pilchin, A. (2014). Thermal properties of rocks and density of fluids. *Applied geothermics*, 99-149.

[87] Bell, F. G., (2013). *Engineering properties of soils and rocks.* Elsevier.

[88] Filippi, M., Slavík, M., Bruthans, J., Weiss, T., & Řihošek, J. (2021). Accelerated disintegration of in situ disconnected portions of sandstone outcrops. *Geomorphology, 391,* 107897.

[89] Gregg, P. M., De Silva, S. L., & Grosfils, E. B. (2013). Thermomechanics of shallow magma chamber pressurization: Implications for the assessment of ground deformation data at active volcanoes. *Earth and Planetary Science Letters, 384,* 100-108.

[90] Bindeman, I. N., Melnik, O. E., Guillong, M., Utkin, I. S., Wotzlaw, J. F., Schmitt, A. K., & Stern, R. A. (2023). Age of the magma chamber and its physicochemical state under Elbrus Greater Caucasus, Russia using zircon petrochronology and modeling insights. *Scientific Reports, 13*(1), 9733.

[91] Jin, Z., Cao, F., Cao, G., Zhang, C., Qiu, Z., Zhang, L., ... & Sun, J. (2023). Effect of casting temperature on the solidification process and (micro) structure of Zr-based metallic glasses. *Journal of Materials Research and Technology, 22,* 3010-3019.

[92] Tasaki, R., Noda, Y., Hashimoto, K., & Terashima, K. (2012). Sand Mold Press Casting with Metal Pressure Control System. In *Science and Technology of Casting Processes*. IntechOpen.

[93] Gerbault, M., Cappa, F., & Hassani, R. (2012). Elasto-plastic and hydromechanical models of failure around an infinitely long magma chamber. *Geochemistry, Geophysics, Geosystems, 13*(3).

[94] Le Corvec, N., Menand, T., & Lindsay, J. (2013). Interaction of ascending magma with pre-existing crustal fractures in monogenetic basaltic volcanism: An experimental approach. *Journal of Geophysical Research: Solid Earth, 118*(3), 968-984.

[95] Eldursi, K., Branquet, Y., Guillou-Frottier, L., & Marcoux, E. (2009). Numerical investigation of transient hydrothermal processes around intrusions: Heat-transfer and fluid-circulation controlled mineralization patterns. *Earth and Planetary Science Letters*, *288*(1-2), 70-83.

[96] Browning, J., & Gudmundsson, A. (2015). Caldera faults capture and deflect inclined sheets: an alternative mechanism of ring dike formation. *Bulletin of Volcanology*, *77*, 1-13.

[97] Geologic Column of the Mount Rogers Area. (n.d.). Retrieved May 19, 2024, from https://sites.radford.edu/~fldsch/RUFieldschool/fieldtrips/MountRogers/MtRogersGeolColumn/MtRogersGeolColumn.html

[98] Molina, O., Vilarrasa, V., & Zeidouni, M. (2017). Geologic carbon storage for shale gas recovery. *Energy Procedia*, *114*, 5748-5760.

[99] Brown, D. J., Holohan, E. P., & Bell, B. R. (2009). Sedimentary and volcano-tectonic processes in the British Paleocene Igneous Province: a review. *Geological Magazine*, *146*(3), 326-352.

[100] Bilgen, S., & Sarıkaya, İ. (2016). New horizon in energy: Shale gas. *Journal of natural gas Science and Engineering*, *35*, 637-645.

[101] Study of earth science, rocks and minerals. (2024). Retrieved May 24, 2024, from https://geologyscience.com/

[102] Gautam, P. K., Verma, A. K., Jha, M. K., Sharma, P., & Singh, T. N. (2018). Effect of high temperature on physical and mechanical properties of Jalore granite. *Journal of Applied Geophysics*, *159*, 460-474.

[103] Massa, M., Barani, S., & Lovati, S. (2014). Overview of topographic effects based on experimental observations: meaning, causes and possible interpretations. *Geophysical Journal International*, *197*(3), 1537-1550.

[104] Meredith, P. G., Knight, K. S., Boon, S. A., & Wood, I. G. (2001). The microscopic origin of thermal cracking in rocks: An investigation by simultaneous time-of-flight neutron diffraction and acoustic emission monitoring. *Geophysical research letters, 28*(10), 2105-2108.